This is to certify that the
thesis entitled

IN VITRO BIOMECHANICAL ANALYSIS OF SEVERAL JOINT AND FRACTURE FIXATION TECHNIQUES

presented by

Michael T. Sinnott

has been accepted towards fulfillment
of the requirements for the

M.S. degree in Mechanical Engineering

Roger C. Haut
Major Professor's Signature

Dec. 4, 2008
Date

IN VITRO BIOMECHANICAL ANALYSIS OF SEVERAL JOINT AND FRACTURE FIXATION TECHNIQUES

By

Michael T. Sinnott

A THESIS

Submitted to
Michigan State University
in partial fulfillment of the requirements
for the degree of

MASTER OF SCIENCE

Mechanical Engineering

2008

ABSTRACT

IN VITRO BIOMECHANICAL ANALYSIS OF SEVERAL JOINT AND FRACTURE FIXATION TECHNIQUES

By

Michael T. Sinnott

The goal of biological fixation is to achieve a balance between the mechanical stability of a joint or fracture repair and the biological preservation of the soft tissue surrounding the site of the repair. The following studies focused on several new techniques for the repair of joint instability as well as comminuted long bone fractures. In Chapter 1, the *in vitro* biomechanical response of pancarpal arthrodesis constructs using either a limited contact dynamic compression plate (LC-DCP), or a recently developed hybrid plate (HP) was investigated. This study demonstrated the mechanical advantages of the HPs over LC-DCPs, making them a viable alternative to LC-DCPs. In Chapter 2, a tibial gap fracture model featuring a synthetic bone substitute developed by our group was used to mechanically compare an investigational interlocking nail (ILN) system, featuring extended modified bolt-pins coupled to a type-IA external skeletal fixator (ILN-ESF), to standard bolted ILN (ILNb) constructs. Results showed that the substitution of locking bolts with extended bolts connected to an ESF significantly reduced construct compliance and overall deformation and eliminated the inherent slack of the ILNb. In Chapter 3, a novel nail (ILNn), engineered by our group, was investigated. This study demonstrated that the ILNn may represent a biomechanically more effective fixation method than standard ILNs for the treatment of comminuted diaphyseal fractures as well as a valid alternative to plate fixation. The results presented in this thesis demonstrate the mechanical and biological advantages of several new techniques for biological fixation.

ACKNOWLEDGEMENTS

I would like to thank my academic advisor, Dr. Roger C. Haut for allowing me to take part in the research at the Orthopaedic Biomechanics Laboratories (OBL) and for continuously motivating me to succeed. I would also like to thank my research advisor, Dr. Loïc M. Déjardin for his expertise, dedication, and leadership throughout my research at the College of Veterinary Medicine Orthopaedic Investigations Laboratory (COIL). Above all, I would like to thank Dr. Haut and Dr. Déjardin for providing me with the opportunity to achieve my goals and for their persistence to see each of these projects to the end. I would also like to acknowledge Dr. Gary Cloud for his excellence in teaching and for his guidance while serving on my committee. I would also like to thank Clifford Beckett of the OBL and Mike McLean of the Engineering Research Machine Shop for their knowledge, creativity, and willingness to help. Finally, I would like to acknowledge everyone who worked with me at both the OBL and COIL; including Eric Meyer, Jennifer Lansdowne, Dennis Ting, Keith Curcio, Eugene Kepich, Lynn Martin, Jerrod Braman, and Tim Baumer.

I would like to thank my better half, Nicole Tarala, for inspiring me to achieve and for patiently being at my side for every step of the way. I would like to thank my siblings, Lory, Nikki, Danny and Monique, for their unspoken lessons and unwavering support in everything I do. I would also like to thank my parents, Judith and Daniel Sinnott, for teaching me the importance of an education and for instilling in me the desire for knowledge and the courage to passionately pursue happiness. I never could have done this without you.

TABLE OF CONTENTS

LIST OF TABLES

LIST OF FIGURES

Images in this thesis are presented in color

LIST OF EQUATIONS

CHAPTER ONE

IN VITRO MECHANICAL EVALUATION OF DYNAMIC COMPRESSION PLATES FOR PANCARPAL ARTHRODESIS

ABSTRACT

Pancarpal arthrodesis is indicated for severe injuries, degenerative conditions and instability of the carpus. While various fixation methods have been described in large dogs, the most common procedure uses a dorsally applied 3.5mm AO/ASIF limited contact dynamic compression plate (LC-DCP). Due to various clinical issues associated with the use of LC-DCPs, a new 3.5/2.7mm hybrid pancarpal arthrodesis hybrid plate (HP), which tapers distally in both width and thickness, has recently been designed. The purpose of this study was to compare the biomechanical properties of pancarpal arthrodesis constructs using either an LC-DCP or an HP. The hypotheses of this study were that pancarpal arthrodesis constructs stabilized with an HP would experience less angular deformation than LC-DCP constructs under load. It was further hypothesized that HPs would experience less strain than LC-DCPs at various load levels. Seven pairs of canine forelimbs were obtained from dogs of similar body weight euthanized for reasons unrelated to this study. Seven HPs and 7 LC-DCPs were consistently bent to 20°, using a custom-designed bending press. All plates were instrumented with two strain gages placed in the area of maximum bending on the medial and lateral side. Arthrodesed constructs were embedded in epoxy molds and mounted in a servo-hydraulic testing machine using custom-designed articulated fixtures that allowed rotation in the sagittal plane. Specimens were successively loaded at 100, 200 and 300N for 10 cycles. Data, consisting of construct angular deformation and plate strain, were compared using paired

t-tests. The results of this study were that the angular deformation, and plate strain of the HP constructs was less than the LC-DCP constructs at all load levels. This study demonstrated the mechanical advantages of the HPs over LC-DCPs under physiological loading conditions. The smaller HP construct angular deformation and plate strain may reduce the risk of implant failure and post-operative morbidity. The improved mechanical properties of the HP make this implant a viable alternative to LC-DCPs.

INTRODUCTION

Arthrodesis (surgical fusion of a joint) is an orthopaedic procedure most often performed in the carpus and tarsus.[1-4] In canines, the carpus is similar to the cluster of bones in the human hand between the radius and ulna and the metacarpals. The carpal bones are not directly associated with the digits, whereas the metacarpal bones are. The joint between the radius/ulna and the carpus is called the radiocarpal joint (Figure 1-1).

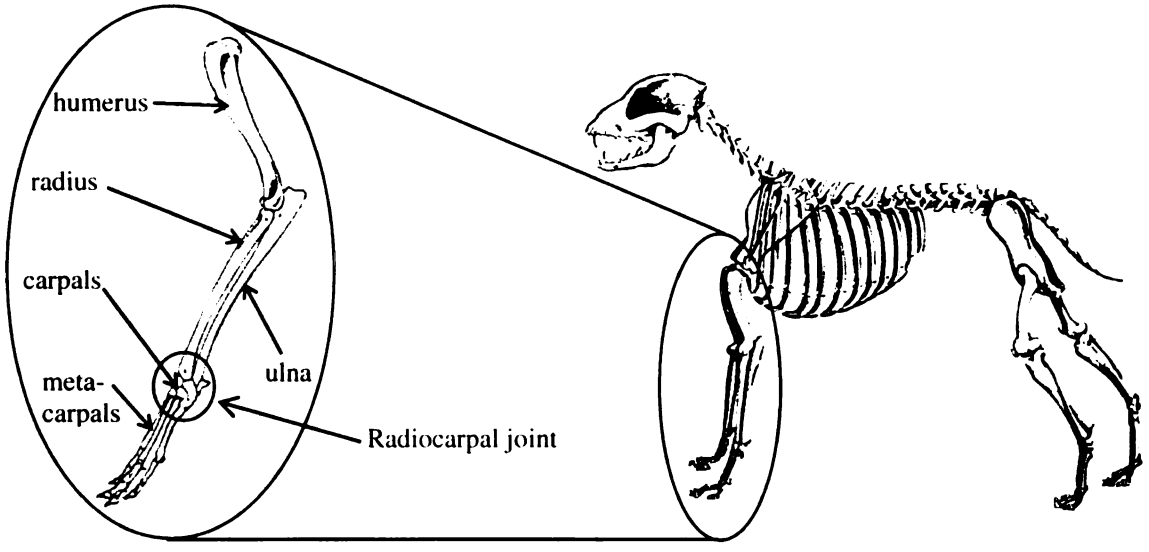

Figure 1-1. Canine skeleton, with upper extremity bones indicated.[5]

Arthrodesis of the carpus is most commonly indicated after an injury caused by hyperextension (Figure 1-2).[2]

Figure 1-2. Lateromedial radiograph of the radiocarpal joint. The figure on the left is of a normal joint; the figure on the right shows a severe hyperextension.[MSU SACS*]

Falling or other impact traumas that hyperextend the carpus can cause severe injury to the numerous palmar ligaments that support the 3 levels of the carpal joints (Figure 1-3).

* MSU SACS: *Michigan State University Small Animal Clinic Sciences.* College of Veterinary Medicine, Michigan State University. East Lansing, MI

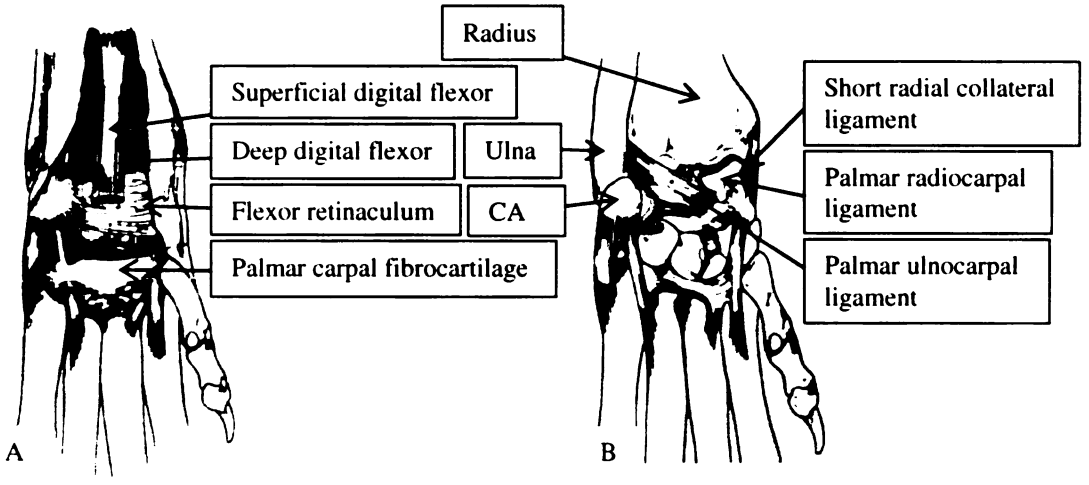

Figure 1-3. A) Superficial ligaments of the left carpus, palmar aspect. B) Deep ligaments in the left carpus, palmar aspect.[6]

These ligaments, along with the palmar fibrocartilage located on the palmar aspect of the carpometacarpal joint space, are the major supports that permit ~15° of extension at the antebrachiocarpal joint in the average standing animal.[7] Although immune-mediated arthritis can cause some of these hyperextensions,[2,7] one of the more common causes is a degenerative condition of the palmar carpal ligaments seen in older, large-breed dogs.[8,9] Other indications for carpal arthrodesis include intractable distal radial and carpal fractures or dislocations (Figure 1-4), where adequate joint stability cannot be achieved and severe luxation/subluxation is present. Cases of severe carpal arthritis and selected neurological defects, where medical therapy does not provide adequate pain relief and limb function, have also been shown.[2,10]

Figure 1-4. Dorsopalmar radiograph of the radiocarpal joint. The figure on the left is of a normal joint; the figure on the right shows a distal radial fracture. MSU SACS

Evaluation of patients with hyperextension, fractures, or dislocations of the carpus involves physical examination to determine the degree of joint instability, as well as taking dorsopalmar and lateromedial radiographs (Figure 1-5).

Figure 1-5. Dorsopalmar (left) and lateromedial (right) radiographs of a normal canine radiocarpal joint. MSU SACS

The carpometacarpal joint is most commonly involved due to the support provided by the palmar carpal fibrocartilage found at this level (Figure 1-3). Instability of the radiocarpal joint is present in only 10% of cases with hyperextension.[2,7] The main structure that provides significant radiocarpal support during weight bearing is the flexor carpi ulnaris muscle, which inserts on the accessory carpal bone (Figure 1-6).

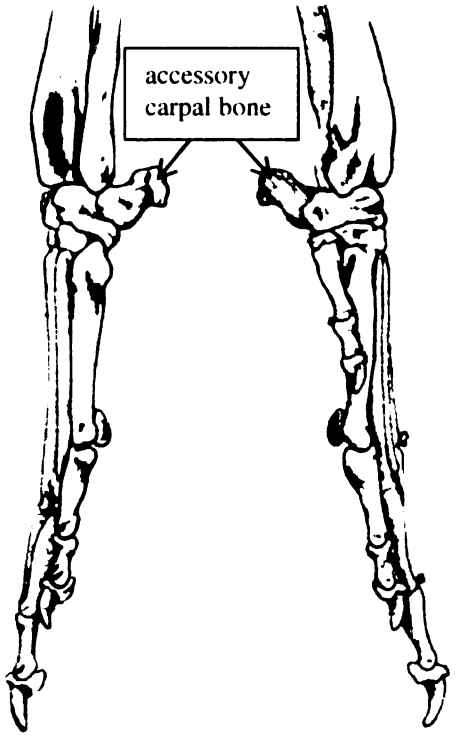

Figure 1-6. Lateral (left) and medial (right) view of the carpus and metacarpal bones, indicating location of the accessory carpal bone.[6]

Disruption of the ligaments attaching the accessory carpal bone to the carpal and or metacarpal bones will result in proximal displacement of the accessory carpal bone.[2,7] Identification of the joint levels involved in the injury leads to the next question: partial carpal arthrodesis or pancarpal arthrodesis. Since carpal hyperextension injuries do not necessarily involve the radiocarpal joint, some argue that if the radiocarpal joint is preserved only partial arthrodesis should be performed. Partial arthrodesis involves only the intercarpal and carpometacarpal joints thus resulting in little change in gait. Furthermore, the procedure involves limited surgical equipment and implants such as cross-pin stabilization and cancellous bone grafting have been described.[7] Pancarpal arthrodesis, in contrast, produces a change in gait, where animals must learn to circumduct the limb during the forward swing phase of the gait since the carpus can no

longer be flexed. Partial arthrodesis in the presence of subtle or mild radiocarpal ligament pathology could lead to a subsequent breakdown and reoccurrence of hyperextension. Regardless of partial or pancarpal arthrodesis, the procedure may increase stresses on adjacent joints, potentially resulting in degenerative joint disease. With partial carpal arthrodesis, there is a high risk of radiocarpal degenerative joint disease (DJD) due to impingement between the implant and the distal aspect of the radius.[2,11] For these reasons, pancarpal arthrodesis is most often preferred, regardless of the level of carpal joint injury.[2]

While various internal and external stabilization procedures have been described, [2,4,12] a dorsally applied limited contact dynamic compression plate (LC-DCP) is the standard technique currently recommended for pancarpal arthrodesis.[1] Application of a plate to the carpus for pancarpal arthrodesis presents several technical challenges. First, basic fracture repair biomechanics dictate that in order to provide adequate support, the bone plate should be placed on the tension side of the bone (i.e. the palmar aspect of the carpus). This is due to the fact that upon physiological loading of the bone, compressive forces will reduce the fracture gap. Muller et al. found that excessive fracture gap, with no inherent fracture stability, may lead to a hypertrophic nonunion. However, the approach to the palmar aspect of the canine carpus is difficult due to the important tendinous and vascular structures located in this area (Figure 1-3). Consequently the compression surface (dorsal aspect) of the carpus is the preferred location.[12] Second, plates that are sized appropriately for a dog's radius accept screws that are often too large for the carpal and metacarpal bones. Until recently, the choice of bone plates has been limited to the LC-DCP included in the AO/ASIF (Arbeitsgemeinschaft fur

Osteosynthesefragen / Association for the Study of Internal Fixation) system.[9] While these plates are suitable for the radius, they become too wide and thick for the metacarpal region of most dogs, leading to complications. Mainly, the screw diameter used in a LC-DCP that is appropriately sized for the radius typically encompasses more than 50% of the diameter of the metacarpal bone. This results in an increased risk of metacarpal fracture and subsequent implant failure because the large screw diameter, relative to the diameter of the bone, acts as a stress riser (Figure 1-7).[13]

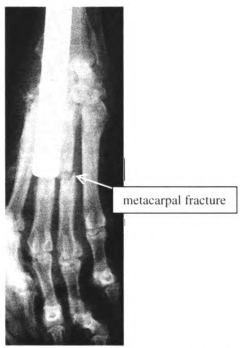

Figure 1-7. Dorsopalmar radiograph showing metacarpal fractures induced by large metacarpal screw diameter in relation to bone size. MSU SACS

Conversely, the use of a smaller plate with screws that are appropriate for the metacarpal bones sacrifices plate strength and rigidity. Third, there is limited soft tissue coverage over the metacarpal region, thus closure over the relatively thick LC-DCP is usually done under excessive tension, leading to incisional dehiscence and secondary wound complications. Considering these complications, a hybrid pancarpal arthrodesis

plate (HP) was developed by Veterinary Instrumentation in Sheffield, U.K. (Figure 1-8). Some images in this thesis are presented in colour.

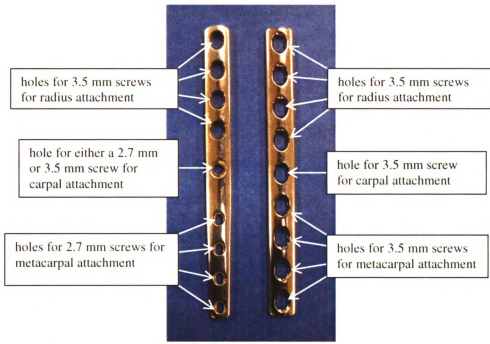

Figure 1-8. Comparison of the HP and LC-DCP, the HP is shown on the left and the LC-DCP is on the right.

The HP features nine screw holes spanning its entire length. Hybrid plates that would be used in a mid-sized dog (~30 kg) includes four 3.5 mm oval dynamic compression (DC) screw holes in the proximal aspect of the plate, four 2.7 mm DC screw holes in the distal aspect of the plate, and one central round screw hole, which can accommodate either a 3.5 mm or 2.7 mm screw. The smaller screws in the distal aspect may reduce the risk of metacarpal fracture. In addition, the HP is manufactured at a standard length or with an extended length of 17 mm. A recent study demonstrated that the risk of a bone fracture at the distal screw hole was reduced if at least 50% of the length of the metacarpal bone was covered by the bone plate.[13] The added length of the extended HP could thus further prevent metacarpal fracture. The HP also narrows at the

distal end in both width and thickness. This feature allows for easier closure and less incisional tension.

Although the introduction of the HP has improved clinical application of the plate during surgery, controversy remains regarding the angle at which the plate should be placed in order to provide the strongest construct while preserving a functionally appropriate carpal angle. Traditionally, canine carpal joints have been fused at a straight (0°) angle. Although some veterinarians continue to use this technique because a straight plate usually provides a stiffer construct, MSU SACS experience suggests that forcing the carpus into a straight position not only results in poor contact of the digital and metacarpal pads with the ground and subsequent gait abnormalities, it can also cause tendonitis and bursitis and thus is not an optimal fixation. In order to circumvent this limitation the HP has been designed with a distal taper in thickness that places the carpus in approximately 4° to 5° of hyperextension without having to bend the plate. However, the normal standing angle of the canine carpus is approximately 15° hyperextension.[20] While the HP could be advantageous over a standard LC-DCP due to an extended fatigue life of the plate given that it allows for some angling without having to actually bend the plate,[15] it still fails to place the carpal joint at the desired angle of hyperextension.

Current veterinary surgical textbooks recommend the fusion of the carpal joint at 10° to 15° of hyperextension.[1,14] Anecdotally it has been the experience of MSU SACS that further angulation of the plate up to 20°, allows for better contact between the ground and the paw at paw strike. This appears to be particularly important at faster gaits such as the trot.[14] The surgeon's choice to bend the plates introduces multiple complications to the integrity of the plate. As mentioned before, bending the plate immediately reduces the

strength of the plate for static reasons. More specifically, the introduction of a bend in the plate creates a larger moment arm than if the plate were left straight, increasing the stresses experienced by the plate at the location of the bend. Another problem of clinical relevance is the actual bending of the plate, and the type of resultant bend. Because the plate has varying cross sectional areas throughout its length, due to the presence of screw holes, the ability of the plate to resist deformation is dramatically reduced in some areas of the plate. It has been the experience of MSU SACS that bending the currently available LC-DCP consistently produces a bend at the level of a screw hole (Figure 1-9). Basic strength of materials theory states that a region of reduced cross sectional area (screw hole level) will experience greater stress under a given load and subsequently will deform prior to a region which has a greater cross sectional area (non screw hole level).[17] In theory, LC-DCPs have equal cross sectional areas (CSA) throughout the length of the plate due to their undersurface design which features cutouts between screw holes so that the CSA of the plate at screw hole levels is equal to the CSA of the plate between screw holes. Although this weak spot should theoretically not exist in LC-DCPs, it has been the experience of MSU SACS that the bend still tended to occur near a screw hole. The undersurface design of the HP does not feature any cutouts and therefore should theoretically be much weaker at the screw hole level and subsequently consistently bend at that location. The largest problem with the bend of the plate occurring at the cross section with a hole once again is related to the bending stress in a member, which is inversely proportional to the area moment of inertia (AMI) of the member. Current bending presses also allow the bend to span a larger length of the plate, due to inherent design flaws, specifically the fact that there is no way of locking the plate to the bending

press while bending. This makes bone-plate contact difficult in the area of the joint, due to the bend being in the shape of an arc (Figure 1-9).

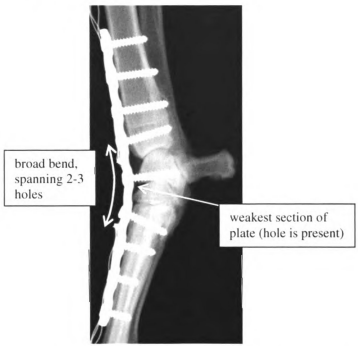

Figure 1-9. Lateromedial radiograph of an implanted LC-DCP bent with a standard bending press. The standard press allows the bend to span over an extended length. Reduction of bone-plate contact area due to the shape of the standard bend was also visible. MSU SMAC

So ideally, if a bend is to occur, extreme care must be taken to ensure that the bend is concentrated in an area of the plate where no hole is present (solid section). Due to the increased force and precision necessary for this to occur, a bending press was specifically designed (MSU BP), for the purpose of this study. This press, if used in the operating room, could also enable a surgeon to produce a concentrated bend at a determined location on the plate, regardless of the cross section of that location.

With the occurrence of a bend in the plate as large as 20°, the effect of the bend on the integrity of the plate should be considered. Since a known amount of deformation is to be given to the plate (20° curvature), the cross section of the plate where the bend is

to occur must be evaluated. The HP and LC-DCP have different cross sections, therefore they must be considered differently. Under a given curvature, the distance from the neutral axis to the surface of an implant governs the strain experienced in a given cross section.[17] The thickness of the cross sections of the two plates (1 mm difference) do not affect the strain experienced by the plates as much as their geometries do. The cross section of the LC-DCP is crown shaped in the solid section of the plate, whereas the HP has a cross section similar to a thin rectangle in the solid section of the plate. To investigate the significance of their respective cross sections, a finite element analysis was done on each plate. In this analysis, the cross sectional areas of the plates, where the bend occurs, were subjected to a point load normal to their dorsal surface. Based on the results of this theoretical analysis (Appendix 4), it was determined that the HP would deform less and be subjected to less stress than the LC-DCP under a given load. Li. et al. showed good clinical outcomes with radiocarpal extension from 5-10°, reporting that arthrodesis occurred in all thirteen cases. Although a 20° bend may have the potential to weaken the bone plate and decrease its fatigue life, to date no studies comparing the biomechanical properties of a LC-DCP to a HP placed at a functionally appropriate 20° angle have been reported. Therefore, the main purpose of this study was to compare the biomechanical properties of a nine-hole LC-DCP and an extended length 3.5/2.7 mm HP placed at a 20° bend for canine pancarpal arthrodesis. It was also desired to develop a clinically usable bending press, which could produce a bend in plates that was both consistent and functional. The hypotheses were that the HP constructs would undergo less radiocarpal joint angular deformation and that the HP would experience less plate strain compared to the LC-DCP, due to differences in the cross sections of the plates.

MATERIALS AND METHODS

Implant Preparation

Plate Bending – Prior to specimen collection, seven LC-DCPs and HPs were accurately bent to 20°. Due to the difficulty and inconsistency of using current plate bending tools and techniques, a specially designed bending press was developed (MSU BP [Figure 1-10]).

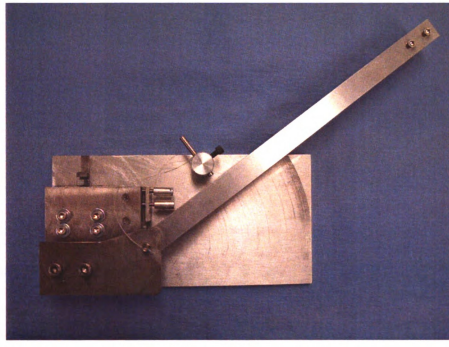

Figure 1-10. Top view of the MSU BP

The bending press uses a design commonly seen in pipe bending, where a lever arm is rotated about a fulcrum and movement of the lever arm results in the bending of the pipe. The pipe is essentially being forced into the shape of the fulcrum by the distribution of force by a contact point. This concept was translated into a design, which would enable a similar deformation or bending of a veterinary plate. In our bending press, the plate was placed between two pins, one pin acted as a fulcrum and the other pin acted

as the contact point. Both pins were fixed on a lever arm, which enabled the generation of large enough forces to bend the steel plates. Without adequate length of the lever arm, the design of the bending press would be impractical due to the difficulty of generating enough force to cause the resultant bend. The lever arm and both pins were then fixed to a location on the base of the bending press. Both plates are convex dorsally and concave palmarly (Figure 1-11).

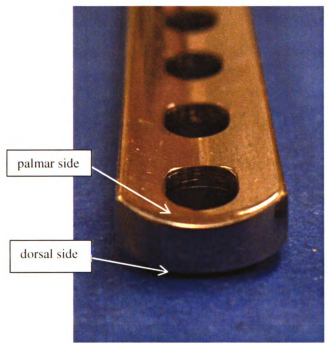

Figure 1-11. Dorsal and palmar aspects of both plates have convex and concave surfaces, respectively. A HP is shown.

When placed into the bending press, the dorsal and palmar aspects of the plate, or convex and concave respectively, were in contact with both the fulcrum and contact pins, respectively. To enhance the quality of the bend, the fulcrum and contact points were fashioned into a concave and convex radius, respectively, which matched the concave and convex aspects of the plate (Figure 1-12).

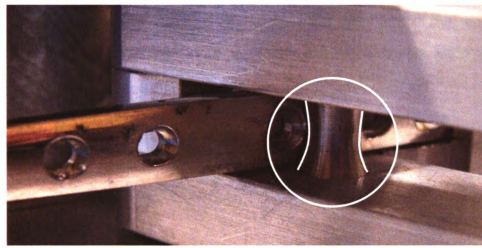

Figure 1-12. View of the concave fulcrum (shown in white) with a curvature matching the dorsal aspect of the plate.

The importance of the distribution of forces over the entire width of the plate will be further explained in the strain gage application section. The plate was fixed to prevent displacement horizontally by a pin located proximally to the bend of the plate (Figure 1-13).

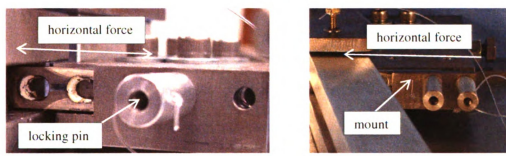

Figure 1-13. Mount and pin, which locked the plate in position, resisting force from the fulcrum and contact point, which would result in horizontal displacement.

The mount that the pin attached the plate to was adjustable in the same horizontal plane on the base of the bending press, this allowed for changes in the location of the bend if desired. When the mount and pin were in place and secured, the bending press was ready for use. By trial and error, the amount of lever arm rotation needed to achieve

the desired bend of 20° was located. The bending press also included a locator, which would enable a consistent amount of lever arm rotation; this was utilized once a satisfactory bend was achieved (Figure 1-14).

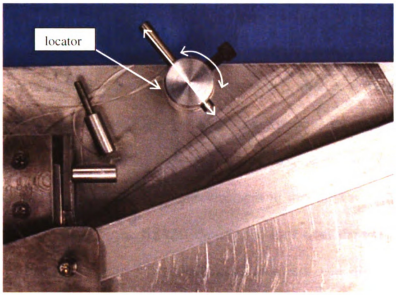

Figure 1-14. View of the locator, which stopped the lever arm when a specific degree of rotation was completed. The resultant bend in the plates could be modified by adjusting the position of the locator.

There were differences in the positioning of the mount and locator between the HP and LC-DCP constructs in order to achieve the desired bend angle of 20° Trial and error provided to be the most accurate means of finding these points. The location dissimilarities were due to geometrical differences of the thickness and width between the HP and LC-DCP, resulting in different amounts of force required to achieve the desired bend. The plate holes were numbered 1 through 9 from proximal to distal, all plates were bent between the 4^{th} and 5^{th} screw hole. See Appendix 1 for MSU BP instructions.

Strain Gage Application – The importance of the distribution of force over the entire width of the plate, instead of a point load, was to preserve the integrity of the surface of

the plate. Strain gage application requires very specific surface conditions for proper adhesion and accurate measurements. The presence of a point load (if standard bending irons are used rather than the MSU BP) would result in large enough compressive forces to cause plastic deformation of the plate in the form of a dent on the dorsal surface of the plate, where the gage was applied. This dent or divot would cause a stress concentration in addition to the already present location of high stress, relative to other areas of the plate, which we were intending to measure. The already present stress risers were: a hole located adjacent to the gage, and the gage was placed directly on top of the bend in the plate. Due to the size of the dent, strain measurement in that area would not have been quantifiable with our strain gages. By distributing the load over the entire width of the plate, the MSU BP, prevented this from occurring to an extent, and allowed for an evenly distributed bend matching the radius of the fulcrum

Strain gages were applied to medial and lateral sides of each plate between the fourth and fifth screw hole, adjacent to the bend (Figure 1-15). Strain gage selection was based on the required size of the gage and the estimated levels of strain, which would be incurred during testing. Strain values were not expected to exceed 4000 με. The selected strain gage (EA-06-031DE-350 Vishay Micro-Measurements) was rated for 3% strain, and had a gage length of 0.79 mm and a grid width of 0.81 mm. Gages were applied by the same person (Keith Curcio, DVM, MSU SACS); see Appendix 1 for full strain gage application instructions.

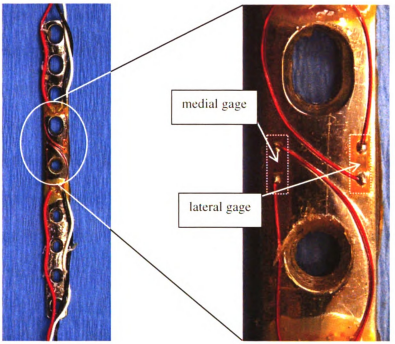

Figure 1-15. Location of strain gages (outlined in white) on plates, HP is shown.

Specimen Preparation

Seven pairs of anatomically normal canine thoracic limbs were harvested from dogs, which weighed between 30 – 32 kg and had been euthanized for reasons unrelated to this study. Additionally, dogs were chosen based on the length (80 ± 0.15 mm) and diameter (8 ± 0.15 mm) of the third metacarpal bone, which was determined radiographically. The limbs were disarticulated at the elbow and metacarpal/phalangeal joints. All soft tissue structures were then removed from the limb with the exception of the supporting structures around the carpal joint. The articular surfaces were left intact in order to maintain consistency. The limbs were then stored in a – 20° C freezer until the time for plate application and biomechanical testing. All specimen preparation was carried out by the same person (Keith Curcio, DVM, MSU SACS).

Within one pair of limbs, a HP bent to 20° was applied to the dorsal side of the limb. A 3.5 mm screw was first placed into screw hole number 5 to assure accurate placement into the radiocarpal bone. Next a 2.7 mm screw was placed in screw hole number 8 into the third metacarpal bone to make sure the plate lined up on the midline of the bone. Then a 3.5 mm screw was placed in screw hole number 2 into the radius. The remaining screws were then filled starting proximally with screw hole number 1 down distally to screw number 9. The end result was four 3.5 mm screws in the radius, four 2.7 mm screws in the third metacarpal bone, and one 3.5 mm screw in the radiocarpal bone Figure 1-16). The LC-DCPs bent to 20° were placed on the opposite limb in a similar fashion. However, in the LC-DCP group all nine screws were 3.5 mm (Figure 1-17).

Figure 1-16. Dorsopalmar (left) and mediolateral (right) radiographs of specimen implanted with fully instrumented HP. MSU SACS

Figure 1-17. Dorsopalmar (left) and mediolateral (right) radiographs of specimen implanted with fully instrumented LC-DCP. [MSU SACS]

The proximal portion of the radius and ulna were then transected 4.5 cm above the proximal aspect of the bone plate to standardize the length of the specimen. The interosseous ligament remained intact at this level.

Specimen Potting

The extremities of all of the specimens were embedded in an epoxy mold (Fibre Strand, Martin Senour Corp., Cleveland OH.) conforming to a custom designed articulated loading cup. Potting consistency and accuracy were enabled with a specially designed potting jig (Figure 1-18).

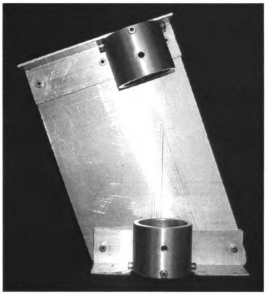

Figure 1-18. Specially design potting jig to fix the constructs at 20° of hyperextension.

Caution was taken in positioning the specimens during potting to ensure that the compressive loading of the specimens during testing caused pure bending. The presence of any off axis loading of the plates, if the plate itself was not oriented perfectly vertical, would apply a twisting moment on the plate. The presence of any type of twisting or torsional force would drastically effect both angular deformation and strain gage data. The epoxy mold extended just below the distal aspect of the plate without contacting it, and was perpendicular to the metacarpal bones. This was also achieved by a specially designed piece of the potting jig, which encompassed the metacarpals and protected the plate from any contact with the epoxy material (Figure 1-19).

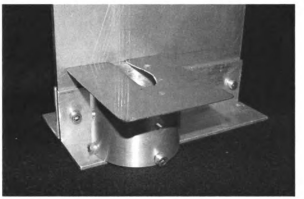

Figure 1-19. Insert at base of potting jig to prevent contact between the epoxy and the plate near the metacarpals.

Mechanical Testing and Data Acquisition

Specimens were mounted on a servo-hydraulic testing machine fitted with a 500 lb (2,225 N) load cell (Figure 1-20) (Interface, Scottsdale, AZ).

Figure 1-20. 500 lb load cell, mounted on the base of the Instron table.

Specimens were secured to the testing machine via articulated custom designed cups, which allowed free rotation of the specimen in the sagittal plane (Figure 1-21). This allowed physiologic flexion of the specimen during loading, and minimized non-physiologic stress concentrations at either bone-epoxy interface. The rotation axis of each mount was instrumented with rotary encoders (Renco Encoders Inc., Goleta, CA) to enable measurement of the specimen angular deformation during testing (Figure 1-21).

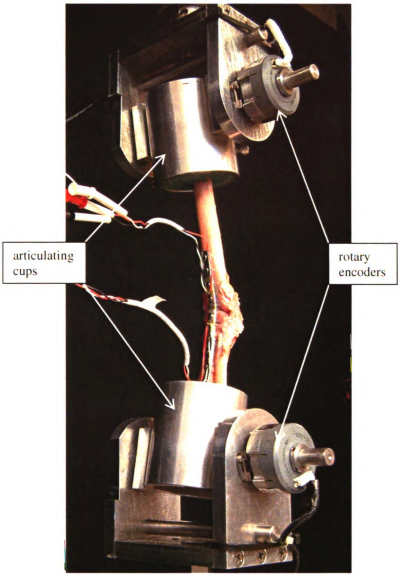

Figure 1-21. Specimen mounted in servo-hydraulic testing machine.

Biomechanical testing was conducted sequentially in each pair. Prior to testing, the load cell was zeroed and a 5N preload was applied to each construct. Specimens were then successively loaded at 100 N, 200 N, and 300 N or 40%, 80%, and 120%, respectively, of body weight (BW) at a rate of 1 Hz for 10 cycles. These load levels were chosen to simulate post-operative loading conditions at rest, walk and trot respectively.[14]

Since all experiments were conducted under load-control, construct compliance (rather than stiffness) was determined. Construct compliance is the inverse of stiffness and is defined as the slope of the deformation versus load curve. Construct compliance was determined at the 10^{th} cycle. However, it was determined post-hoc that compliance was the most definitive measure of construct performance. Construct compliance is a measure of the ability of the plate alone to resist deformation whereas angular deformation is a measure of the ability of an entire construct (including bone deformation) to resist deformation. As shown in Figure 1-22, nonlinearities in the compliance curves increased with load. For this reason, angular deformation was evaluated instead of construct compliance (compliance data included in Appendix 4).

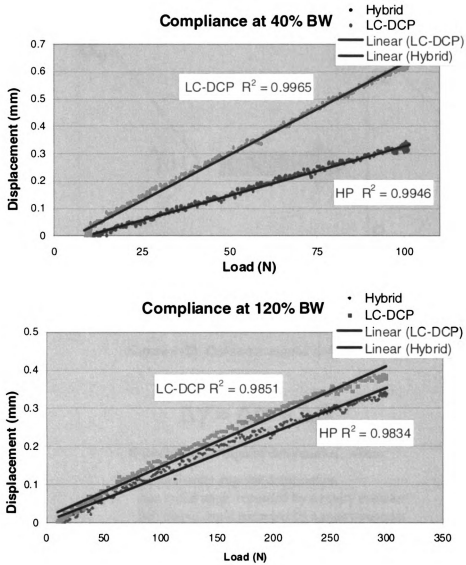

Figure 1-22. Construct compliance increased in nonlinearity as load increased. Shown are 40% (top) and 120% BW (bottom) compliance curves, corresponding to 100 N and 300 N, respectively. Notice the reduction in R^2 value from 40% to 120% BW.

As specimens were loaded, the radial and carpal angles (α and β, respectively) with respect to the vertical were recorded via the rotary encoders affixed to each articulated mount. Angular deformation ($\Delta\gamma$) was computed with Equation 1 (Figure 1-23).

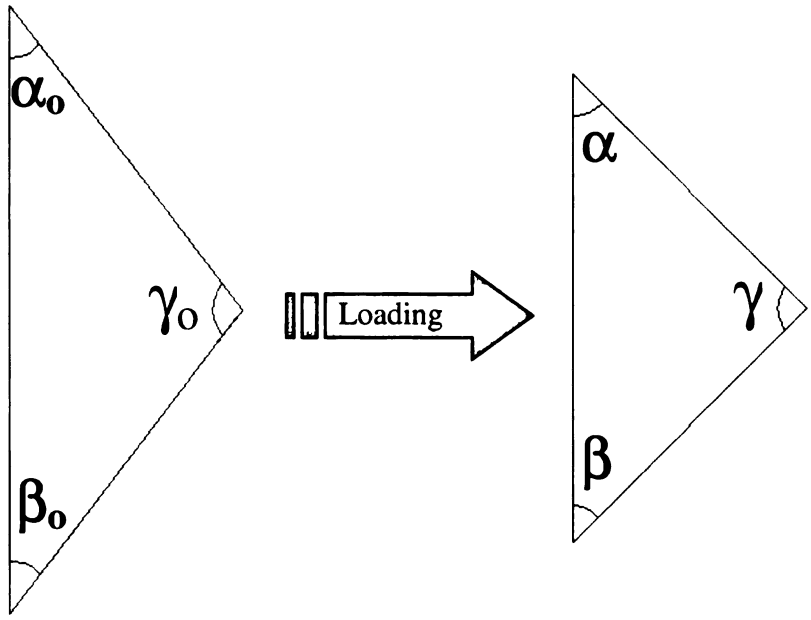

Figure 1-23. Construct angular deformation.

$$\Delta\gamma = \Delta\alpha + \Delta\beta \qquad [1\text{-}1]$$

Equation 1-1. Angular deformation, where:

$\Delta\gamma$: construct angular deformation
$\Delta\alpha$: radial angle recorded by a rotary encoder
$\Delta\beta$: carpal angle recorded by a rotary encoder

Strain gage outputs (V) were converted to microstrain ($\mu\varepsilon$) via the electrical bridge circuit of a calibrated strain gage indicator (Figure 1-24).

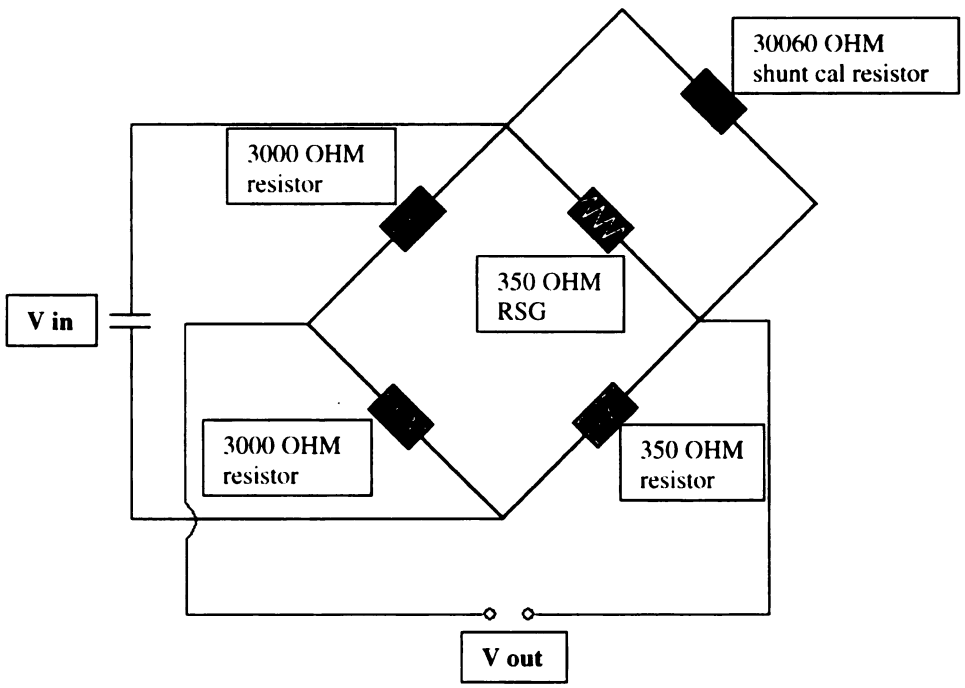

Figure 1-24. Diagram of single arm (1/4 bridge) Wheatstone bridge circuit.

Circuit calibration was used to calibrate the system; this was done by attaching a shunt calibration resistor (green in Figure 1-24) in parallel with the strain gage (red in Figure 1-24). The purpose of the shunt cal. resistor was to simulate an electrical resistance on the circuit, so the voltage readout can be adjusted to give accurate readings in relation to strain. The following equation is used to determine the strain reading when the shunt cal. resistor was activated.

$$\varepsilon_S = (R_g) / [F_g*(R_g + R_s)] \qquad [1\text{-}2]$$

Equation 1-2. Shunt calibration strain readout, where:

ε_S: strain readout with shunt cal.

R_g: strain gage resistance (350 Ohms)

F_g: gage factor (2.12 ± 1.0%)

R_S shunt cal. resistance (30060 Ohms)

Individual strains (medial and lateral, see Figure 1-15) were recorded on separate channels. Plate strain between medial and lateral gages was not significant; the two-gage setup was primarily to ensure a reading if one of the gages were to fail or not trigger properly.

Data Analysis

Construct angular deformation was recorded via the rotary encoders, linear displacement of the actuator was recorded via the Instron LVDT, and load was measured using the 500 lb load cell. Statistical analysis was performed by use a 2-factor repeated measures ANOVA (Sigma Stat). The two factors for all data analysis were the type of arthrodesis (LC-DCP or HP) and load level (100 N, 200 N, or 300 N). All pairwise comparisons were calculated with Student-Newman-Keuls post-hoc tests where significance was set at $p<0.05$.

RESULTS

Bending Press Performance

As indicated in the materials and methods section, movement of the lever arm, which was restricted by the locator, enforced deformation of the plate. Adjustment of the locator point between the two groups was necessary to acquire a 20° bend in the plates. The locator point dissimilarities between the HP and LC-DCP were due to geometrical differences of the thickness and width between the HP and LC-DCP, resulting in different amounts of force required to achieve the desired plastic deformation. The plate holes were numbered 1 through 9 from proximal to distal, all plates were bent between the 4^{th} and 5^{th} screw hole (Figure 1-25). Once the locator points were established for both plates, a consistent bend was easily and efficiently achieved (Figure 1-26). The efficiency of the bending process was due to the absence of multiple bending reiterations on each plate to achieve similar bends between plates within each group.

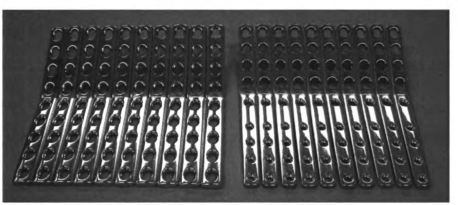

Figure 1-25. Dorsal view of plates, showing consistent location of bend for the LC-DCP group (left) and HP group (right).

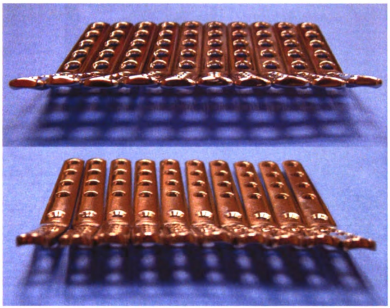

Figure 1-26. View of plates, showing consistent degree of bend for the LC-DCP group (top) and HP group (bottom).

As important as achieving a consistent location and degree of bend, was to achieve a consistent type of bend. More specifically, the goal was to produce a concentrated bend, which occurred in a solid section of a plate, without spanning over a length, which included sections where holes were present. This was consistently a problem with standard bending techniques, due to their inability to restrict movement of the plate while bending occurred. This problem was considered in the design of the new MSU BP, and the efficacy of this design in providing a concentrated, functionally located bend is shown in Figure 1-27.

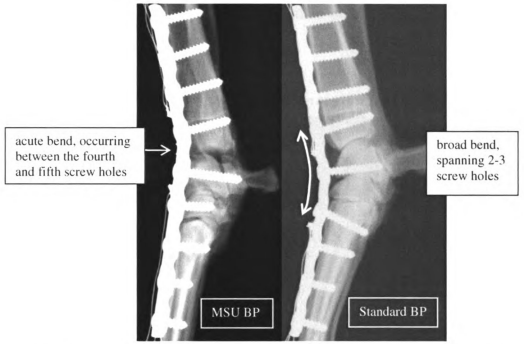

Figure 1-27. Lateromedial radiograph of an implanted LC-DCP bent with MSU BP (left) and a standard bending press (right). Notice the concentrated bend with the MSU BP occurring between the fourth and fifth screw hole, while standard bending presses allow the bend to span over a longer length. Reduction of bone-plate contact area due to the shape of the standard bend is also visible. MSU SACS

Angular Deformation During Compressive Joint Loading

Although maximum angular deformation of the HP constructs was consistently less than that of the LC-DCP constructs at all loads, these differences were only significant at 80% and 120% BW corresponding to 200 N and 300 N, respectively (Figure 1-28, Table 1-1). However, the differences between the groups were similar at all load levels, the HP consistently deformed 18-20% less than the LC-DCP. Additionally, both of the constructs angular deformation increased with increasing load levels within their respective groups. From 40% to 80% BW (100 N and 200 N), the HP exhibited a 268% increase in deformation, similarly, the LC-DCP showed a 267% increase. Results were comparable in the 80% to 120% load level increase (200 N and 300 N), where increases of 188% and 182% were found for the HP and LC-DCP

constructs, respectively. The increases shown within groups were significantly different between all load levels for both groups ($p<0.05$).

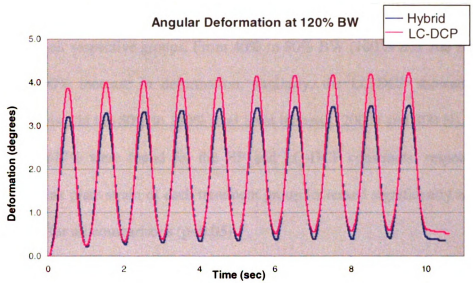

Figure 1-28. Representative angular deformation curves of HP and LC-DCP constructs at 120% BW (300 N).

Maximum Angular Deformation (°)			
	40% BW	**80% BW #**	**120% BW #**
HP	0.73 ± 0.47 †	1.96 ± 1.33 †	3.68 ± 2.48 †
LC-DCP	0.94 ± 0.66 *	2.51 ± 1.64 *	4.56 ± 2.82 *

Table 1-1. Maximum angular deformation data (mean ± SD) (where 40%, 80% and 120% BW correspond to 100 N, 200 N and 300 N respectively) indicating significant differences ($p < 0.05$, see Appendix 4 for exact values):

\# between HP and LC-DCP constructs
† between load levels for HP constructs
* between load levels for LC-DCP constructs

Plate Strain

All plate strain data was taken as the average of the two gages on each plate, since significance was not seen between the medial and lateral strain readings. Similar to angular deformation, plate strain in the HP constructs was consistently less than that of the LC-DCP constructs. The HP experienced approximately 35% less plate strain than the

LC-DCP at all load level, this difference, however, was only significant at 80% and 120% BW, or 200 N and 300 N, respectively (Figure 1-29, Table 1-2). Similar to construct angular deformation, plate strain also increased equally with increasing load levels within their respective groups. From 40% to 80% BW (100 N and 200 N), the HP exhibited a 240% increase in deformation, similarly, the LC-DCP showed a 239% increase. Likewise, in the 80% to 120% load level increase (200 N and 300 N), increases of 170% and 177% were found for the HP and LC-DCP constructs, respectively. In addition, the peak plate strain of each treatment group increased significantly as the load level increased for all comparisons ($p<0.05$).

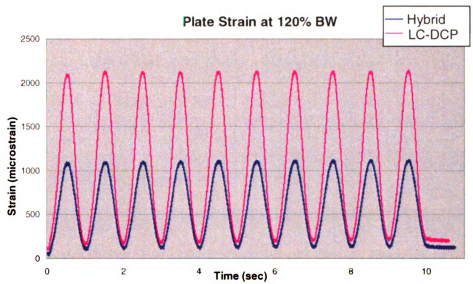

Figure 1-29. Representative plate strain curves of HP and LC-DCP constructs at 120% BW (300 N). Shown is the average of the medial and lateral strain readings for each plate.

Plate Strain (με)			
	40% BW	**80% BW** [#]	**120% BW** [#]
HP	269 ± 100 [†]	646 ± 259 [†]	1098 ± 438 [†]
LC-DCP	410 ± 203 *	980 ± 478 *	1735 ± 808 *

Table 1-2. 10th cycle plate strain data (mean ± SD)(where 40%, 80% and 120% BW correspond to 100 N, 200 N and 300 N respectively) indicating significant differences ($p<0.05$, see Appendix 4 for exact p-values):

[#] between HP and LC-DCP constructs

* between load levels for LC-DCP constructs

[†] between load levels for HP constructs

DISCUSSION

The hypotheses of the current study were that the HP constructs would undergo less radiocarpal joint angular deformation than the LC-DCP, and also that the HP would experience less plate strain compared to the LC-DCP. The results of this study supported both of the hypotheses. Firstly, the HP bent to 20°° exhibited significantly less angular deformation than the LC-DCP, at 80% BW (1.9 ± 1.3° versus 2.5 ± 1.6°, for the HP and LC-DCP respectively, at 200 N) and at 120% BW (3.7 ± 2.5° versus 4.6 ± 2.8°, for the HP and LC-DCP, respectively, at 300 N). Secondly, that the HP would experience more plate strain than the LC-DCP. This occurred at all load levels, but their differences were significant only at the 80% BW (646 ± 259 με versus 980 ± 478 με, for the HP and LC-DCP, respectively, at 200 N) and at 120% BW (1098 ± 438 με versus 1735 ± 808 με, for the HP and LC-DCP, respectively, at 300 N). The design of the cross sectional area of HP was the major reason there was an improvement in the biomechanical variables documented in this study in comparison to the LC-DCP.

Based on recent *in vitro* studies, the decrease in construct angular deformation observed in the specimens implanted with a HP has several potential advantages. It decreases the risk of catastrophic plate failure by increasing the ability of the plate to sustain higher loads. Similarly, the magnitude of stress from each bending cycle during daily activity is also decreased, which in turn, may translate into an increase in plate fatigue life.[18] This becomes important because in an angulated construct, there is an increase of cyclic loading at the point of maximum bending. With repetitive loading, construct angulation may promote fatigue failure of the plate. Although the immediate effect of the decreased HP construct deformation appears minor, on the basis of results

from previous studies on tarsal arthrodesis constructs,[15] it can be speculated that the reduced deformation seen in the HP may have a substantial effect over the life of the implant. Hulse et al. demonstrated on 316L cold-worked stainless steel that a reduction in strain by two-fold could effectively extend the fatigue life of an implant by ten-fold. Regardless of how many cycles of loading and unloading were experienced, the stress levels of the HP and LC-DCP in this study were found to be far below the stress levels associated with the fatigue failure seen in the Hulse study.[19] However, in larger breed dogs, where plates would experience increased levels of stress, the effect of the increased stress on the fatigue life of the implant requires further consideration.

Several factors, primarily related to implant design, degree of construct angulation, and load magnitudes placed on the implant may predispose pancarpal arthrodesis constructs to failure. The latter two factors can be altered little, with the last being largely beyond the direct control of the surgeon. However, addressing the surgical challenge by improving the biomechanics of the implant construct has the potential to minimize complications and maximize success. The implant design of the HP was the major reason there is an improvement in the biomechanical variables documented in this study in comparison to the LC-DCP. Despite a 20° bend of the plates, the HP was still shown to be biomechanically superior. The hypotheses were governed by results of a finite element analysis (FEA) that was conducted on the solid cross sections of the plates. Results of the FEA were in good agreement with results calculated using equations given for deformations in members under pure bending (See FEA data and further discussion in Appendix 4). Specifically, an equation for strain related to radius of curvature, which

states that longitudinal normal strain varies linearly with the distance from the neutral axis (see Equation B in Appendix 3).

We chose to conduct testing under load control since it better reflected the biomechanical stresses to which the constructs are subjected during physiological activities. The results of the current study indicated that in both constructs, angular deformation consistently increased with load, with significance seen in the LC-DCP construct at each load level increase. This finding likely resulted from the fact that as the plate angular deformation increased, the moment arm was increased. The moment arm was represented by the distance between the bend in the plate and the point of load application. In this study, the HP experienced less angular deformation at all loads tested, with significance seen at 80% BW (200 N) and 120% BW (300 N), simulating walk and trot, respectively. The absence of a significant difference in the 40% BW (100 N) was most likely attributable to large deviations seen at those load levels due to the reduced load bearing needs of the plate. Though the LC-DCP showed greater angular deformation at all load levels, the deviation within groups decreased as load increased. The design of the central portion of the HP may have contributed to the decrease in angular deformation. The weakest portion of a bone plate was where a screw hole is present, while the strongest portion was the solid portion between the screw holes. This was due to the second moment of area, also known as the area moment of inertia (AMI), of the plate. The bending stress developed in the plate during loading was inversely proportional to the AMI, this relationship was given by the flexural formula (see Equation D in Appendix 3). The AMI is a geometrical property (see Equation E in Appendix 3), which is related to the amount of material in a given region, therefore, the

AMI was higher in the solid portion of the plate than it was in the region where a hole was present.

In the LC-DCP for example, the AMI in the solid region with respect to the axis of bending was 28.13 mm^4, in comparison to the region where a hole was present, where the AMI was 10.26 mm^4 (Figure 1-30).

Figure 1-30. Cross-section of the LC-DCP. The figure on the left is the solid section of the plate where the bend occurs; the figure on the right is the section where a hole was present.

The bend in the plates for pancarpal arthrodesis occured between the fourth and fifth screw holes to correspond with the radio-carpal joint. The HP had approximately 8 mm of metal between the fourth and fifth screw holes in comparison to the LC-DCP, which had half (4 mm) of that length. More importantly though, was the AMI at the location of the bend, which for the LC-DCP was 28.13 mm^4 (provided by Synthes) and for the HP was approximately 35.44 mm^4. The large difference in the AMI of the plates was attributable to the variation in the cross-sectional areas (CSA), the HP had a CSA in the area of the bend of 32.64 mm^2, and the LC-DCP had a CSA of 26.65 mm^2, a difference of 22.5% with respect to the LC-DCP. This further exemplified the importance of a functional bending press, which forced the bend to occur on the solid section of the plate. If standard bending techniques were used, and a bend was placed into the section

where a hole occurred, the difference between the plates and the inherent weakness of the LC-DCP would have been even further magnified.

It should be noted that the deformations documented in the FEA did not correlate very well with experimental data. However, the FEA was not meant to simulate the experiment, it was only meant to validate theoretical calculations based on the different cross sections of the two plates. Since theoretical analysis was the basis of the hypotheses, the FEA was used as a way to non-destructively examine the mechanical response of the plates when subjected to bending. Angular deformation was documented as a way to analyze the entire construct, and not just the plate. The entire construct consisted of the plate itself, the bones and tissues making up the radiocarpal joint, and the screws, which attached them to each other. The rotary encoder data showed that the HP construct deformed approximately 23% less than the LC-DCP construct at all load levels. The FEA on the other hand, resulted in the HP deforming approximately 44% less than the LC-DCP under a given load (100 N). The large difference between the experimental and FEA results (see Appendix 4) could have been attributable to many factors, primarily involving the connection between the plate, screws, and the underlying bone. One factor, which could have contributed, was the presence of slippage between the plate and the bone in both constructs. This would undermine the strengthening effects of the HP design, and make the difference between the two constructs less defined. Such slippage could have arose under several conditions; if the screws were not tight enough, if the palmar aspect of the plate did not match the shape of the underlying bone as well as anticipated, or if the overall bone to plate contact area was reduced in one construct versus the other.

The plate strain was used to compare only the plate, as opposed the entire bone-plate construct like the angular deformation data provided. The HP experienced approximately 65% of the plate strain seen in the LC-DCPs at each load tested with significance seen at 80% BW and 120% BW, or 200 N and 300 N, respectively ($p<0.05$). Based on the linear relationship between stress and strain in the elastic region governed by the constitutive equation known as Hooke's Law (see Equation C in Appendix 3), in combination with the flexural formula, the correlation between the AMI and the plate strain experienced was also inversely proportional (see Equation F in Appendix 3).

Theoretical results provided by the FEA were in good general agreement with the experimental results. As stated earlier, the AMI of the HP was approximately 26% greater than that of the LC-DCP (at solid section level), and the recorded plate strains of the LC-DCP were approximately 36.7% greater than that of the HP. Although they are not directly related (axial strain and von Mises stress) the results of the FEA (see Appendix 4) did correlate very well with the recorded strain measurements on the dorsal aspect of the plate. In the FEA, the surface von Mises stresses seen in the HP were approximately 38.3% less than that of the LC-DCP under a given load of 100 N.

The FEA results compared to the experimental results better when analyzing plate strain and stress than they did when investigating angular deformation. This was due to the fact that both the experimental data on plate strain and the FEA results on von Mises stresses did not take construct variables into account, such as slippage and bone to plate contact area. Variations between the theoretical and experimental results may have been due to the plastic deformation that occurred to the plates during pre-bending, which would have altered their cross sections and their resultant AMIs. Further investigation of

the correlation between surface strains measured experimentally and theoretically is suggested.

One of the goals of this study was to develop a clinically usable bending press, which could produce a bend in plates that was both consistent and functional. The consistent location and degree of bend was achieved as shown in Figures 1-25 and 1-26. The increased bone-to-plate contact area enabled with the type of bend produced with the MSU BP is shown in Figure 1-27. One design flaw of the MSU BP was that, despite precautions taken to distribute the force of the bend over the entire width of the plate, a dent on the middle of the dorsal surface was still present (Figure 1-31).

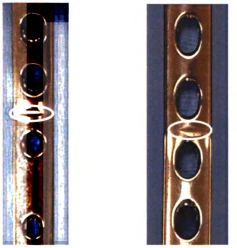

Figure 1-31. Close-up dorsal view of HP (left) and LC-DCP (right) after bending with MSU BP. Significant denting still occurred in the central region of the plate (circled in white).

An improvement to the design of the bending press would be to increase the diameter of the fulcrum to more accurately match the dimension of the dorsal and palmar aspects of the plates. The current diameter focused the force over too small of an area and caused the denting. With knowledge of the exact measurements of the plate surfaces, matching the radii of the fulcrum and contact point to the dorsal and palmar aspect of the plates, respectively, would also reduce the effect of the high stresses generated, thus

eliminating the presence of a dent. This dent proved to not be as significant of a concern as initially anticipated, because the strain gages were small enough to be placed outside of the dent area (see Figure 1-15).

CONCLUSION

The HP has been designed for use in the canine pancarpal arthrodesis procedure in place of a traditional LC-DCP plate, which is a good general use plate. The HP was specifically designed to address the complications of wound dehiscence and post-operative metacarpal fractures associated with pancarpal arthrodesis. One clinical study, using varying plate sizes with 10° of hyperextension, stated that 74% of 45 dogs returned to normal walking and running on the leg, with 97% clinically improved to a degree that the owners expressed satisfaction with the procedure.[2] Another study reported that arthrodesis occurred in all thirteen antebrachiocarpal joints implanted with a HP.[9] Based on Li's study, the HP has been shown to be an effective implant when performing a pancarpal arthrodesis in canines and is currently recommended for clinical use.

Based on the results of the current study, it was concluded that the HP yielded a biomechanically superior construct than the LC-DCP. Results of the current study indicated that the use of a HP for pancarpal arthrodesis provided a construct that was more resistant to angular deformation and experienced less plate strain than a LC-DCP. The biomechanical advantage gained with a HP construct may decrease the likelihood of implant related complications and lessen the need for long-term postoperative coaptation with no additional time or complexity in the surgical procedure.

REFERENCES

1. Lesser AS. Arthrodesis. In: Slatter D, *Textbook of Small Animal Surgery*. Saunders, Philadelphia, 2003; 2174-2176

2. Parker RB, Brown SG. Pancarpal arthrodesis in the dog: A review of 45 cases. Vet Surg 1981; 10: 35-43

3. Early TD. Canine carpal ligament injuries. Vet Clin North Am Small Anim Pract. 1978; 8: 183-199

4. Gambardella PC, Griffiths RC. Treatment of hyperextension injuries of the canine carpus. Compend Contin Educ Pract Vet 1982; 4: 127-132

5. Fogle B. The Encyclopedia of the Dog. 1st ed. New York: DK Publishing, 1995

6. Evans HE: Miller's Anatomy of the Dog, 3rd ed. Philadelphia: WB Saunders Co, 1993

7. Piermatti DL, Flo GL. *Handbook of Small Animal Orthopaedics and Fracture Repair.* 3rd ed. Philadelphia: WB Saunders, 1997; 344-348, 361-370

8. Pederson NC, Morgan JP, Vasseur PB. Joint diseases of dogs and cats. In: Ettinger SJ, Feldmen EC, eds. *Textbook of Veterinary Internal Medicine.* 5th ed. Vol 2. Philadelphia: WB Saunders, 2000

9. Li A, Gibson N, Carmichael S, Bennett D. Thirteen pancarpal arthrodesis using 2.7/3.5 mm hybrid dynamic compression plates. Vet Comp Orthop Traumatol 1999; 12: 102-107

10. Okin R. Carpal arthrodesis in a cat with radial nerve damage. Fel Pract 1982; 12: 18-20

11. McKee M. Intractably painful joints. In: Houlton JE, Collinson RW, eds. *Manual of Small Animal Arthrology.* Gloucestershire: British Small Animal Veterinary Association, 1994: 122-125

12. Chambers JN, Bjorling DE. Palmar surface plating for arthrodesis of the canine carpus. J Am Anim Hosp Assoc 1982; 18: 875-882

13. Whitelock RG, et al. Metacarpal fractures associated with pancarpal arthrodesis in dogs. Vet Surg 1999; 28: 25-30

14. DeCamp CE, Soutas-Little RW, Hauptman J, et al. Kinematic gait analysis of the trot in healthy greyhounds. Am J Vet Res 1993; 54(4): 627-634

15. Hulse D, Hyman W, Nori M, Slater M: Reduction in plate strain by addition of an intramedullary pin. Vet Surg 1997; 26: 451-458

16. Johnson AL, Hulse DA. Diseases of the joints. In: *Small Animal Surgery*. Mosby Inc., St. Louis 2002; 1091-1093

17. Hibbeler RC. *Mechanics of Materials*. 3rd ed. Upper Sadle River: Pearson Prentice Hall, 2004

18. Pohler O, Straumann F. The effect of pin size on reducing bone plate strain. Vet Comp Orthop Traum 2000; 13: 185-19

19. Black J. *Biological Performance of Materials*. 2nd ed. New York: Marcel Decker, 1992

20. Marcellin-Little DJ, Deyoung BA, Doyens DH. Canine uncemented porous-coated total hip arthroplasty: results of a long-term prospective evaluation of 50 consecutive cases. Vet Surg 1999; 28: 10-20

CHAPTER TWO

MECHANICAL EVALUATION OF AN INTERLOCKING NAIL LOCKED WITH EITHER BOLTS OR A TYPE-IA EXTERNAL SKELETAL FIXATOR IN A SIMULATED CANINE TIBIAL MODEL

ABSTRACT

Interlocking nails (ILNs) can be implanted with small remote surgical approaches, thus preserving soft tissue integrity and minimizing disruption to local vasculature. This technique is synergistic with the trend toward biological fracture management. Due to their biological advantages, the use of ILNs has gained popularity amongst orthopedic surgeons in recent years. Nevertheless, with increased use, several limitations have also been documented, both clinically and experimentally. Recently, an investigational ILN system, featuring extended modified bolt-pins coupled to a type-IA external skeletal fixator (ILN-ESF), has emerged as a technique to augment the stability of an ILN. The extended bolts are used to lock the ILN, while serving as connecting pins for the ESF frame. The purpose of this study was to use a tibial gap fracture model, featuring a synthetic bone substitute to mechanically compare ILN-ESF and standard bolted ILN (ILNb) constructs in torsion, 4-point bending and axial compression. The hypothesis was that the ILN-ESF would be less compliant and sustain less deformation than a bolted nail construct.

To reduce specimen variability, custom-made synthetic tibial bone substitutes were used in this study. The tibial bone substitutes were implanted with standard ILNs locked with either bolts or extended bolts connected with an ESF. Constructs were tested

in torsion, bending and axial compression (n=4/testing mode). Data, consisting of construct compliance and associated deformation, were compared using t-tests.

The results of this study indicated that the ILN-ESF construct compliance and deformation was significantly less than those of the ILNb construct in torsion, bending and compression. Slack was present in the ILNb construct under torsion and bending, but not in the ILN-ESF construct, regardless of testing mode.

This study showed that the substitution of locking bolts with extended bolts connected to an ESF significantly reduced the construct compliance and overall deformation in torsion, bending, and compression. Furthermore, the inherent slack of the ILNb was eliminated by the use of an ESF in torsion and bending. The improvement in structural properties of the ILN-ESF constructs could diminish interfragmentary motion at the fracture site and potentially improve bone healing.

INTRODUCTION

Due to an advanced understanding of both human and veterinary fracture healing, the concept of biological fracture fixation has evolved greatly over the past two decades. The goal of biological fixation, particularly in comminuted long bone fractures, is to achieve a balance between mechanical stability of the fracture repair and biological preservation of the soft tissue.[1,2] From a biomechanical standpoint in particular, the function of fracture fixation is to provide sufficient stability, meaning that the interfragmentary movement that occurs under external loading and muscle forces is reduced to a degree which allows bone healing to occur.

Traditionally, it has been felt that comminuted long bone fractures were best managed by bone-plating techniques (Figure 2-1). Proper application of bone plates provides mechanical stability by counteracting axial (compression and tension), bending, and rotational forces.[3,4]

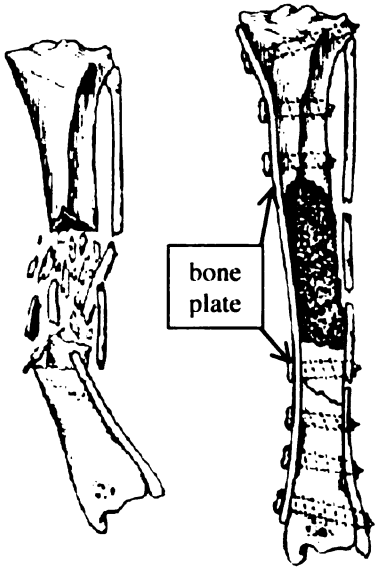

Figure 2-1. Comminuted long-bone (tibia and fibula) fracture, before (left) and after (right) fixation with a medially applied bone-plate.[5]

Despite their potential mechanical advantages, bone-plating techniques often require extensive soft tissue dissection and operative time. It has also been shown that the pressure of the plate on the surface of the bone can have detrimental effects on the vascularization.[6-9,32] The end result may be slower bone healing and increased post-operative morbidity.

As an alternative to bone plates, interlocking nails (ILNs) have been introduced for internal fracture fixation. Interlocking nails can be inserted into the bone with minor surgical approaches, away from the traumatized area; thus preserving soft tissue integrity and minimizing disruption to local vasculature and fracture hematoma.[6-9] Interlocking nails provide a connection between the bone and nail, both proximal and distal to a fracture site (Figure 2-2).

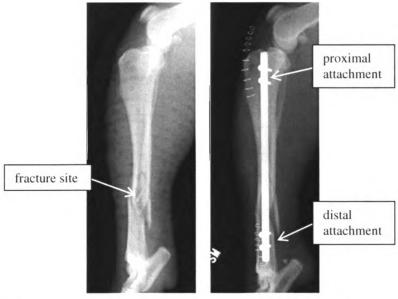

Figure 2-2. Mediolateral radiograph of a tibial fracture (left) internally fixated with an interlocking nail (right). [MSU SACS*]

* MSU SACS: *Michigan State University Small Animal Clinical Sciences.* College of Veterinary Medicine, Michigan State University. East Lansing, MI.

Several large clinical studies have reported good to excellent healing results and low complication rates with the use of ILNs in both animals and humans.[8-10] Due to their biological advantages, the use of ILNs has gained popularity amongst orthopaedic surgeons in recent years. Nevertheless, with increased use several limitations have been documented, both clinically and experimentally.[9-16] A recent *in vivo* study with an ILN showed a significant reduction in bone healing and functional recovery attributed to torsional and bending instabilities, when compared to an external fixator in an ovine tibial fracture model.[11] Similarly, an *in vitro* study of nine different human ILN designs implanted in cadaveric tibiae demonstrated that consistent slack was present in all constructs in torsion regardless of nail design.[15] Finally, a recent *in vitro* study[16] showed that torsional compliance of ILNs was indeed greater than that of a plate and intramedullary rod (IMR) combination (PRC); a fixation device often used in the treatment of comminuted fractures. In addition, a mismatch between screw and nail-hole diameter (Figure 2-3) was also identified in the ILN. This mismatch allowed movement of the nail prior to engagement with the screw.

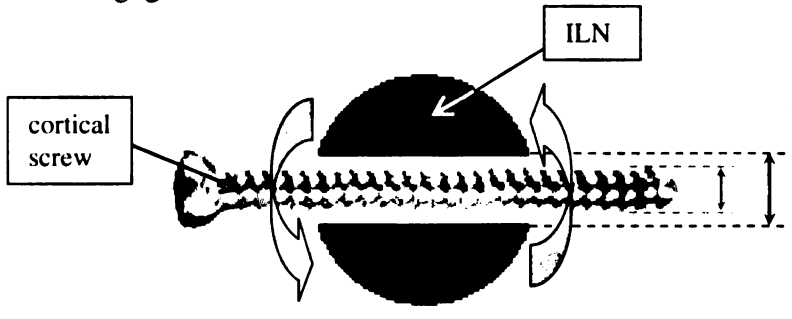

Figure 2-3. Diagram of mismatch between screw diameter (gray) and the ILN hole diameter (black).

As a result, significant rotational instability (~25° slack) was still present following the locking of the screw to the bone. In addition, structural deformation (flattening) of the screw threads further increased the relative mismatch between the nail hole and screw

diameters, thus potentially accentuating the magnitude of the slack over time. These studies suggest that current human or veterinary ILNs may have inherent torsional instabilities, which could contribute to delayed bone healing and implant fatigue failure such as clinically described screw bending or breakage.

To address the instabilities associated with ILNs, several modifications have been devised. These can be divided into two major groups. The first group includes modifications in the nail and/or screw designs. Based on a recent mathematical evaluation of ILNs,[14] replacement of the locking screws with similar sized bolts was recommended. The goal was to increase the stiffness of the locking mechanism by providing a solid bolt-nail interface.[8,17] The bolts are threaded to lock on the cis-cortex of the bone, but otherwise feature a smooth core that slides into the corresponding nail hole (Figure 2-4).

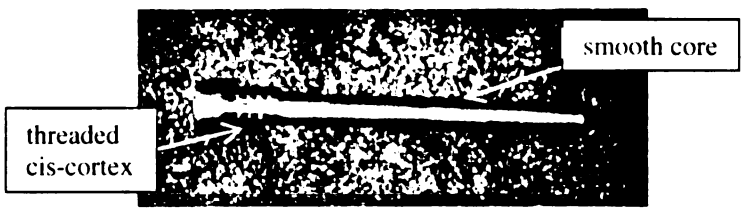

Figure 2-4. Bolt for ILN, featuring a threaded cis-cortex section and a smooth, solid core.

The second group that addresses ILN instability supplements the ILN systems with other modes of fixation,[17-19] such as stack pinning, double ILNs, ILN combined with an intramedullary rod, and most recently an ILN with proximal "tie-in" configuration. All of the above techniques, however, have the potential to increase surgical time, invasiveness, and morbidity; thus defeating the biological purpose intended with the interlocking nail technique.

External skeletal fixation (ESF) offers yet another alternative for fracture reduction and stabilization. An ESF is a device, which stabilizes fractures with utilization of several trans-osseous pins connected to one or more external bars (Figure 2-5).

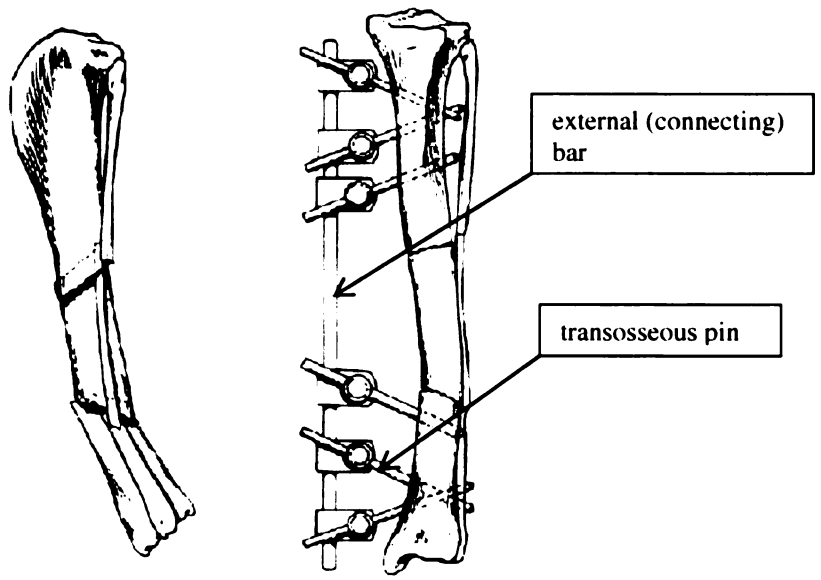

Figure 2-5. Comminuted long-bone (tibia and fibula) fracture, before (left) and after (right), being externally fixated with a type-IA external fixator.[5]

Depending on the configurations of the pins and bars, ESFs are further classified into type-IA or IB (Figure 2-6), type-IIA or IIB (Figure 2-7), or type-III (Figure 2-8) with increasing number of transosseous pins and connecting bars.[5,20]

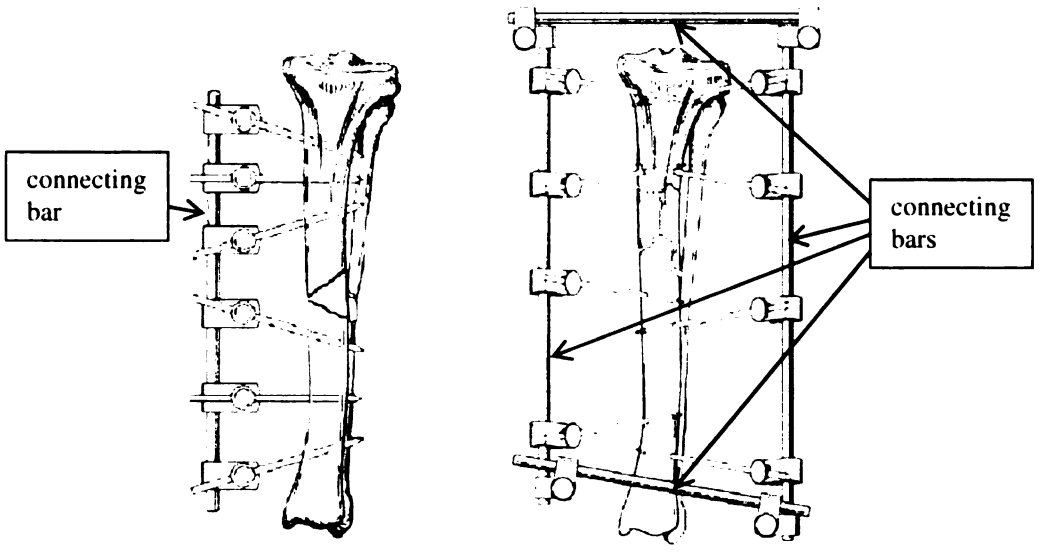

Figure 2-6. Type-IA (on left) is a one-plane, unilateral fixator with 6 transosseous pins (half pins) and one connecting bar. Type-IB (on right) is a two-plane bilateral fixator with 8 transosseous pins (half pins) and four connecting bars.[5]

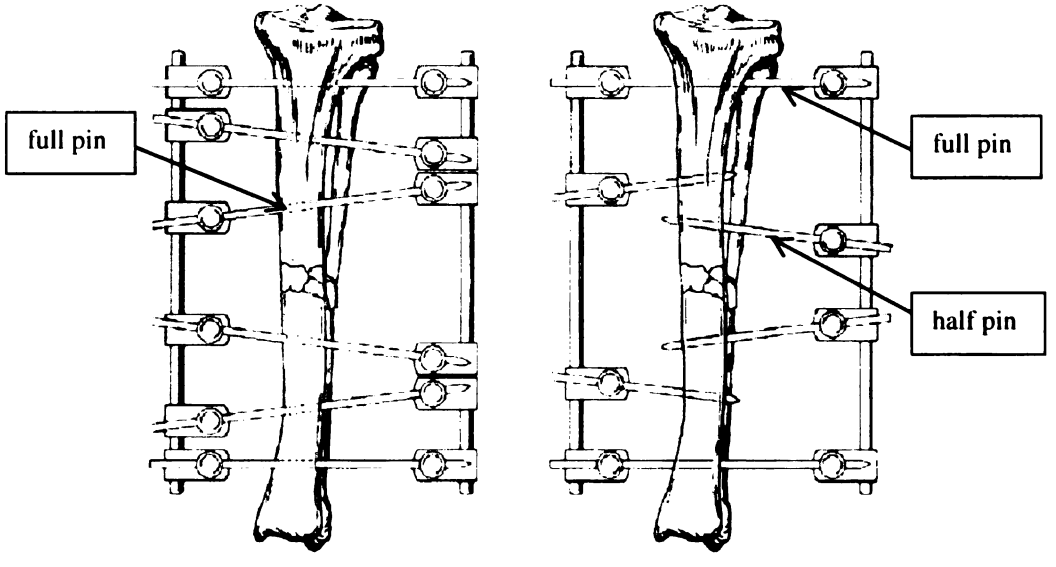

Figure 2-7. Type-IIA (left) and type-IIB (right) ESFs. Notice the full pins in the type-IIA and the full and half pins in type-IIB. The use of half pins results in a slight loss of stiffness compared to a full-pin configuration.[5]

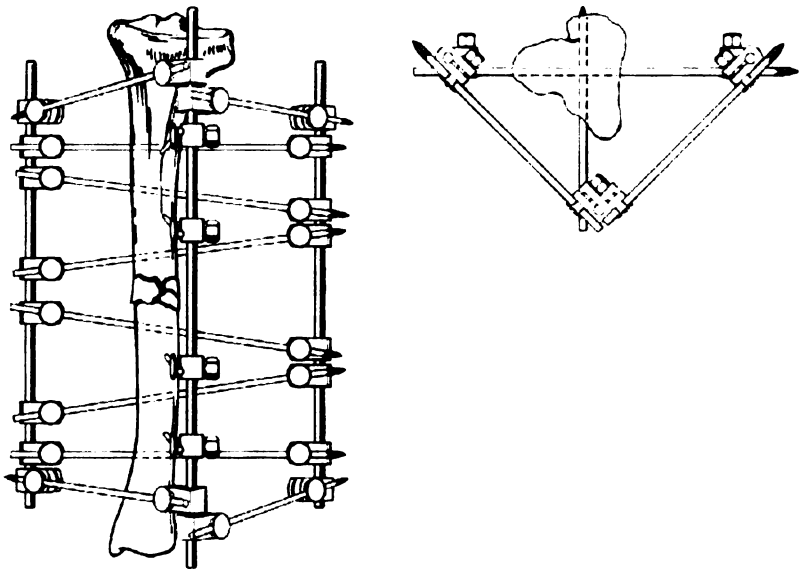

Figure 2-8. Type-III ESF, notice the bilateral and biplanar configuration.[5]

Similar to ILNs, ESFs can achieve the goal of biological fixation with a minimally invasive or percutaneous (closed) surgical approach to help preserve the soft tissue environment. Studies have shown that the mechanical properties of the ESF are dependent on the overall frame configuration.[21] Geometric parameters influencing the stability of fractures stabilized with external fixation include: transosseous pin diameter, connecting bar diameter, free length between the connecting bar and the bone, distance between the inner pin and the fracture site, and the distance between pins (Figure 2-9).

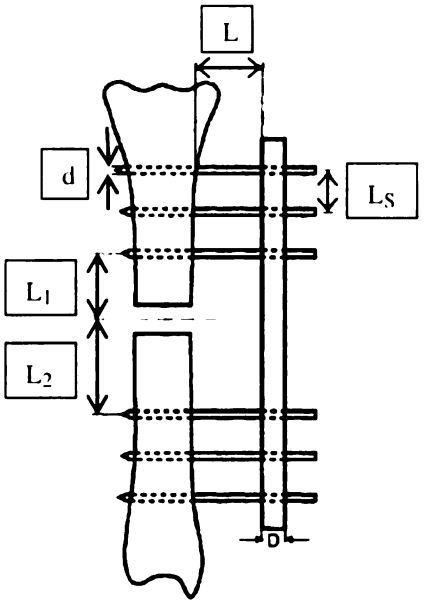

Figure 2-9. Geometric parameters influencing fracture stabilization with an ESF,[22] where:

d: transosseous pin diameter

D: connecting bar diameter

L: free length between the connecting bar and bone

L_1,L_2: distance between pin and fracture site

L_S: distance between pins

In general terms, the construct stability may be increased by increasing the number of pins and/or connecting bars,[5,20,23] with type-I configurations (made of half trans-osseous pins and a connecting bar in one plane only) being the weakest of all ESF frames. However, the improved stability achieved with the addition of pins and bars in various planes, may come at the expense of post-operative morbidities such as increased risk of pin tract infection, extensive muscle impalement, and increased bulkiness of the apparatus. For this reason, simple type-I ESFs are often used as adjunct fixations to complement and strengthen a primary mode of fixation, such as an IMR.

Recently, an investigational hybrid ILN, featuring extended modified bolts-pins coupled to a type-I ESF (ILN-ESF), has emerged as yet another technique to augment the

stability of an ILN.[18,24] The hybrid bolt-pins are used to lock the ILN while serving as connecting pins for the ESF frame (Figure 2-10).

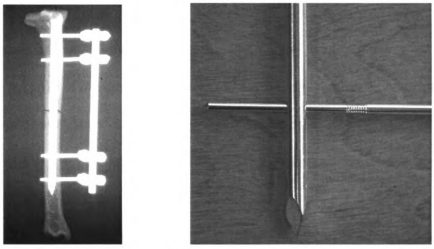

Figure 2-10. (Left) Radiograph of a tibial specimen implanted with the investigational hybrid bolt-pin locked with a type-IA external skeletal fixator. [SCSRS*] (Right) A close-up photograph of the hybrid 2.7mm ILN bolt/3.2mm ESF pin passing through one of the nail holes.

By combining the ILN to an ESF, the instabilities associated with each separate system should theoretically be eliminated by the other, while retaining their own unique biological and mechanical advantages. For instance, seated along the neutral axis of the bone, ILNs have bending and torsional stiffness proportional to the cross section of the nail. Specifically, the area moment of inertia (AMI) and polar moment of inertia (PMI) are structural properties that characterize the ability of an implant to resist bending and torsional deformation, respectively. Design consideration of these structural properties allows ILNs to counteract bending and torsional forces deleterious to bone healing. Further, by combining a simple type-I ESF with an ILN, substantial bending and rotational stability may be achieved without utilization of a type III ESF, which is often associated with a high rate of postoperative morbidity. This technique was successfully

* SCSRF: *South Carolina Surgical Referral Service*. Columbia, SC.

used in a limited number of clinical cases in small animal surgery.[19,24] A prospective study, by Basinger et al., showed encouraging clinical use of the investigational hybrid ILN-ESF construct in dogs.[19] Despite their clinical success, the proposed mechanical stability has not been validated in an experimental setting.

The purpose of the current study was to use a tibial gap fracture model featuring a synthetic bone substitute designed by the Comparative Orthopaedic Investigations Laboratory (COIL) at Michigan State University, to mechanically compare hybrid ILN-ESF and bolted ILN (ILNb) constructs in torsion, 4-point bending, and compression. Several objectives were deemed necessary in the overall preparation and testing of these specimens. Because instability has been shown to be present in the ILN systems in previous studies,[11,15,16] it was important to create a similar environment for the nail with the synthetic bone model. For this to occur, consistent placement of the ILNb and ILN-ESF constructs was absolutely necessary. Therefore, a goal was to develop several custom designed fixtures which would allow consistent and accurate placement of the fixators in the bone model. The ultimate goal was to acquire data that would support application of the ILN-ESF in a wider range of clinical circumstances, including human orthopaedics. The hypothesis of the study was that the ILN-ESF would be less compliant than the ILNb in torsion, bending, and compression. We further hypothesized that the use of an ESF would dampen or eliminate the acute torsional and bending instability (slack) characteristic of standard nails.

MATERIALS AND METHODS

Specimen Preparation

Bone Model – In an attempt to limit specimen variability and circumvent the need to procure canine bones, a custom-made synthetic tibial model was used in this study. The material used for the bone model was 30% glass-filled structural nylon (Part No. P0304909, 30% GF nylon natural, Alro Plastics, Jackson, MI). This material was chosen on the basis of its material properties, which are similar to those of cortical bone (Table 2-1). To mimic a gap-fracture model, specimens were manufactured in 2 symmetrical halves. Each half of the bone model featured a segment used for linkage to the holding fixtures (cupping section), a tapering segment representing the metaphyseal section, and a final segment representing the diaphyseal section (Figure 2-11). Thickness of the wall was 2.5 mm throughout. Dimensions for the synthetic bone model were determined on the basis of morphometric analysis conducted by Michigan State University Small Animal Clinic (MSU SACS) on canine tibiae obtained from dogs weighing between 30 and 35 kg. The overall length of the tibial model (between each holding fixture and including a 50 mm central gap) was 210 mm. Machining of the bone model, reducing it from a solid rod to the bone model tube, was done by Olympia Tools (St. Johns, MI)

Property	Human cortical bone range; average	Canine cortical bone range; average	30% glass filled structural nylon range; average
UTS (MPa)	53 – 135; 106.8 [25]	NA	65 - 195; 140
UCS (MPa)	145 – 167; 158.8 [25]	112.8 [25]	140
USS (MPa)	68 [26]	NA	59 - 85; 72
Young's modulus: E (GPa)	8.2 – 17; 14.9 [27]	12.26 [25]	7.2
Poisson's ratio	0.46 – 0.58; 0.49 [27]	NA	0.35
Density (g/cm^3)	1.9 [28]	0.84 [29]	1.35

Table 2-1. Comparative material properties of human and canine cortical bone and of the composite material used in this study. Where UTS, UCS and USS is Ultimate tensile, compressive and shear strength, resectively. [25-29]

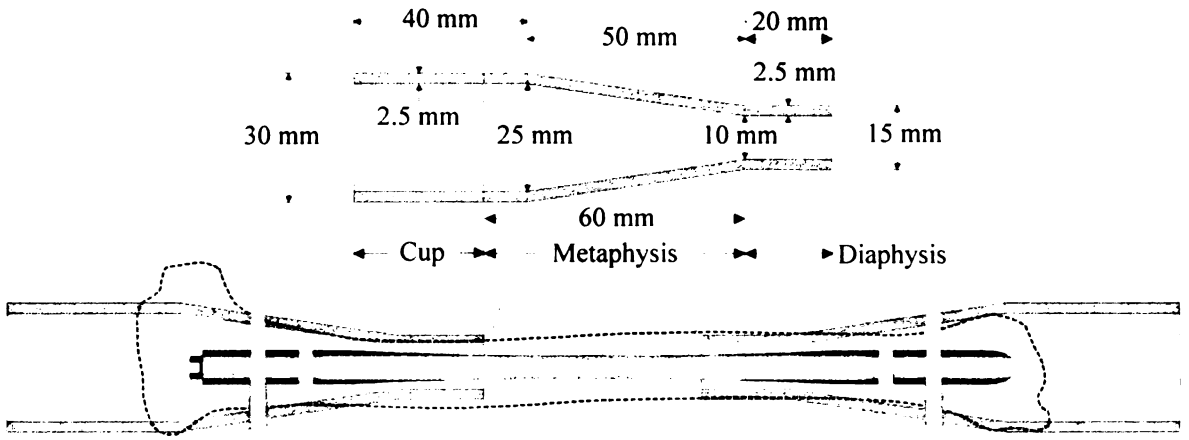

Figure 2-11. Schematic depiction of the synthetic bone model (30% glass-filled nylon composite) with the various dimensions of each segment (top) and a schematic depiction of the outline of an actual canine tibia and fibula (red and gray dotted lines, respectively) superimposed over a completed bone model with a novel ILN with 2 of the 4 locking SCPs (bottom).

Drilling Fixture – To allow accurate and consistent placement of the bolts and hybrid bolt-pins, a dedicated custom-designed drilling fixture was fabricated to drill 2 pilot holes in all bone models (Figure 2-12). The centers of the holes were exactly 11 mm apart to match the nail holes.

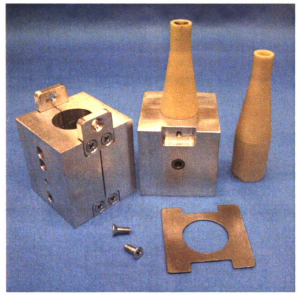

Figure 2-12. Partially disassembled drilling fixture, with the top portion on the left and the bottom on the right. The cupping section of the bone model is inserted into the bottom portion with the metaphyseal and diaphyseal sections still visible. A spacer for minor adjustment is also shown.

The drilling fixture featured a design made of three main pieces, consisting of a top portion, which split into two symmetrical halves, and a bottom portion. There was also a spacer made to compensate for minor variations in bone length due to machining tolerances. The three-piece fixture allowed the bone to be placed into the fixture by removing the symmetrical halves of the top portion, which featured removable drill guides (Figure 2-13).

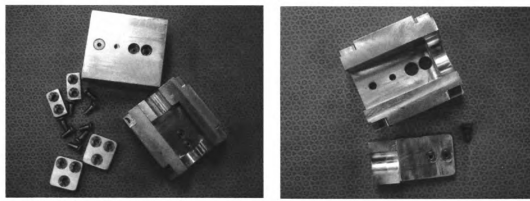

Figure 2-13. Top portion of drilling fixture, with symmetrical halves shown on the left and the removable drill guides shown on the right.

Beyond locating two points which were 11 mm apart to drill the pilot holes, it was important to ensure that these pilot holes were drilled perpendicular to the axis of the bone, and not just normal to its slanted metaphyseal surface (Figure 2-14).

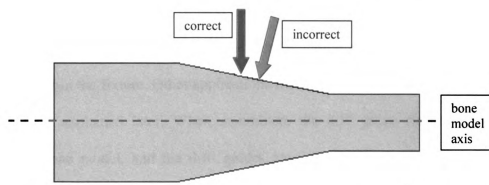

Figure 2-14. Schematic of correct (green) and incorrect (blue) way to drill pilot holes.

This was enabled by the design of the removable drill guides, which featured a geometry matching the slope of the metaphyseal section of the bone model (Figure 2-15). The drill guides also featured a radius, which matched that of the diaphyseal section of the bone. An additional feature of the drill guide fixture was that the removable guides were designed so that bushings of various sizes could be interchanged to accommodate for

various screw and bolt sizes.

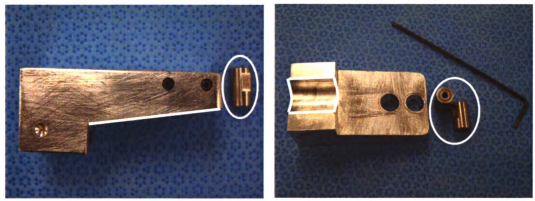

Figure 2-15. Removable drill guide, featuring a geometry matching the slope of the metaphyseal section of the bone model (white line), a radius matching the diaphyseal section (white rectangle), and interchangeable bushings for various bolt and screw sizes (white ovals).

The bone was constrained axially and transversely by the radii of the removable drill guides and the base of the bottom portion of the fixture, which matched the cupping section of the bone model. The bottom portion of the fixture also featured two pairs of steel bushings oriented perpendicular to each other, which restricted movement of the bone model within the fixture. Other applications for the locking holes in the bone model will be further explained later. When assembled, the drill guide fixture completely enclosed the bone model, and the drill guides ensured that the drill bit was directed throughout its path into the bone model (Figure 2-16). This standardized procedure allowed all nails to be precisely and reliably centered longitudinally within the bone model. Detailed drilling fixture operating instructions are found in Appendix 1.

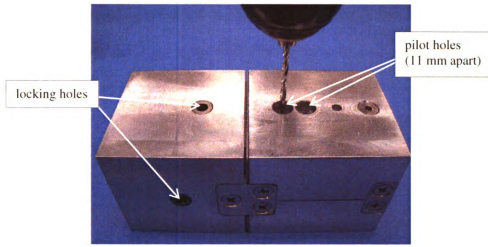

Figure 2-16. Assembled bone drilling fixture, with bone model enclosed. A hand held drill is shown drilling pilot holes.

Construct Preparation

Foam Plugs – Custom-made polyurethane foam plugs were inserted at the ends of each bone model to maintain the ILNs in a centralized position during testing. The foam plugs were meant to simulate cancellous bone in the metaphyseal section of the tibia. The foam plugs were made of a two-part mixture molded into tubes. These tubes were then reduced to dimensions fitting the inside of the metaphyseal section of the bone model by a custom designed lathe tool (Figure 2-17).

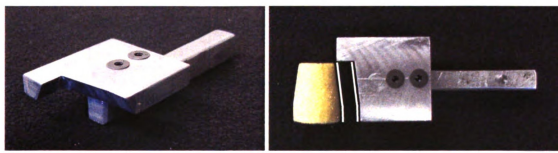

Figure 2-17. Custom designed lathe tool, which created a geometry matching the inside of the metaphyseal section of the bone model (shown in white).

The foam plugs were designed to grasp only 1-2 mm of the proximal and distal ends of the nail. After lathing, the foam plugs were inserted into the ends of the bone (Figure 2-18). Detailed foam plug instructions are given in Appendix 1.

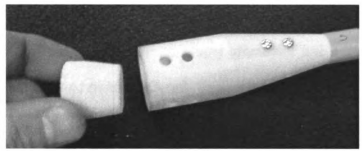

Figure 2-18. Foam plug insertion into the bone model.

Construct Alignment Fixtures – An alignment fixture was used during implantation to ensure that all of the nails were also axially aligned within the bone models (Figure 2-19). The alignment fixture for the ILNb constructs featured two sliding frames which held the bone model, and a fixed nail-clamping piece that matched the diameter of the nail.

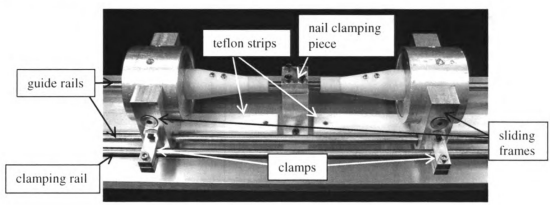

Figure 2-19. ILNb alignment fixture.

The basic construction of the ILNb alignment fixture consisted of a base with two Teflon strips which were in contact with the base of the sliding frames. The sliding frames served as a method of holding the potting, which was directly attached to the bone model

(potting discussed later). The sliding frames, equipped with brass bushings and clamps, were attached to two guide rails and a third rail, which could be clamped to secure location of the cups. When the nail was in the proper position with respect to the bone, the bolts or hybrid bolt-pins were inserted.

Another fixture was used to ensure proper alignment and distance relationships between the ILN and external fixator (3.5 cm) (Figure 2-20).

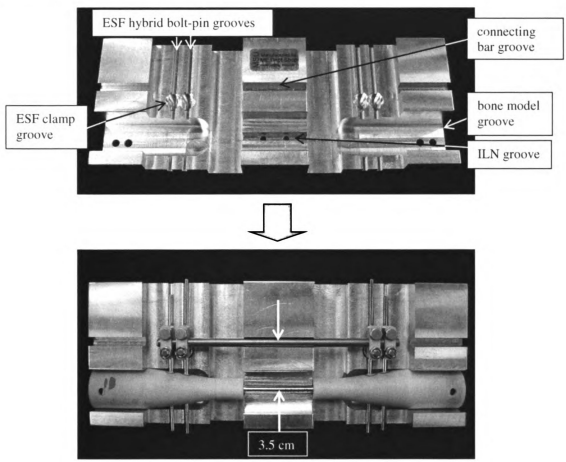

Figure 2-20. ILN-ESF alignment fixture.

The ILN-ESF alignment fixture consisted of one solid block of aluminum. The block was milled to place the ESF at the desired location with respect to the bone and ILN. Location of the ESF was insured by grooves in the aluminum block, which restricted movement of

the ESF connecting bar, the ESF clamps, the ESF hybrid bolt-pins, the bone model, and the ILN. Detailed alignment fixture instructions are given in Appendix 1.

ILN-ESF Tightening – The ESF connecting bar was attached to the hybrid bolt-pins via four clamps (SK™). To ensure consistency, all clamps were tightened to the same torque (4.5 Nm). This was done using a digital torque wrench (CDI Computorq II, City, State [Figure 2-21]).

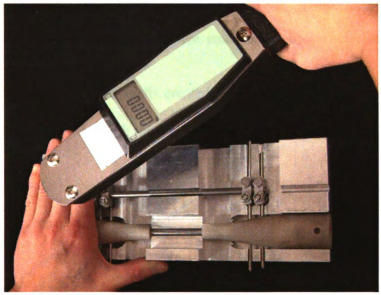

Figure 2-21. CDI Computorq digital torque wrench shown tightening ESF clamps.

Potting Fixture – A uniform potting system was created in an effort to reduce specimen variation. The potting was essentially the connection between the specimen and the mechanical testing environment. In previous studies,[16] an epoxy had been used to create a solid environment in which load could be transferred from the machine to the construct. The actual procedure of potting specimens proved to be quite tedious, messy, and prone to variation. With this in mind, an aluminum potting fixture was custom designed to fit

the bone models. The potting fixture featured two sections, an inner and outer shell (Figure 2-22).

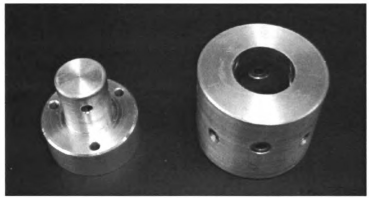

Figure 2-22. Disassembled potting fixture, inner shell (left) and outer shell (right).

When joined, the inner and outer shells created an inner and outer diameter matching the cup section of the bone model with minimal tolerance (<0.01 mm [Figure 2-23]).

Figure 2-23. Assembled potting fixture with bone model inserted.

The aluminum pots were equipped with two pairs of axially aligned thru holes, equipped with hardened steel bushings, which spanned the entire diameter of the potting. The potting fixture also featured four threaded holes (oriented 90° from each other) with steel

threads which were used to lock the potting fixtures into various cups of the mechanical testing fixtures (Figure 2-24).

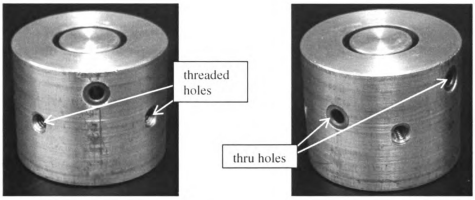

Figure 2-24. Potting fixture, which featured perpendicularly oriented thru holes for locking bone to potting fixture and threaded-holes for locking potting fixture to testing fixture cups.

The drill guide fixture and potting were both designed so that the holes drilled in the cupping section of the bone were aligned with the thru holes in the potting fixture. Locking pins were then placed into the holes to rigidly attach the bone model to the potting (Figure 2-25).

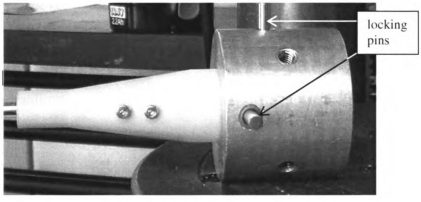

Figure 2-25. Potting fixture with partially inserted locking pins installed. The assembled construct is shown.

Study Design

All ILNs in this study were 6 mm (diameter) by 185 mm (length) nails with 2 proximal and 2 distal 2.7 mm (diameter) holes. The corresponding locking bolts (2.7 mm in diameter) and the ILNs were obtained from Innovative Animal Products, Rochester, MN.

Each ESF frame was composed of 4 hybrid 2.7 mm ILN bolt/3.2 mm ESF pins and 1 small SK™ titanium connecting bar (6.3 mm [diameter] by 150 mm [length]). The hybrid bolt-pins were coupled to the connecting bar via 4 small SK™ clamps. All ESF frames were obtained from IMEX Veterinary Inc., Longview, TX.

Implants were applied to the synthetic tibiae in 2 groups for a total of 12 specimens per group (n=4/testing mode). Group 1 (ILNb) was made up of 6 mm x 185 mm ILNs with four 2.7 mm bolts. Group 2 (ILN-ESF) was made up of 6 mm x 185 mm ILNs with four hybrid 2.7 mm ILN bolt/3.2 mm ESF pins.

Mechanical Testing

Using custom designed loading fixtures, all specimens were mounted in an Instron servo-hydraulic testing machine (Instron model 1331, Instron Corp., Canton, MA) coupled to a 2500 lb (11,120 N) axial load cell (Model 1010AF-2.5K-B, Interface Inc., Scottsdale, AZ). The loading fixtures dedicated to bending and torsion were instrumented with rotary encoders to document angular deformation of the constructs. In addition, the torsion fixture was instrumented with a 1200 lb*in (135 N*m) torque load cell (Model 5330-1200, Interface Inc., Scottsdale, AZ) to further document the magnitude of the applied torques. All specimens were tested non-destructively in torsion, 4-point bending,

and compression (n = 4 per testing protocol). All tests were run in load control for 10 cycles. The actuator displacement, rotary encoder output, and corresponding load/torque were documented in the tenth cycle. See Appendix 2 for detailed operating procedures for the torsion, bending, and compression tests.

Torsion Tests – Torsion tests were run using a 0.125 Hz sinusoidal waveform at a torque level of ± 5 Nm. This frequency was established in pilot tests and was based on the frequency that generated minimal electrical noise in the response of the constructs during this type of loading (where slack is present, such as in ILNb constructs). The torque level chosen for this study was identical to that used in previous biomechanical investigations.[16,30] Torsion was achieved using a rack and pinion assembly that converted linear displacement of the actuator into rotation of the proximal cup, while the distal cup remained static. The torsion fixture was equipped with a rotary encoder (Baumer Electric, Southington, CT) used to record angular deformation and a torque load cell (Figure 2-26).

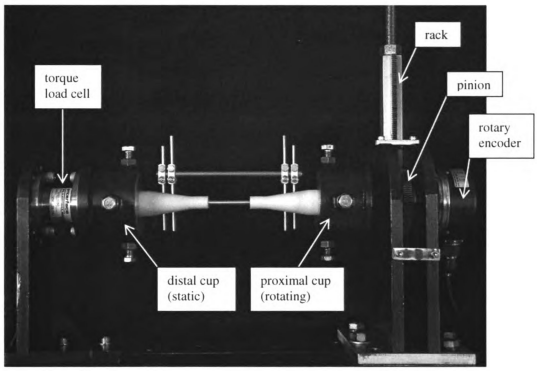

Figure 2-26. The torsion fixture shown with a loaded ILN-ESF.

Bending Tests – For purposes of this study, the constructs were only tested in mediolateral bending (see Appendix 4 for data). Bending tests were run using a 0.125 Hz sinusoidal waveform at a bending moment of ± 3.5 Nm. The bending moment chosen for this study was identical to that used in previous biomechanical evaluations of fixation devices in a gap fracture model.[16,30] A specially designed fixture allowed for application of a pure bending moment over the entire bone model/implant construct, as well as alternate bending in the medial to lateral and lateral to medial directions. The bending fixture had two cups, which articulated in one plane (mediolateral), equipped with rotary encoders (Renco Encoders Inc., Goleta, CA) used to record specimen angular deformation (Figure 2-27). The cups were attached to a loading arm, made up of a main cross bar and two linkage bars, which allowed rotation at two points (at the connection to the cup and at the main cross bar). The loading arm was attached to the axial load cell.

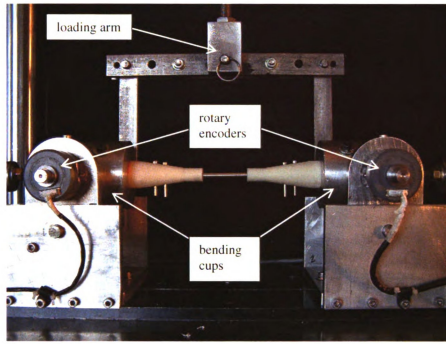

Figure 2-27. The bending fixture shown with a loaded ILNb.

Compression Tests – Compression tests were run using a 1 Hz haversine waveform to a peak load of 176 N. This load level was chosen to simulate post-operative loading conditions of a 30 kg dog. Therefore it was slightly less than the force acting on a healthy canine limb during trot.[31] Compression tests applied an axial load on the ILN through displacement of the actuator. The compression fixture consisted of the axial load cell and two compression cups to hold the potting fixtures (Figure 2-28).

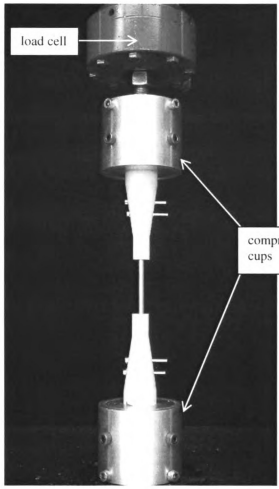

Figure 2-28. The compression fixture shown with a loaded ILNb.

Data Acquisition

A load cell and/or a torque load cell coupled to the Instron actuator and to the torsion fixture, respectively, recorded applied loads (N) and torques (Nm) over time. These and the actuator displacement (mm) were recorded at a sampling rate of 500 Hz (compression) and 250 Hz (bending and torsion). The difference in sampling rates between testing conditions was dictated by computers limitations in handling the size of the respective data files. Since all constructs were tested under load control, construct compliance (slope of deformation versus load curve) was evaluated in the 10^{th} cycle.

Construct compliance in bending and torsion was calculated as the mean compliances during positive and negative loading. Construct angular deformation (torsion and bending) was computed from the geometrical dimensions of the torsion and bending fixtures as well as from rotary encoder data, while construct linear deformation (compression) was obtained from actuator displacement data. See Appendix 2 for calculations for torsion and bending tests.

As specimens were loaded in bending tests, the proximal and distal angles (α and β, respectively) with respect to the horizontal were recorded via the rotary encoders affixed to each articulated mount. Angular deformation (γ) was computed with Equation 2-1 (Figure 2-29).

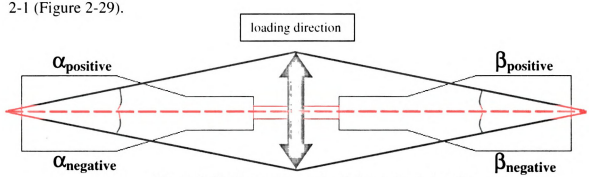

Figure 2-29. Construct angular deformation in bending

$$\gamma_{minimum} = \left| \alpha_{negative} + \beta_{negative} \right|$$
$$\gamma_{maximum} = \alpha_{positive} + \beta_{positive} \quad \textbf{[2-1]}$$
$$\gamma_{Total\ (full\ cycle)} = \gamma_{maximum} + \gamma_{minimum}$$

Equation 2-1. Angular deformation, where positive and negative are in reference to the applied moment, and:

γ : construct angular deformation
α : deformed construct angle recorded by a rotary encoder
β : deformed construct angle recorded by a rotary encoder

The results of compliance and associated deformation of ILNb constructs and ILN-ESF constructs were compared using unpaired t-tests. Student-Newman-Keuls post-hoc tests were used whenever significant differences were identified ($p < 0.05$).

RESULTS

Performance of Construct Development Fixtures

The goal of developing and using a synthetic bone model was two-fold. One reason was to eliminate the need of procuring biological specimens, which can require significant time, effort, and expense. Experimentally, the elimination of biological variation between specimens could potentially provide data, which has much less variance between specimens. For this to occur however, a very reliable, efficient, and consistent method of preparing the bone-implant constructs had to be developed. With this in mind several fixtures were specially designed which were responsible for everything from preparing the bone for implantation to mounting the construct in the loading fixture. Theoretically, the goal was to eliminate the degree of human variation while preparing specimens for mechanical testing.

The foam plugs, which were meant to simulate cancellous bone at the tibial metaphysis, were created using a custom designed lathe tool. Consistency and efficiency were the focal points in the design of the lathe tool. Figure 2-30 shows the consistent final product prior to implantation into the bone model.

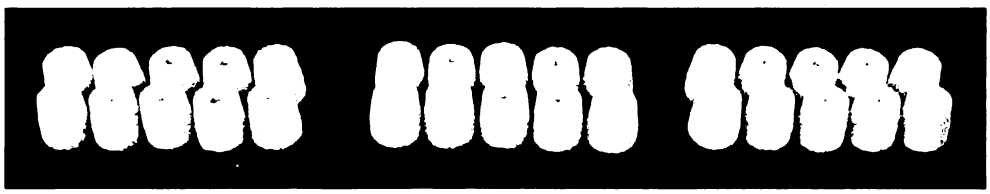

Figure 2-30. Polyurethane foam plugs created on a lathe with a custom designed tool.

The use of a drilling and alignment fixture was deemed successful based on the final bone-implant construct consistency in both the ILNb and ILN-ESF groups. Figure 2-31

shows the achievement of extremely consistent construct overall length (drilling fixture) and orientation of the nail within the bone model (alignment fixture).

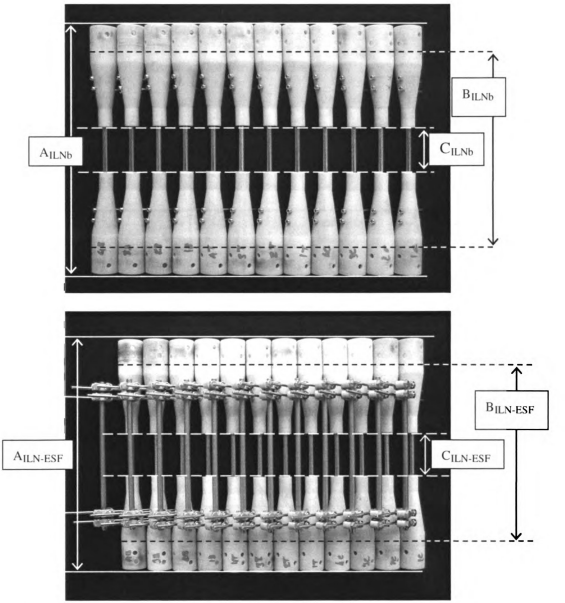

Figure 2-31. Fully assembled ILNb (top) and ILN-ESF (bottom) constructs, where:

A = overall construct length
$A_{ILNb} = 270$ mm = $A_{ILN-ESF}$
B = testing length (length between loading cups)
$B_{ILNb} = 210$ mm = $B_{ILN-ESF}$
C = osteotomy length (fracture gap)
$C_{ILNb} = 50$ mm = $C_{ILN-ESF}$

Torsion Tests

Construct Compliance – Construct compliance curves for both the ILNb and ILN-ESF were consistently bimodal in torsion (Figure 2-32).

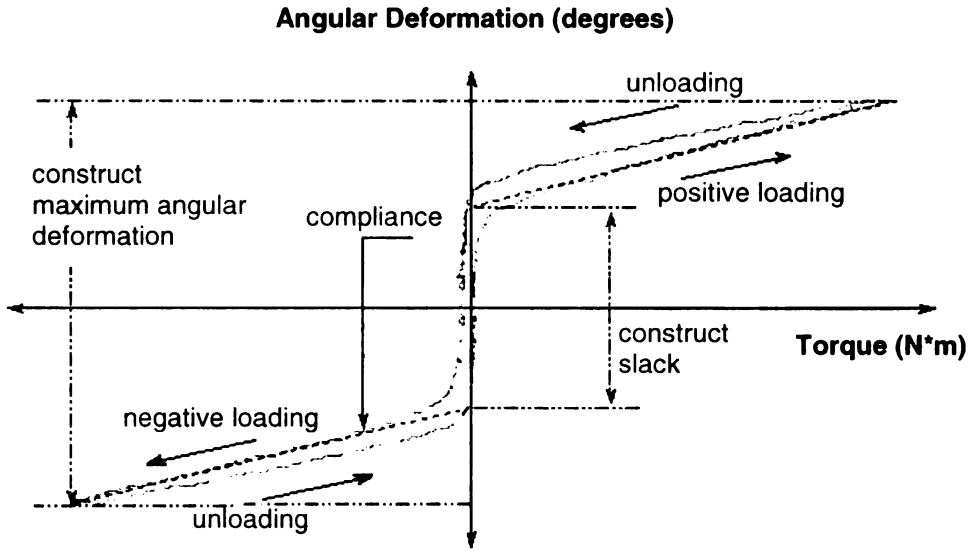

Figure 2-32. Typical bimodal torsion compliance curve.

The graphs of the ILNb (Figure 2-33) indicated no quantifiable torque in the central region, corresponding to the change in the direction of applied torque.

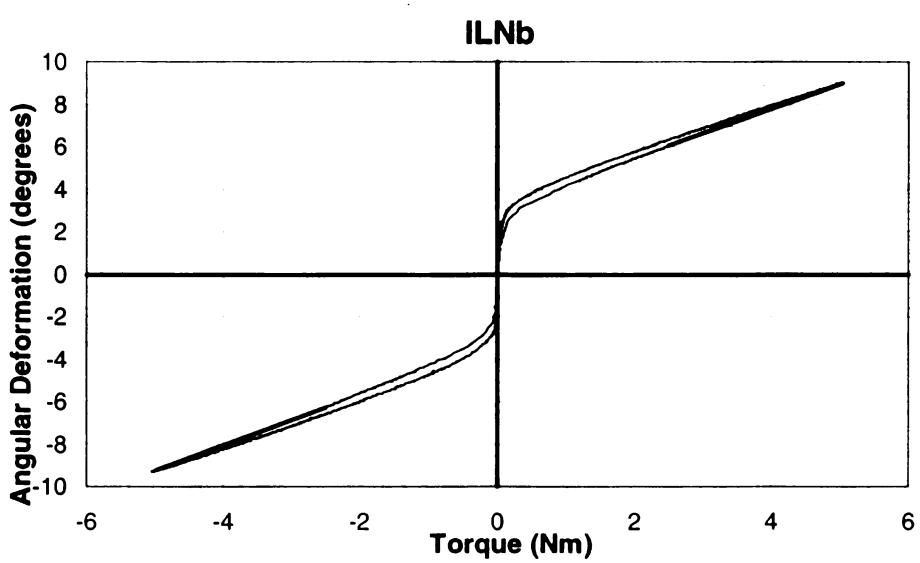

Figure 2-33. Representative torsion curve for ILNb, notice the presence of slack.

This central region (torque = 0) represented the slack in the construct and reflected an abrupt change in angular deformation without resistance to applied torque. The bimodal appearance of the ILN-ESF curves was different (Figure 2-34).

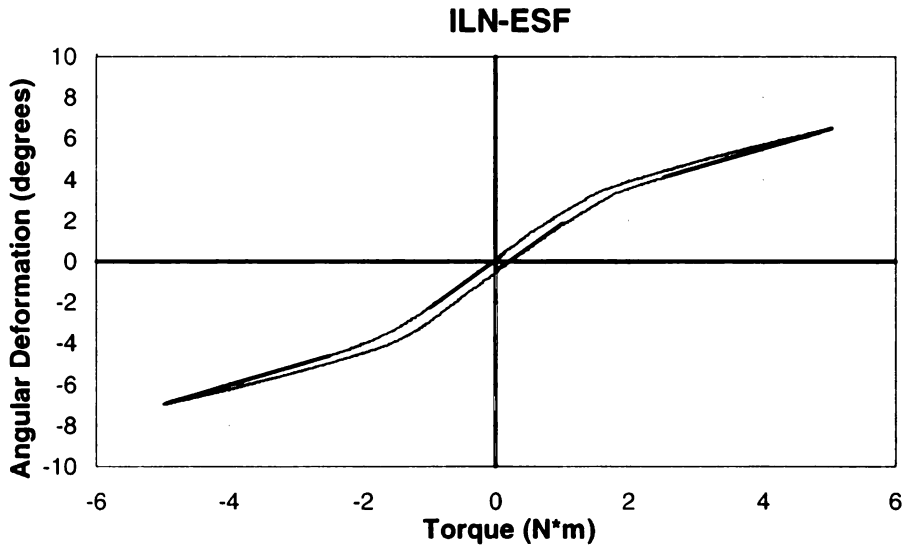

Figure 2-34. Representative torsion curve for ILN-ESF, notice the lack of slack and change in compliance.

With ILN-ESF, there was no characteristic vertical region of the curve where the direction of torque was changed, thus indicating that no slack was present. There was, however, a visible and quantifiable change in the compliance of the construct throughout its cycle (Figure 2-34). Therefore, both initial (IC) and terminal (TC) compliances were computed for the ILN-ESF constructs. The initial (ILN-ESF construct only) and terminal (ILN-ESF and ILNb constructs) compliances were calculated as the slope of the deformation versus torque curve from 0-1 Nm and 2.5-5 Nm, respectively. Compliance was calculated as the mean of the positive and negative loading curves because there was

not a significant difference between the positive and negative compliances in either group for either test ($p > 0.05$).

There was a significant difference in the initial (1.88 ± 0.29 °/Nm) and terminal (0.87 ± 0.1 °/Nm) compliances for the ILN-ESF constructs ($p < 0.05$ [Table 2-2]). Terminal compliance of the ILN-ESF constructs was significantly less than that for the ILNb constructs ($p < 0.05$). Terminal compliance of the ILN-ESF construct was approximately 25% less compliant than that of the ILNb constructs (0.87 ± 0.1 °/Nm and 1.16 ± 0.01 °/Nm, respectively).

Construct Angular Deformation – Maximum angular deformation for the ILN-ESF constructs was approximately 30% less than that for the ILNb constructs (12.2 ± 0.87° and 17.74 ± 0.45°, respectively). Construct slack, where present, was computed as the difference between the y-axis intercept of the compliance slope on the positive and negative loading curves (Figure 2-32). ILNb constructs exhibited 6.12 ± 0.5° of slack. While the ILN-ESF had no region of slack, there was both an initial and terminal compliance in the constructs (Figure 2-34). At high torques, ILN-ESF constructs deformed approximately 5% more than the ILNb constructs (12.2 ± 0.87° and 11.62 ± 0.06°, respectively), once the slack was overcome at high torques. These differences were not statistically significant ($p=0.234$)

Construct	IC (°/Nm)	TC (°/Nm) #	Slack (°)	Angular Def. (°) #	Def. – Slack (°)
ILNb	NA	1.16 ± 0.01	6.12 ±0.5	17.74 ± 0.45	11.62±0.06
ILN-ESF	1.88±0.29*	0.87±0.1*	none	12.2 ± 0.87	12.2 ± 0.87

Table 2-2. Torsion data (mean ± standard deviation), indicating significant differences ($p<0.05$)
between ILNb and ILN-ESF constructs
* within ILN-ESF group
(see Appendix 4 for exact p-values)

Bending Tests

Construct Compliance – Construct compliance curves for the ILNb were also consistently bimodal in bending (Figure 2-35), whereas ILN-ESF curves were unimodal. The bimodal graphs of the ILNb indicate that there was no quantifiable moment in the central region, which corresponded to the change in the direction of the applied bending moment. For all practical purposes this region represented slack in the construct and reflected an abrupt change in angular deformation without resistance to the applied bending moment. Conversely, with unimodal shape of the ILN-ESF compliance curves (Figure 2-36), there was no measurable region of slack for these specimens. Construct compliances were calculated as the slope of the deformation versus moment curve from 1.5-3.5 Nm. Compliance in the ILN-ESF constructs was significantly less than that for the ILNb constructs ($p < 0.05$ [Table 2-3]). Specifically, the ILN-ESF construct was approximately 60% less compliant than the ILNb constructs (0.29 ± 0.01 °/Nm and 0.7 ± 0.05 °/Nm, respectively).

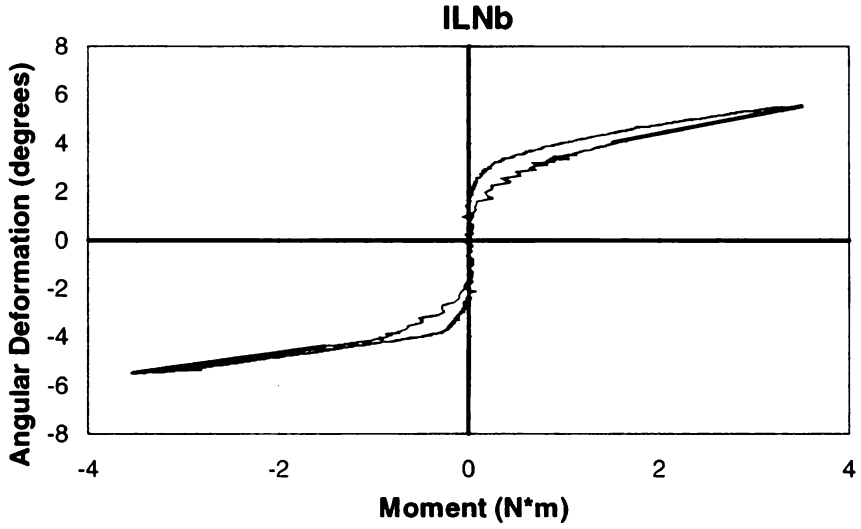

Figure 2-35. Representative mediolateral bending curve for ILNb, notice the bimodal shape and presence of slack.

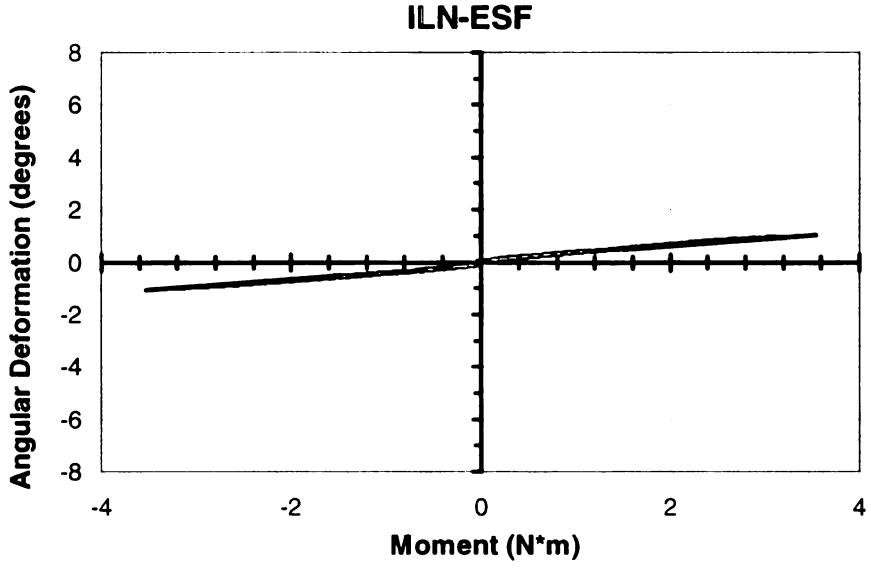

Figure 2-36. Representative mediolateral bending curve for ILN-ESF, notice the unimodal shape due to an absence of slack.

Construct Angular Deformation – Maximum angular deformation developed in the ILN-ESF constructs was approximately 80% less than that in the ILNb constructs (2.09 ± 0.004 ° and 11.38 ± 0.45 °, respectively). ILNb constructs exhibited slack (6.51 ± 0.05 °)

(Figure 2-35), whereas the ILN-ESF had a relatively constant resistance to load throughout their bending cycle (Figure 2-36). Angular deformation for the ILNb constructs, once slack was overcome (at high torques), was approximately 60% greater than that of the ILN-ESF constructs (4.88 ± 0.44 ^{o} and 2.09 ± 0.01 ^{o}, respectively).

Construct	Compliance (°/Nm) #	Slack (°)	Angular Deformation (°) #	Deformation – Slack (°)#
ILNb	0.7 ± 0.05	6.51 ± 0.05	11.38 ± 0.45	4.88 ± 0.44
ILN-ESF	0.29 ± 0.01	none	2.09 ± 0.004	2.09 ± 0.01

Table 2-3. Bending data (mean ± standard deviation), indicating significant differences ($p < 0.05$):

between ILNb and ILN-ESF constructs.

Compression Tests

Construct Compliance and Displacement – Construct compliances were computed as the slope of the displacement versus load curves from 50-176 N (Figure 2-37). Compliance of the ILN-ESF construct was significantly less than that of ILNb constructs ($p < 0.001$). ILN-ESF constructs were approximately 45% less compliant (5.35 ± 0.89 mm/N*E-04 and 9.78 ± 0.86 mm/N*E-04, respectively) than ILNb constructs and displaced approximately 40% less than ILNb constructs (9.28 ± 1.8E mm*E-02 and 16 ± 0.7 mm*E-02, respectively [Table 2-4]).

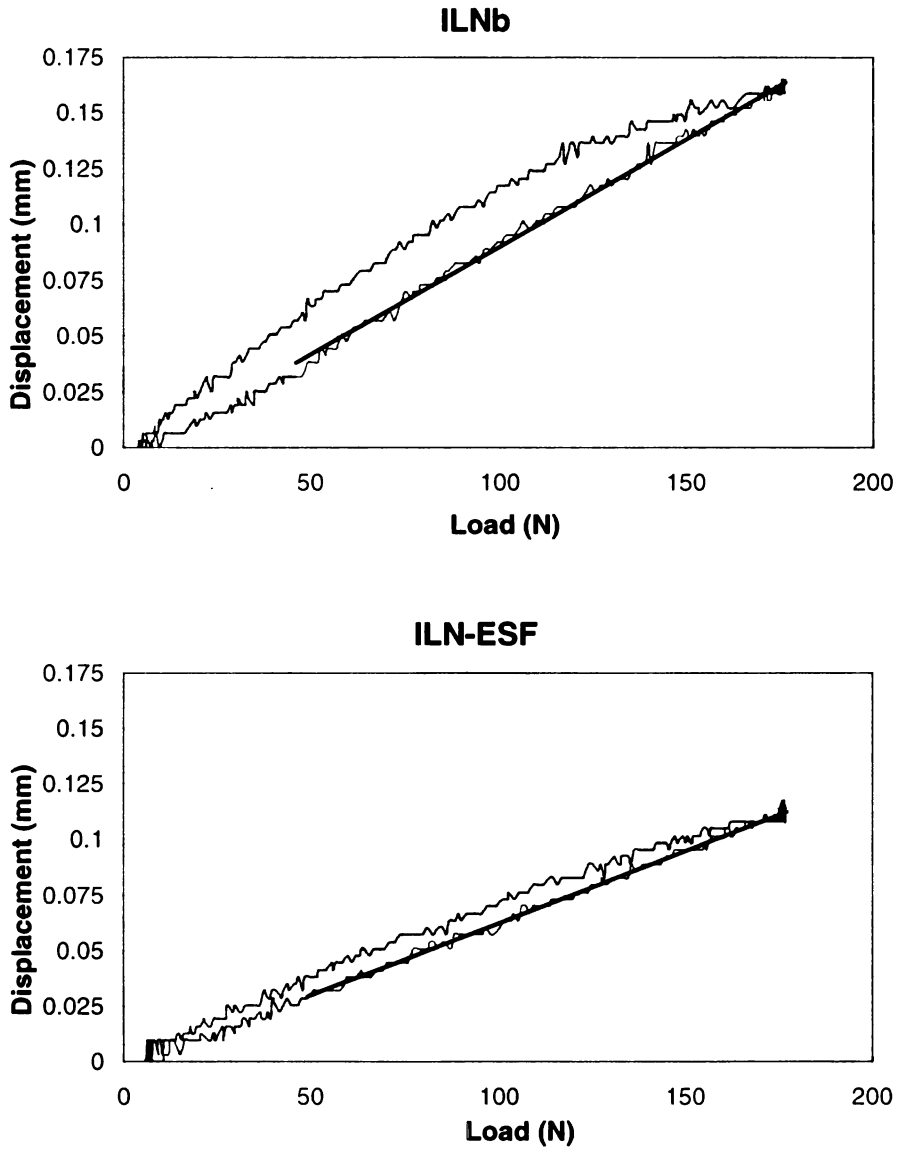

Figure 2-37. Representative compression curves for ILNb (top) and ILN-ESF (bottom).

Construct	Compliance (mm/N*E-04) #	Displacement (mm*E-02) #
ILNb	9.78 ± 0.86	16 ± 0.7
ILN-ESF	5.35 ± 0.89	9.28 ± 1.8

Table 2-4. Compression data (mean ± standard deviation), indicating significant differences ($p < 0.05$):

between ILNb and ILN-ESF constructs.

DISCUSSION

The hypothesis of the present study was that the ILN-ESF construct would be less compliant than the ILNb in torsion, bending, and compression. The results of the torsion tests in the current study indicate that there was a significant variation in compliance of the ILN-ESF construct as it was loaded. The initial and terminal compliances of the construct were 1.88 ± 0.29 °/Nm and 0.87±0.1 °/Nm, respectively. Furthermore, the terminal compliance of the ILN-ESF constructs were 25% less compliant than the ILNb constructs (0.87 and 1.16 °/Nm, respectively) and deformed approximately 30% less. The results of the bending tests indicated that the ILN-ESF constructs were approximately 60% less compliant than ILNb constructs (0.29 ± 0.01 °/Nm and 0.7 ± 0.05 °/Nm, respectively) and underwent approximately 80% less deformation (7.97 ± 0.05° and 9.45 ± 0.22°, respectively). Finally, as seen with torsion and bending, the compression tests showed similar trends, specifically, the ILN-ESF constructs were approximately 45% less compliant than the ILNb constructs (5.35 ± 0.89 and 9.78 ± 0.86 mm/N*E-04, respectively. The substitution of standard ILN locking bolts with an ESF in the current study significantly reduced the construct compliance and overall deformation in torsion, bending and compression, thus creating a more stable construct. This added stability could create the biomechanical environment necessary for improved fracture healing, by eliminating excessive interfragmentary motion.

Although the exact level of fracture stability necessary to optimize bone healing has yet to be determined, numerous studies have suggested that, while controlled axial micromotion promotes bone healing, excessive interfragmentary shear motion often results in delayed ossification of the fracture site.[21,32-36] In my study, the substitution of

locking bolts with extended bolts connected with a type IA ESF significantly reduced construct compliance and overall deformation in torsion, bending and axial compression to create a more stable construct. Perhaps more importantly, the use of an ILN-ESF appeared to have successfully eliminated construct slack. By eliminating excessive and uncontrolled interfragmentary motion, the added stability provided by ILN-ESF could create a biomechanical environment more favorable for fracture healing.

Because tibial fractures in people are inherently unstable in torsion and mediolateral bending,[37-40] the fixation method should efficiently counteract torsional and bending stresses to which these fractures are subjected post-operatively. However, both *in vitro* and *in vivo* experimental studies have documented torsional and bending instability with various human ILN designs.[11,12,15] The recent comparison of a human ILN to an ESF in an ovine tibial fracture model showed significantly more interfragmentary motion with inferior bone healing and incomplete return to function in the ILN treated sheep compared to the ESF group.[11] In an effort to improve fracture repair stability, experimental angle-stable nails have been recently designed in human and veterinary orthopaedics.[41,42] Both systems showed that through re-engineering of the locking system, construct stability is greater than that offered by conventional nails, which in turn results superior bone healing and more complete functional recovery.[42] One can speculate that because of the comparable muscle distribution between humans and dogs, tibial fractures in dogs may undergo similar deformation patterns if ineffectively stabilized. Ironically, the limited ability of current veterinary nails to counteract torsion and bending parallels that of human nails. Indeed, torsional slack was first reported in an *in vitro* evaluation of screwed interlocking nails using a canine tibial fracture model.[16]

Concurrently, intra- and post-operative instability have been documented in 12-14% of fracture cases treated with standard veterinary ILNs.[9,18,19] To provide adequate stability and reduce the risk of delayed or non-union, various supplementations of current veterinary ILN systems with other modes of fixation have been devised.[17-19,24] The development of an ILN coupled to a type IA ESF represents one of the recent techniques used to more effectively stabilize diaphyseal fractures in dogs.[18,19,24]

While the angular deformation of both constructs in response to applied torques was biphasic, the torsional compliance of the bolted nail constructs at low torques was not measurable. A similar behavior has been documented in screwed ILNs and was attributed to construct slack inherent to the design of current ILN systems.[16] In contrast, the initial compliance of the ILN-ESF constructs at low torque levels was quantifiable. This anticipated behavior was attributed to the resistance of the external fixator frame alone, mainly through early and continuous flexural deformation of the extended locking bolts. From a mechanical point of view, the external fixator serves as a pathway for accepting the torsional loads applied to the bone through bending of the transosseous pins. A torsional force on the bone model is like a load applied perpendicular to the longitudinal axis of the pin. This load results in bending of the transosseous pin, comparable to a cantilever beam in bending (Figure 2- 38).

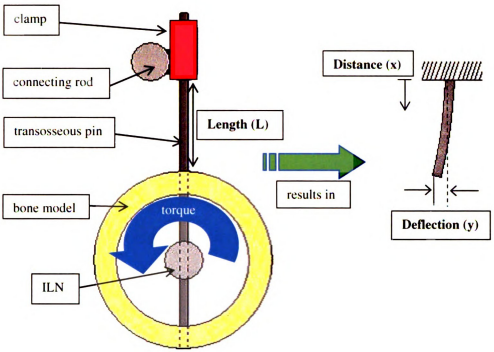

Figure 2- 38. Schematic of the load transfer between the bone and ESF. In vitro setup is shown on the left and beam theory correlation is shown on the right.

In beam theory, the stiffness of a cantilever beam can be calculated with:

$$k = \frac{P}{y} = \frac{3EI}{L^3} \qquad [2\text{-}2]$$

Equation 2-2. ESF stiffness (k) equation, where:

P = applied load
L = length
E = elastic modulus
I = area moment of inertia
y = deflection

Huiskes et al., developed a more complete model of ESF stiffness, taking mechanical properties of the connecting rod as well as the pin configuration into account. That model was also based on cantilever beam theory and gave results that were in good agreement with both experimental and finite element analysis.[43] However, the Huiskes model was

based on axial compression tests, without the connection of an ESF to an ILN, therefore it could not be directly applied to the current study.

The initial compliance of the ILN-ESF constructs was directly influenced by the working length of the extended locking bolts, i.e. the length between the connecting bar and the outer edge of the bone model.[23,30] A previous study showed that the stiffness (the inverse of compliance) of an ESF construct in torsion significantly increases when the distance between the connecting bar of the ESF and the bone is decreased from 1.5 cm to 0.5 cm.[30] Therefore, to reduce inter-specimen variability, the distance between the ILN and the connecting bar was standardized in this study. As the deformation of the ILN-ESF constructs increased in response to increased torque levels, the extended locking bolts began to engage the nail. The added contribution of the nail in resisting construct deformation resulted in a significant decrease in the ILN-ESF construct compliance at high torque levels and accordingly, the terminal compliance of the ILN-ESF constructs was significantly smaller than that of the ILNb constructs.

The slack in the ILNb construct was due to a mismatch between bolt and nail hole diameter. This mismatch allowed the nail to move a considerable amount prior to engagement with the bolt (Figure 2-39).

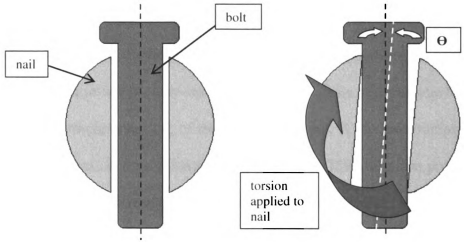

Figure 2-39. Schematic of the nail without applied torque (left) and after torques is applied (right). The nail hole axis is white and the bolt axis is black, notice the amount of nail rotation (Θ) prior to engagement between the bolt and nail.

The significantly smaller torsional deformation of the ILN-ESF constructs was mainly due to the elimination of construct slack. Indeed, once the slack inherent to the bolted nail system was overcome, both ILN-ESF and ILNb constructs underwent similar overall deformation ($12.2 \pm 0.87°$ and $11.6 \pm 0.5°$, respectively). Interestingly, a previous study[16] showed that the torsional deformation of tibial constructs stabilized with a plate-rod-combination was similar in magnitude ($11.66 \pm 2.59°$) to that of ILN-ESF constructs. This suggested that this hybrid system should be effective in counteracting fracture forces in clinical cases. While the current study suggested that the use of bolts instead of screws, as used in the previous study,[16] substantially reduced the amount of slack, it also demonstrated that construct slack can be eliminated by using extended bolts connected to an ESF frame. Similar observations have been reported in a clinical study where intra-operative torsional slack associated with the use of an ILNb was eliminated with the addition of a type IA ESF.[18]

In bending tests, the differences seen in the angular deformations can again be attributed to slack in the ILNb constructs (6.51 ± 0.05°). However, the differences in compliance were most likely due to the external fixator acting as a pathway for accepting the applied loads through bending of the transosseous pin. While the addition of an ESF reduced construct torsional compliance by approximately 25%, the same procedure had a more dramatic effect in bending where the use of an ESF resulted in a 60% decrease in construct compliance. As in torsion, this bending deformation resulted in the transosseous pins being subjected to loading perpendicular to their longitudinal axes (Figure 2- 40).

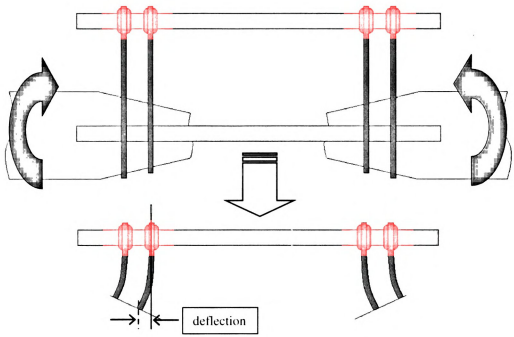

Figure 2-40. Schematic of the applied moment on the bone model resulting in deflection of the transosseous pins.

Furthermore, the bending compliance curves of the ILN-ESF constructs were consistently unimodal. This indicates that ILN-ESF constructs resisted applied bending moments in a continuous manner similar to that of bone plates.[16] The effectiveness of the

ESF in mediolateral bending was also reflected by the small angular deformation, as well as by the absence of slack compared to the bolted nails.

Compression showed that the ILNb and ILN-ESF constructs both had small deformations (approximately 0.16 and 0.09 mm, respectively). Several *in vivo* studies have shown that controlled axial micromotion may enhance bone healing,[21,32-36] therefore with this amount of deformation (less than 2 mm), the use of either construct could be advantageous for healing of fractures from an axial micromotion perspective.

Because standard and extended bolts have identical diameters, it was speculated that extended bolts alone would not be capable of providing construct stability. To test this theory (see Appendix 4 for data), the connecting bar was removed from the ILN-ESF specimens following torsion and bending tests and retested in torsion. As expected, the compliance, angular deformation and slack of the ILN constructs with extended bolts alone were identical to those of the ILNb constructs. Therefore, one must recognize that the integrity of the connecting clamps, and not the extended bolts, is essential to prevent torsional and bending slack in ILN-ESF constructs. Should the ESF connecting bar become lose, the stability of the repair would be compromised.

A limitation of this study was the use of a synthetic bone model as a substitute for cadaveric tissue. However, the bone model greatly limited specimen variability and thereby allowed for better evaluation of the implant itself. The shape and material properties of bones used in a human cadaveric study [44] have standard deviations (SDs) that exceeded 100%. These SDs are likely to be even greater in dogs on the basis of the large number of breeds and conformations. Therefore the canine tibia model was created to limit interspecimen variability and thereby allow for a better evaluation of the implant.

Simple tubes of various materials have been used for fatigue testing;[37,45] however, complex shapes may be more appropriate to model physiological loads when devices for fracture fixation are evaluated.[46] In an attempt to create a more realistic tibial model, tapered ends created on the basis of measurements obtained by MSU SACS were incorporated into the model to mimic the larger metaphysis. In another experimental study [45] that used a bone model, ILNs were more susceptible to failure when implanted in the center of larger aluminum bone models. Accordingly, to subject the ILN-ESF to the most stringent conditions and allow meaningful comparison between groups, all nails were locked near the ends of the model (outside diameter, 26 and 23 mm) and were maintained in a central location by use of a polyurethane plug.

In nonfailure tests, mechanical properties that directly affect any alteration of the screw-bone interface during loading have not been determined. Therefore, general mechanical properties of human and canine cortical bone were used as guidelines for choosing an acceptable material. Although models of human tibiae are commercially available (Sawbones, Pacific Research Laboratories Inc., Vashon, WA), they are too large to represent tibiae of giant breeds (405 to 375 mm in length), and were cost prohibitive. The 30% glass-filled structural nylon composite chosen for use in the study reported here was commercially available and relatively inexpensive.

The development of the bone model required the development of numerous dedicated fixtures, which could allow the implants to be effectively and consistently implanted within the bone model. These fixtures produced constructs lacking the variability that could be introduced with implantation, such as implant positioning and overall length differences between constructs. In addition, the results of the study also

illustrated the effectiveness of not only the bone model itself, but also the fixtures that enabled its use. In a previous study,[16] angular deformations under torsion had standard deviations as high as 22% of the mean; standard deviations in the current study of similar tests were 7% of the mean. Minimum standard deviations in the current study were as low as 0.2% of the mean (ILN-ESF angular deformation in bending), compared to minimum deviations of 7% of the mean (ILN constructs locked with screws) in similar studies.[16] The reduction in standard deviations compared to the previous study was mainly attributable to the development of dedicated fixtures, which enabled the bone model to be implanted with the ILNs and ILN-ESFs consistently. This was based on the fact that both studies were conducted in the same laboratory (Orthopaedic Biomechanics Lab) with the same equipment (Instron), and almost identical loading fixtures. Thus, the current study with this newly developed bone model yielded numerous advantages over natural specimens for the functional evaluation of construct designs.

CONCLUSION

The addition of an ESF to currently available ILN systems was meant to eliminate the instabilities associated with each system when used individually, while retaining their own unique biological and mechanical advantages. This technique was successfully used and documented in a limited number of clinical cases in small animal surgery.[19,24] One such study showed encouraging clinical use of the investigational hybrid ILN-ESF construct in dogs.[19]

The results of the current study suggested that an ILN locked with hybrid bolt-pins coupled with an ESF, compared with an ILN locked with standard bolts, significantly reduced construct compliance and overall deformation in torsion, bending, and compression. Furthermore, the inherent slack of the bolted ILN was eliminated by the supplementation of an ESF in torsion and bending. The improvement in construct stability documented in the ILN-ESF constructs could diminish interfragmentary motion at the fracture site and potentially improve bone healing. Accordingly, ILN-ESF may represent an effective alternative to standard ILN fixation, particularly in the treatment of diaphyseal tibial fractures.

REFERENCES

1. Field JR, Tornkvist H. Biological fracture fixation: a perspective. Vet Comp Orthop Traumatol 14: 169-178, 2001

2. Aron DN, Palmer RH, Johnson AL. Biologic strategies and a balanced concept of repair of highly comminuted long bone fractures. Comp Cont Ed Pract Vet 17: 35-38, 1995

3. Bernarde A, Diop A, Maurel N, et al. An in vitro biomechanical study of bone plate and interlocking nail in a canine diaphyseal femoral fracture model. Vet Surg 30: 397-408, 2001

4. Roe SC. Mechanical characteristics and comparisons of cerclage wires. Introduction of the double-wrap and loop/twist tying methods. Vet Surg. 1997 Jul-Aug; 26 (4): 310-6

5. Piermattei DL, Flo GL. Fractures: classification, diagnosis, and treatment, in Handbook of Small Animal Orthopedics and Fracture Repair (ed 3rd). Philadelphia, W. B. Saunders, 1997, pp 24-146

6. Moses PA, Lewis DD, Lanz OI, et al. Intra-medullary interlocking nail stabilization of 21 humeral fractures in 19 dogs and one cat. Aust Vet J 80: 336-343, 2002

7. Durall I, Diaz-Bertrana MC, Morales I. Interlocking nail stabilization of humeral fractures: initial experiences in seven clinical cases. Vet Comp Orthop Traumatol 7: 3-8, 1994

8. Dueland RT, Johnson KA, Roe SC, et al. Interlocking nail treatment of diaphyseal long bone fractures in dogs. J Am Vet Med Assoc 214: 59-66, 1999

9. Duhautois B. Use of Veterinary Interlocking Nails for Diaphyseal Fractures in Dogs and Cats: 121 Cases. Vet Surg 32: 8-20, 2003

10. Klemm KW, Borner M. Interlocking nailing of complex fractures of the femur and tibia. Clin Orthop Relat Res. 1986 Nov; (212): 89-100

11. Klein P, Opitz M, Schell H, et al. Comparison of unreamed nailing and external fixation of tibia diastases-mechanical conditions during healing and biological outcome. J Orthop Res 22: 1072-1078, 2004

12. Laflamme GY, Heimlich D, Stephen D, et al. Proximal tibial stability with intramedullary nail fixation using oblique interlocking screws. J Orthop Trauma 17: 496-502, 2003

13. Knothe U, Knothe TML, Klaue K, et al. Development and testing of a new self-locking intramedullary nail system: testing of handling aspects and mechanical properties. Injury 31: 617-626, 2000

14. Lin J, Lin SJ, Chen PQ, et al. Stress analysis of the distal lockinig screws for femoral interlocking nailing. J Orthop Res 19: 57-63, 2001

15. Schandelmaier P, Krettek C, Tscherne H. Biomechanical study of nine different tibia-locking nails. J Orthop Trauma 10: 37-44, 1996

16. Von Pfeil DJF, Déjardin LM, DeCamp CE, et al. In vitro biomechanical comparison of plate-rod combination-construct and an interlocking nail-constructs for experimentally induced gap fractures in canine tibiae. Am J Vet Res 66:1536-1543, 2005

17. Suber JT, May BM, Basinger RR. A comparison of bending and gap stiffness between interlocking nails and interlocking nails supplemented with stack pins. Vet Comp Orthop Traumatol, In press

18. Basinger RR, Suber JT. Two techniques for supplementing interlocking nail repair of fractures of the humerus, femur, and tibia: results in 12 dogs and cats. Vet Surg 33: 673-680, 2004

19. Basinger RR, Suber JT. Supplemental fixation of fractures repaired with interlocking nail: 14 cases. In: Proceedings, 29th An Meet Vet Orthop Soc, The Canyons, UT: 27 2002

20. Marcellin-Little DJ. External skeletal fixation, in Slatter D (ed): Textbook of Small Animal Surgery (ed 2). Philadelphia, Saunders, 2003, pp 1818-1834

21. Goodship AE, Watkins PE, Rigby HS, et al. The role of fixator frame stiffness in the control of fracture healing. An experimental study. J Biomech 26: 1027-1035, 1993

22. Claes LE. Biomechanics of fracture repair and fracture fixation. In: Mow VC, Hayes WC, eds. Basic Orthopaedic Biomechanics and Mechano-Biology. Philadelphia: Lippincott Williams and Wilkins; 2005

23. Johnson WD, Fischer DA. Skeletal stabilization with a multiplane external fixation device. Biomechanical evaluation and finite element model. Clin Orthop Rel Res 180: 34-43, 1983

24. Nanai B, Basinger RR. Use of a new investigational interlocking nail supplement in the repair of comminuted diaphyseal tibia fractures in two dogs. J Am Anim Hosp Assoc 41: 203-208, 2005

25. Yamada H. Mechanical properties of locomotor organs and tissues. In: Evans FG, ed. Strength of biological materials. Baltimore: The Williams & Wilkins Co, 1970; 20, 54

26. Reilly DT, Burstein AH. The elastic and ultimate properties of compact bone tissue. J Biomech 1975; 8: 393–405

27. Carter DR, Spengler DM. Mechanical properties and composition of cortical bone. Clin Orthop Relat Res 1978; 135: 192–217

28. Silbernagel JT, Kennedy SC, Johnson AL, et al. Validation of canine cancellous and cortical polyurethane foam bone models. Vet Comp Orthop Traumatol 2002; 15: 200–204

29. Mat-Web. http://www.matweb.com/search/SpecificMaterial.asp?bassnum=PTSXBI21

30. Bouvy BM, Markel MD, Chelikani S, et al. Ex vivo biomechanics of Kirschner-Ehmer external skeletal fixation applied to canine tibiae. Vet Surg 22: 194-207, 1993

31. DeCamp CE, Soutas-Little RW, Hauptmann J, et al: Kinematic gait analysis of the trot in healthy greyhound dogs. Am J Vet Res 54:627–634, 1993

32. Claes LE, Eckert-Hubner K, Augat P. The effect of mechanical stability on local vascularization and tissue differentiation in callus healing. J Ortho Res 20: 1099-1105, 2002.

33. Claes LE, Heigele CA. Magnitudes of local stress and strain along bony surfaces predict the course and type of fracture healing. J Biomech 32: 255-266, 1999

34. Claes LE, Heigele CA, Neidlinger-Wilke C, et al. Effects of machanical factors on the fracture healing process. Clin Orthop Relat Res Suppl 355: S132-S147, 1998

35. Lewallen DG, Chao EY, Kasman RA, et al. Comparison of the effects of compression plates and external fixators on early bone-healing. J Bone Joint Surg Am 66: 1084-1091, 1984

36. Wu JJ, Shyr HS, Chao EY, et al. Comparison of osteotomy heling under external fixation devices with different stiffness characteristics. J Bone Joint Surg Am 66: 1258-1264, 1984

37. Gaebler C, Berger U, Schandelmaier E, et al. Rates and odds ratios for complications in closed and open tibial fractures treated with unreamed, small diameter tibial nails: a multicenter analysis of 467 cases. J Orthop Trauma 2001; 15: 415-423

38. Freedman EL, Johnson EE. Radiographic analysis of tibial fracture malalignment following intrmedullary nailing. Clin Orthop 315: 25-33, 1995

39. Mercado EM, Lim EV, Stern PJ, et al. Exchange nailing for failure of initially rodded tibial shaft fractures. Orthopedics 24: 757-762, 2001

40. Safran O, Liebergall M, Segal D et al. Proximal tibial fractures - should we nail them? Am J Orhtop 30: 681-684, 2001

41. Déjardin LM, Lansdowne JL, Sinnott MT, et al. In vitro mechanical evaluation of torsional loading in simulated canine tibiae for a novel hourglass-shaped interlocking nail with a self-tapping tapered locking design. Am J Vet Res 67:678-685, 2006.

42. Kaspar K, Schell H. Seebeck P et al. Angle stable locking reduces interfragmnetary movements and promotes healing after unreamed nailing. Study of a displaced osteotomy model in sheep tibiae. J Bone Joint Surg Am 87: 2028-2037, 2005

43. Huiskes R, Chao EYS. Guidelines for external fixation frame rigidity and stresses. J Orthop Res 4: 68-75, 1986

44. Hulse D, Hyman W, Nori M, et al. Reduction in plate strain by addition of an intramedullary pin. *Vet Surg* 1997;26: 451–459

45. Aper RL, Litsky AS, Roe SC, et al. Effect of bone diameter and eccentric loading on fatigue life of cortical screws used with interlocking nails. Am J Vet Res 2003; 64: 569–573

46. Szivek JA. Synthetic materials and structures used as models for bone. In: An YH, Drauhgn RA, eds. Mechanical testing of bone and the bone-implant interface. Boca Raton, Fla: CRC Press LLC, 2000; 159–171

CHAPTER THREE

COMPREHENSIVE MECHANICAL EVALUATION OF FRACTURE FIXATION SYSTEMS: COMPARISON OF PLATED VS. SCREWED, BOLTED AND NOVEL INTERLOCKING NAIL CONSTRUCTS

ABSTRACT

Interlocking nails (ILNs) are attractive alternatives to plate fixation for repair of comminuted fractures due to several mechanical and biological advantages. While the use of ILNs has yielded favorable clinical outcomes in both human and animal patients, several limitations have been documented clinically and experimentally. Specifically, current ILN systems do not counteract torsional and bending forces as much as initially anticipated, which could explain the complications reported clinically. In an attempt to reduce instability inherent to ILN constructs, a novel interlocking nail and locking mechanism were designed (ILNn) by our research group. The novel nail featured a tapered self-locking mechanism engineered to improve implant stability along with an hourglass profile, which tapered from 8-mm extremities to a 6-mm central core and was designed to preserve the biological advantages of ILN fixation. The purpose of this study was to use a previously described tibial fracture model to provide a comprehensive evaluation of the torsional and bending characteristics of currently available 6-and 8-mm screwed and bolted ILNs (ILN6s, ILN8s, ILN6b, ILN8b, respectively), and to compare the structural properties of these ILNs to those of an ILNn and a standard plate (br-DCP). The study hypotheses were that the compliance of ILNn constructs would be in between that of 6-mm and 8-mm ILN constructs and smaller than that of 3.5mm br-DCP constructs, that the angular deformation of screwed constructs would be greater than that of bolted constructs and that ILNn constructs would sustain the least deformation of all

constructs. Another hypothesis was that all standard ILN constructs would have slack, whereas the ILNn and br-DCP construct deformation would occur without slack.

Forty-eight bone models treated with 6-mm and 8-mm nails locked with screws or bolts (ILN6s, ILN8s, ILN6b, ILN8b, respectively), ILNn, and a 3.5-mm broad-DCP (br-DCP) (n=4/testing mode) were tested in torsion or 4-point bending. Construct compliance, deformation and slack were statistically compared.

Results of this study showed that regardless of testing mode, construct compliance was greater with smaller ILNs. Screwed constructs were more compliant than bolted ones, with a significant difference between ILN6s and ILN6b in torsion. Plated constructs were significantly more compliant than the ILNn. Angular deformation was consistently greater with smaller ILNs. Screwed ILN constructs sustained approximately twice the torsional deformation of bolted ones. Comparatively, ILNn constructs underwent significantly less torsional and bending deformation than other constructs. While standard ILN constructs had slack in both modes, ILNn and br-DCP construct deformations consistently occurred without slack. This study suggested that while using bolts rather than screws improved the ILNs mechanical behavior, neither locking mechanism effectively counteracted torsion and bending forces. Conversely, the ILNn angle-stable locking system eliminated torsional and bending slack resulting in comparable mechanical performances between ILNn and plated constructs. Considering the potentially deleterious effect of uncontrolled motion on bone healing, the ILNn may represent a biomechanically more effective fixation method than standard ILNs for the treatment of comminuted diaphyseal fractures, as well as a valid alternative to plate fixation.

INTRODUCTION

As a result of biological and mechanical advantages, interlocking nails (ILNs) are considered the standard of care for use in the treatment of most diaphyseal fractures of the humerus, femur, and tibia in people.[1] However, as the use of ILNs has increased clinical limitations have been reported which prompted several experimental studies.[2-8] One in vivo study,[2] revealed a significant delay in bone healing and functional recovery when results for an ILN were compared with those for an external fixator in experimentally induced tibial fractures using sheep. This delay in bone healing was attributed to torsional and bending instability. A similar in vitro study[9] revealed that torsional compliance and deformation of tibial constructs implanted with ILNs were greater than those of constructs implanted with a plate-rod construct (PRC). In that study ILN constructs under torsional loads had up to 28° of slack, whereas PRC constructs underwent continuous deformation throughout the testing period. Similarly, an in vitro study[7] of 9 ILNs implanted in human tibiae revealed that there was both torsional and bending slack in all constructs, regardless of nail design. These studies suggest that current human and veterinary ILNs do not provide torsional and bending stability as much as initially anticipated, thus potentially contributing to complications, such as delayed healing or nonunion of fractures.[3,10]

Contrary to ILNs used in humans, which often are implanted after the medullary cavity is reamed, ILNs are used in veterinary medicine without reaming of the medullary cavity. Reaming allows for implantation of larger, stronger nails and increases contact between the nails and endocortices, thereby potentially improving stability of the repair.[10] However, reaming severely impairs the medullary blood supply and has been associated

with a higher incidence of infection and fat emboli.[2,12,13] The use of thinner ILNs, without reaming of the medullary cavity, has potential biological advantages, such as preservation of the endosteal and medullary blood.[2,7,13,14] The procedure however, places the construct at a mechanical disadvantage by reducing the nail-bone contact area[11] and increasing the working length of the locking device. This suggests that while reaming may be preferable from a biological standpoint, they risk the integrity of the locking mechanism from a mechanical standpoint.[15]

Current ILN designs require a mismatch between the screw/bolt and the nail hole diameters. While this mismatch permits the insertion of the locking device, it also allows some movement between the nail and the screw or bolt prior to rigid interaction between these two components of the ILN. Indeed, it has been reported[9] that *in vitro* torsional and bending instability results from the discrepancy between the screw or bolt diameters and that of the nail hole (See Chapter 2). Though not quantitatively reported, the same occurrence is likely responsible for the "play" described in similar *in vivo* studies.[3,7,8,10] Furthermore, it has been suggested[9] that this discrepancy may be exacerbated by flattening of the screw threads and by structural damages to the edges of the nail holes induced by the screw.

To increase stability, ILN constructs have been augmented with various implants.[10] Although improved stability has been subjectively reported[10] for use of such techniques, these augmentations are potentially time consuming and invasive, thereby offsetting the biological advantages of interlocking nails. In addition to providing adequate stability, implants must be sufficiently strong to withstand loads during the early postoperative period, particularly when cortical continuity is not achieved or local

instability may result in a prolonged healing time.[2] The second moment of area, or area moment of inertia (AMI) of an implant characterizes its ability to resist bending and is inversely proportional to the stress of a section under bending.[16] Because a larger AMI results in smaller stress values for a specific load, AMIs have been used to determine the theoretical fatigue life of implants[17,18] and predict the risk of stress fractures.[19] The AMIs for several implants, including broad dynamic compression plates (br-DCPs) and ILNs currently used in veterinary medicine have been reported and used as a basis for comparison of theoretical bending stiffness.[17,18]

To circumvent the mechanical shortcomings of current nail designs while preserving the biological benefits from use of smaller nails without reaming of the medullary cavity, a novel nail and locking system was developed (Loic M. Déjardin, US patent application No. 11/243,725, Office of Intellectual Property, Michigan State University). The nail and locking system (ILNn) were created to address several issues. Firstly, the ILNn was meant to substantially reduce relative motion between the locking device and nail, thereby effectively locking the construct. Another goal was to increase the nail-bone contact area in the metaphyseal region while limiting contact between the nail and endocortices throughout the medullary cavity of the diaphysis. And finally, the ILNn was designed to provide bending strength similar to that of existing ILNs, based on AMI. It was proposed that this design would substantially reduce torsional and bending instabilities, compared with traditional ILNs of similar size.

The purpose of the current study was then to mechanically compare this novel hourglass-shaped ILN and locking system to currently available ILN, br-DCP, and ILNn constructs in torsion and 4-point bending using a canine tibial gap fracture model

featuring the previously described synthetic bone substitute (Chapter 2). It was hypothesized that the bending and torsional compliances of novel ILN constructs would be significantly less than those of the currently available 6 mm ILN constructs, and that bending and torsional angular deformation of the novel ILN constructs would be less than currently available 6 and 8 mm ILN constructs. Because the new nail and locking system design was meant to eliminate slack, it was also hypothesized that angular deformation of the novel ILN and br-DCP constructs would be continuous throughout loading, whereas there would be slack during angular deformation of currently available ILN constructs. The slack present in currently available ILN constructs is due to a mismatch in screw and nail hole diameters.

MATERIALS AND METHODS

Specimen Preparation

Bone Model – In an attempt to limit specimen variability and circumvent the need to procure canine bones, a custom-made synthetic tibial model was used in this study. See Chapter 2 for a detailed description of this model.

Fixtures – Several fixtures were developed to provide consistent specimens and help reduce specimen variation. These fixtures guided specimen preparation from drilling pilot holes in the bone model to loading the specimens into the mechanical testing fixtures. See Chapter 2 for detailed information regarding these fixtures (drilling fixture, alignment fixture, foam lathing tool, potting fixture), and Chapter 1 for detailed information on the bending press (MSU BP), which was slightly modified to accommodate the br-DCPs. Accommodation of the MSU BP consisted of modifying the fulcrum and contact point to match the convex and concave aspects of the br-DCP.

In addition to the previously mentioned fixtures, an additional modification was made to the ILN-ESF alignment fixture mentioned in Chapter 2. Several additional pieces were designed to allow for consistent and accurate placement of the br-DCPs onto the bone model. Figure 3-1 shows the additional pieces of the ILN-ESF alignment fixture used to stabilize the pre-bent (with the MSU bending press) br-DCPs.

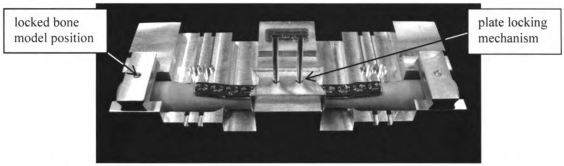

Figure 3-1. Modified ILN-ESF alignment fixture to accommodate the br-DCPs.

The function of the modified alignment fixture was to stabilize the plates so that pilot holes could be accurately drilled into the bone model for consistent plate placement. Movement in all directions had to be restricted to stabilize the plates. This was accomplished by a specially designed locking mechanism (Figure 3-2).

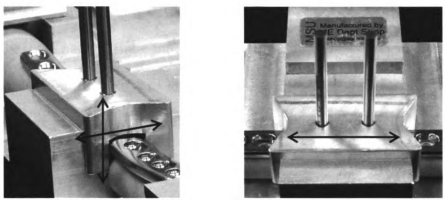

Figure 3-2. The plate locking mechanism that restricted movement in all directions.

The plate locking mechanism restricted front to back movement (shown in blue) of the plate by the shape of the cutout being the same size as the width of the plate. Left to right movement (shown in red) was restricted by two pins, which passed through holes in the plate and inserted into the base of the alignment fixture. Vertical movement (shown in green) of the plate was restricted by the bone model on the bottom and the cutout surface on the top.

Design of Novel ILN – Dogs affected with long bone fractures seen at Michigan State University Small Animal Clinic (MSU SMAC) commonly are midsize dogs weighing approx 30 to 35 kg. This patient population is often treated for comminuted fractures of the tibial diaphysis with a 6 mm or an 8 mm ILN (ILN6 and ILN8, respectively). Based on morphometric analyses of canine tibiae, a 185 mm long ILN is most often appropriate to fit the tibial diaphysis of dogs within that weight range. Therefore, prototypes of a novel ILN system were designed to be comparable to the commercially available 6 or 8 X 185-mm ILN (models 11-06-185-02-32.7 and 11-08-185-02-3.5, respectively, Innovative Animal Products, Rochester, MN).

Prototypes of the locking device and novel nail were designed with several primary constraints. The locking device had to provide rigid interaction with the nail. The shape of the nail had to limit interference with endocortices and facilitate fracture reduction, while limiting the risk of joint infraction attributable to perforation of the distal subchondral bone plate. Finally, the shape and size of the locking device had to enhance successful insertion during surgery.

Secondary constraints were the stiffness and strength of the locking device and nail. The AMI of the novel locking device had to be greater than that of a 4.5-mm bone screw and comparable to that of a commercially available 3.5-mm locking bolt. The AMI of the novel nail at the level of a locking hole had to be similar to that of an ILN8 with 3.5-mm bone screws in both the mediolateral and craniocaudal planes. Finally, the AMI of the weakest part of the solid central section of the novel nail had to be similar to that of the solid section of a 3.5-mm br-DCP.

To address the above constraints, an hourglass-shaped nail was designed. It featured an oblong bullet-like distal tip and a novel screw-cone-peg (SCP) locking device. The nail was fabricated with 316L stainless steel certified to ASTM F138 standards (Hourglass ILN/SCP, 20-TB08-TB-0A, BioMedtrix, Boonton, NJ [Figure 3-3]). This material was similar in chemical composition and mechanical properties to that used to manufacture the ILN8 used in the study (316L ASTM F139). Stainless-steel 316L ASTM F138 was chosen for the manufacture of the SCP locking device and the ILN components. This was largely because it is the material of choice for medical manufacturers of such implants. The outside diameter of the nail ends was 8 mm, whereas the central portion featured a reverse entasis that reduced the middle portion of the nail to an outside diameter of 6 mm. Two tapered holes (diameter, 4.0 and 3.2 mm, respectively) were placed 11 mm apart in each end of the nail. The most proximal and distal nail holes were separated by 155.5 mm. The SCP was designed as a self-tapping, cortical type screw (core diameter, 4 mm) with a central Morse taper that matched the nail hole and a solid distal tip (outside diameter, 3.2 mm). Prototype SCPs were manufactured in lengths of 26 and 30 mm.

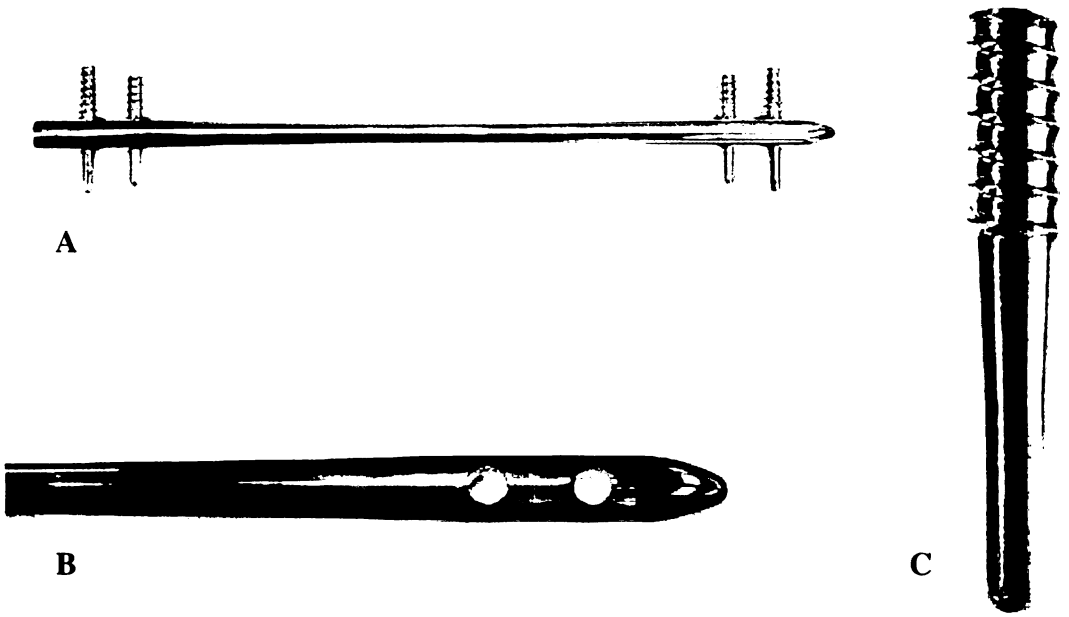

Figure 3-3. A) Photograph of ILNn. B) Close-up view of the distal end of the novel ILN. C) Close-up view of the SCP.

Measurement of AMI – AMIs were calculated using basic strength of materials theory, namely Equation 3-1, corresponding to Figure 3-4.

$$I_x = \int y^2 dA \qquad I_y = \int x^2 dA \qquad [3\text{-}1]$$

Equation 3-1. Area moment of inertia (AMI), where:

I_x: AMI with respect to x-axis (mediolateral AMI)

I_y: AMI with respect to y-axis (craniocaudal AMI)

y, x: equation of the line forming the boundary of the cross section

A: area of the cross section

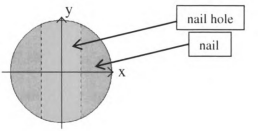

Figure 3-4. Cross-section of a nail with corresponding x and y-axes, shown at nail hole level.

AMI values were calculated for various sections of the SCP (screw, cone and peg) and the ILNs (nail hole level, and for the central section) (Figure 3-5).

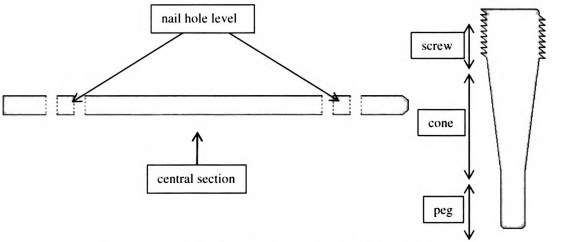

Figure 3-5. Schematic of various sections of SCP and ILN

AMIs were calculated with a specially designed computational program[20] which produced automated results based on inputs of ILN diameter (central section and nail hole) and screw size. See Appendix 3 for detailed Matlab programming.

Study Design

Implants were applied to the synthetic tibiae in 6 groups for a total of 8 specimens per group (n=4/testing mode; torsion, bending). Group 1 (ILN6s) was made up of 6 mm x 185 mm ILN with four 2.7 mm screws. Group 2 (ILN6b) was made up of 6 mm x 185

mm ILN with four 2.7 mm bolts. Group 3 (ILN8S) was made up of 8 mm x 185 mm ILN with four 3.5 mm screws. Group 4 (ILN8B) was made up of 8 mm x 185 mm ILN with four 3.5 mm bolts. Group 5 (br-DCP) was made up of broad dynamic compression plates with eight 3.5 mm screws (four on each bone segment). Group 6 (ILNn) was made up of the 185 mm novel interlocking nail and four 4/3.2 mm SCPs. All standard ILNs (ILN6s, ILN6b, ILN8S, ILN8B), plates (br-DCP), and locking bolts/screws used in this study were obtained from Innovative Animal Products, Rochester, MN. ILNn and SCPs used in this study were obtained from BioMedtrix, Boonton, NJ.

Mechanical Testing

Using custom designed loading fixtures; all specimens were mounted in an Instron servo-hydraulic testing machine (Instron model 1331, Instron Corp., Canton, MA) coupled to a 2500 lb (11,120 N) axial load cell (Model 1010AF-2.5K-B, Interface Inc., Scottsdale, AZ). The torsion and bending loading fixtures were instrumented with rotary encoders (torsion encoder- Bez BHW 16.05A72000, Baumer Electric, Southington, CT; bending encoders-RHS20D-5000-1/2-5/LD-1-M4, Renco Encoders, Goleta, CA) to document angular deformation of the constructs. In addition, the torsion fixture was instrumented with a 1200 lb*in (135 N*m) torque load cell (Model 5330-1200, Interface Inc., Scottsdale, AZ) to further document the magnitude of the applied torques. All specimens were tested non-destructively in torsion and 4-point bending (n=4 per testing protocol). All tests were run in load control for 10 cycles. Actuator displacement, rotary encoder output, and corresponding load/torque were documented in the tenth cycle. See Appendix 2 for detailed operating procedures for the torsion and bending tests.

Torsion Tests – Torsion tests were run using a 0.125 Hz sinusoidal waveform at a torque level of ± 5 N*m. The torque level chosen for the current study was identical to that used in previous biomechanical investigations.[9,21] The torsion fixture was equipped with a rotary encoder to record angular deformation and a torque load cell (Figure 3-6). See Chapter 2 for detailed information on torsion tests.

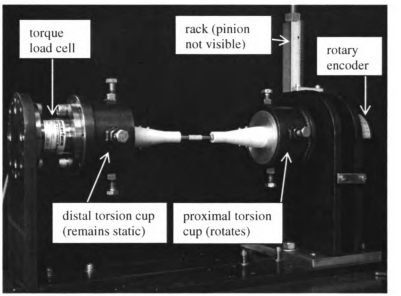

Figure 3-6. The torsion fixture shown with a loaded ILNn.

Bending Tests – Bending tests were run using a 0.125 Hz sinusoidal waveform at a bending moment of ± 3.5 N*m. The bending moment chosen for this study was identical to that used in previous biomechanical evaluations of fixation devices in a gap fracture model.[9,21] A specially designed fixture allowed for application of a pure bending moment over the entire bone model/implant construct. See Chapter 2 for detailed information on bending tests. Slight modifications were made to the bending cups and loading arm of the bending fixture to improve both performance and ease of use. In previous studies (Chapter 2), the loading arm had been connected to the bending cups via a steel shaft that was rigidly attached to the cups. The steel shaft was difficult to use because if there was

any out-of-plane misalignment between the cups and the linkage arms, they could not be connected. Another effect of misalignment when using the steel shafts was that binding would sometimes occur at various points throughout the loading cycle. The addition of stainless steel balls to the attachment point (Figure 3-7) between the loading arm and loading cups allowed for ease of connection between tests (Figure 3-8).

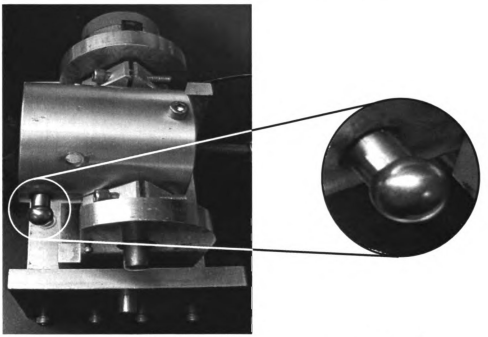

Figure 3-7. Stainless steel ball for connection between the cups and the loading arm.

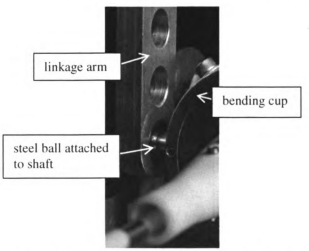

Figure 3-8. Linkage arm shown attached to the bending cups.

In addition to modification of the connection points from the loading arm to the bending cups, the loading arm itself was also modified (Figure 3-9).

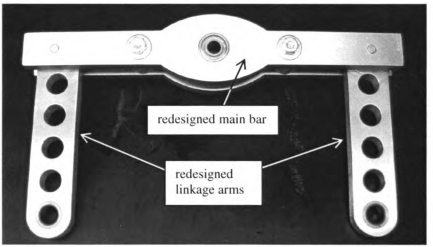

Figure 3-9. The modified loading arm.

Improvements in the loading arm included reducing the overall weight of the arm and minimizing friction between connection points. The loading arm was remade out of aluminum and cutouts were made to reduce its weight. The loading arm was also equipped with bearings to reduce friction at the connection between the loading arm and the actuator (Figure 3-10).

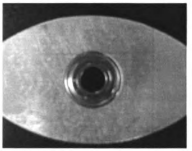

Figure 3-10. Loading arm bearings.

Another modification was made at the point of connection between the main bar and the linkage arms. Instead of a steel shaft, which allowed rotation in one plane, the linkage arm was now attached to the main bar with a partial ball joint (Figure 3- 11-A). This joint

allowed full rotation in one plane, as with the shaft, and also slight out-of-plane movement. The out-of-plane movement was restricted by the spacing between the two cross bars which make up the main bar (Figure 3-11-B). Figure 3-12 shows the fully assembled bending fixture.

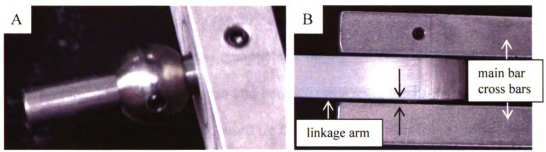

Figure 3-11. A) Partial ball joint for connection between main bar and linkage arms (the main bar is shown disassembled so the ball is visible). B) Linkage arm shown attached to main bar (spacing shown in black).

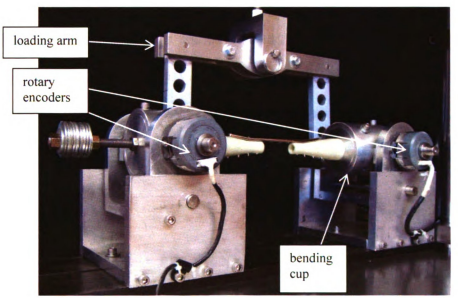

Figure 3-12. The bending fixture shown with a loaded br-DCP.

Data Acquisition

A load cell and/or a torque load cell coupled to the Instron actuator and to the torsion fixture, respectively, recorded applied loads (N) and torques (N*m) over time. These and actuator displacement (mm) were recorded at a sampling rate of 250 Hz. Since all constructs were tested under load control, construct compliance (slope of deformation versus load curve) was evaluated in the 10^{th} cycle. Construct compliance in bending and torsion was determined as the mean compliances during positive and negative loading. Construct angular deformation (torsion and bending) was recorded by rotary encoders in addition to redundant measurements based on the geometrical dimensions of the torsion and bending fixtures. Angular deformation of constructs in bending was calculated as described in Chapter 2. See Appendix 2 for detailed static analysis and calculations for torsion and bending tests.

The results of compliance and associated deformation between constructs were compared using a one factor ANOVA. Student-Newman-Keuls post-hoc tests were used whenever significant differences between groups were indicated ($p < 0.05$).

RESULTS

Values for AMI

The AMI of the 2.7 mm screw, 2.7 mm bolt, 3.5 mm screw, 3.5 mm bolt, 4.5 mm screw, and SCP was calculated. The AMI of 2.7 mm screws was approximately 25% of the 2.7 mm bolt (0.639 mm^4 and 2.607 mm^4). The AMI of various sections of the SCP (threaded section, 12.57 mm^4 [core, 4.0 mm]; tapered midsection, 8.24 mm^4 [core, 3.6 mm]; and smooth solid section, 5.15 mm^4 [core, 3.2 mm]) were always larger than those of the 3.5-mm (1.63 mm^4) or 4.5-mm (3.98 mm^4) screws (core diameter of the 3.5 and 4.5 mm screws, 2.4 and 3.0 mm, respectively[34]). In addition, the AMI for the threaded section of the SCP was 171% greater than that of a 3.5-mm bolt (7.36 mm^4). Whereas the AMI of the smooth section of the SCP was 316% and 129% greater than that of a 3.5 or 4.5 mm screw, respectively, it was 30% less than that of a 3.5 mm bolt.

Values of AMIs for the ILN6 (with 2.7 mm nail hole), ILN8 (with 3.5 and 4.5 mm nail holes), ILNn and 3.5-mm br-DCP were calculated (Table 3-1). The AMI values for the novel ILN at the nail holes were similar to those of an ILN8 with 3.5 mm screws and larger than those of an ILN8 with 4.5 mm screws in both the mediolateral and craniocaudal planes. The central section of the novel ILN had an AMI greater than that of a 3.5 mm br-DCP.

Section	ILN6 (2.7mm hole)	ILN8 (3.5mm hole)	ILNn	ILN8 (4.5mm hole)	br-DCP*
Solid central section	63.6	201.06	63.62	201.06	~ 59
Nail hole					
Mediolateral	19.8	65.6	62.1	37.94	~ 32
Craniocaudal	54.4	174.2	171.4	146.5	~ 500

Table 3-1. Nail and plate AMI values (mm^4).

* Values determined on the basis of a plate cross-section of approximately 3.9 X 11.95 mm and a hole cross-section of approximately 3.9 X 5.55 mm, assuming rectangular cross sections for the plate and hole.

Performance of Construct Development Fixtures

The goal of developing and using a synthetic bone model was two-fold. One reason was to eliminate the need of procuring specimens, which can require significant time, effort, and expense. Experimentally though, the elimination of biological specimens would potentially provide data which had much less deviation from specimen to specimen. For this to occur however, a reliable, efficient, and consistent method of preparing the bone-implant constructs had to be developed. With this in mind, several fixtures were specially designed, for preparation of the bone for implantation to mounting the construct in the loading fixture. Theoretically, the goal was to eliminate the possibility of human variation while preparing the specimens for mechanical testing.

The modification of the ILN-ESF alignment fixture was done to produce consistent br-DCP specimens by drilling pilot holes at the same location on the bone models from specimen to specimen. The plate locking mechanism ensured the plate's position with respect to the bone. Drilling of pilot holes was then carried out by locating

appropriate position with respect to the standardized plate hole locations; Figure 3-13 shows a sample bone model with pilot holes drilled using the alignment fixture.

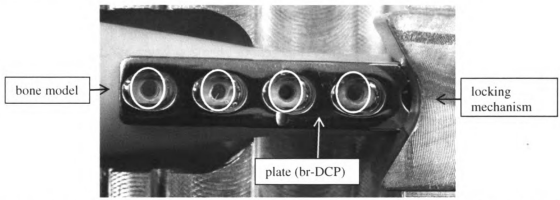

Figure 3-13. Pilot holes (white) drilled in the bone model with respect to the plate hole locations.

The ILN alignment fixture was used to create consistent ILN constructs. Figure 3-14 shows the consistency in overall length and osteotomy length between groups.

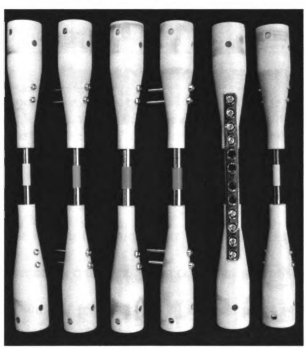

Figure 3-14. All constructs from left to right: ILN6s (yellow), ILN6b (orange), ILN8S (green), ILN8B (red), br-DCP, and ILNn (blue).

Torsion Tests

Construct Compliance – Construct compliance curves for the ILN6 (ILN6s and ILN6b) and ILN8 (ILN8S and ILN8B) constructs were bimodal, whereas compliance curves for the br-DCP and ILNn constructs were unimodal (Figure 3-15).

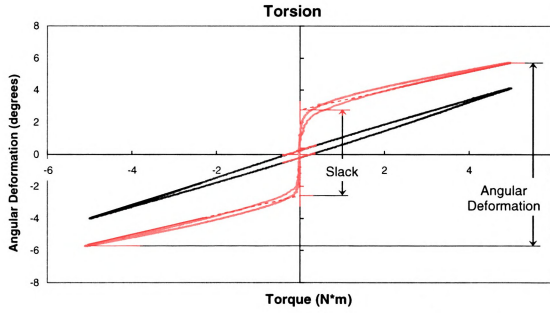

Figure 3-15. Typical compliance curves; note the bimodal response (red-ILN8B) which was characteristic of the 6 and 8 mm ILNs, and the unimodal response (blue-ILNn) that characterized the response of the br-DCP and ILNn constructs.

In the bimodal curves for the 6 and 8 mm ILN constructs, there was no quantifiable torque in the central region, which corresponds to the change in direction of torque. This region represented the slack in the construct and reflected an abrupt change in angular deformation without resistance to applied torque. Conversely, the unimodal shape of the compliance curves for br-DCP and ILNn constructs reflects a lack of slack, and a continuous resistance to deformation throughout and during reversals in construct loading. Construct compliances were calculated as the slope of the deformation versus torque curve in the range of 2.5-5 N*m. Since there was not a significant difference

between the positive and negative compliances within any of the groups ($p > 0.05$) compliance was calculated as the mean of the positive and negative loading curves. The ILNn constructs were significantly less compliant than that of the ILN6s and ILN6b constructs ([$p < 0.05$] – 0.87 ± 0.02 °/N*m, 1.65 ± 0.05 °/N*m, and 1.12 ± 0.04 °/N*m, respectively [Figure 3-16]). Construct compliance for the ILNn constructs was greater than that of both 8 mm ILN constructs (Table 3-2). See Appendix 4 for all pairwise comparisons.

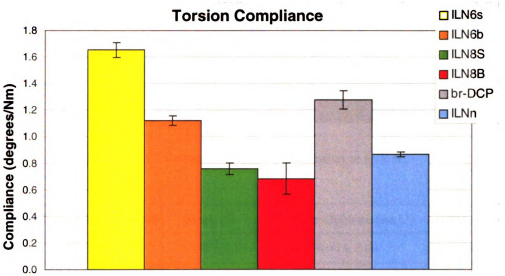

Figure 3-16. Construct compliances in torsion.

Construct Angular Deformation – Maximum angular deformation of the ILNn constructs was significantly less than all other constructs ([$p < 0.05$] Appendix 4 [Figure 3-17]). Construct slack, where present, was computed as the difference between the y-axis intercept of the compliance slope on the positive and negative loading curves (Figure 3-15). There was also no slack present in the ILN and br-DCP groups. Within groups where slack was present, the ILN6s construct had the most, and the ILN8B construct had the least (19.79 ± 2.1° and 5.6 ± 0.14°, respectively). Once slack was overcome (at high

torques), angular deformation for the ILNn constructs, was less than that for the 6 mm ILN constructs and greater than that for the 8 mm ILN constructs (Table 3-2). See Appendix 4 for all pairwise comparisons.

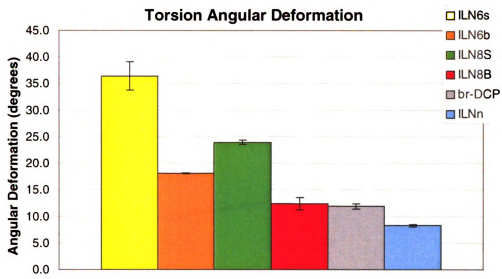

Figure 3-17. Construct angular deformation in torsion.

Construct	Compliance (°/N*m)	Slack (°)	Angular Deformation (°)	AD – Slack (°)
ILN6s	1.65 ± 0.05	19.79 ± 2.1	36.44 ± 2.68	16.66 ± 0.58
ILN6b	1.12 ± 0.04	6.85 ± 0.44	18.11 ± 0.11	11.26 ± 0.35
ILN8S	0.76 ± 0.04	16.31 ± 0.75	23.93 ± 0.39	7.61 ± 0.42
ILN8B	0.68 ± 0.1	5.6 ± 0.14	12.41 ± 1.14	6.81 ± 1.12
br-DCP	1.28 ± 0.07	0	11.93 ± 0.51	11.93 ± 0.51
ILNn	0.868 ± 0.02	0	8.29 ± 0.22	8.29 ± 0.22

Table 3-2. Torsion data (mean ± standard deviation).

Bending Tests

Construct Compliance – Similar to torsion tests, bending tests compliance curves for the ILN6 (ILN6s and ILN6b) and ILN8 (ILN8S and ILN8B) constructs were bimodal, whereas compliance curves for the br-DCP and ILNn were unimodal (Figure 3-18).

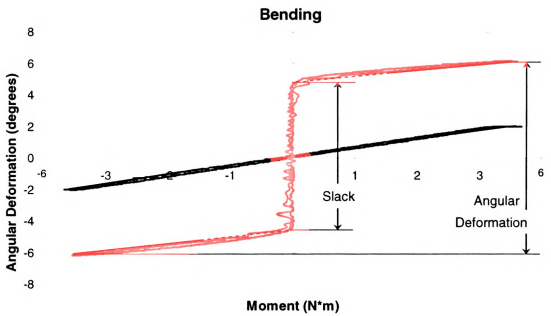

Figure 3-18. Typical compliance curves; note the bimodal response (red-ILN8B) which was characteristic of the 6 and 8 mm ILNs, and the unimodal response (blue-ILNn) that characterized the response of the br-DCP and ILNn constructs.

In the bimodal curves for the 6 and 8 mm ILN constructs, there was a region where the construct did not resist the applied moment. This region was defined as the slack in the construct. Due to the unimodal appearance of the compliance curves for the br-DCP and ILNn constructs, there was a continuous resistance to deformation throughout loading and reversal of loading. Construct compliances were computed as the slope of the deformation versus moment curve in the range 1.5-3.5 N*m. Since there was not a significant difference between the positive and negative compliances in any of the groups ($p > 0.05$), compliance was computed as the mean of the positive and negative

loading curves. In bending tests, ILNn constructs were significantly less compliant than 6 mm bolted constructs, however, ILNn and ILN6s constructs were not significantly different (Figure 3-19)(Table 3-3). ILNn constructs were significantly more compliant than that of the ILN8S and ILN8b constructs. See Appendix 4 for all pairwise comparisons.

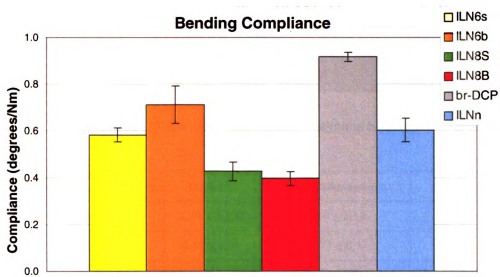

Figure 3-19. Construct compliance in bending.

Construct Angular Deformation – Maximum angular deformation of the ILNn constructs was significantly less than all 6 and 8 mm ILN constructs in bending ([$p < 0.05$] Figure 3-20 [Table 3-3]). There was also no slack present in the ILN and br-DCP groups in either mode of testing. The constructs locked with screws (ILN6s and ILN8S) had more slack ($9.79 \pm 1.21°$ and $9.03 \pm 1.06°$, respectively), than the constructs locked with bolts ($6.81 \pm 0.4°$ for ILN6b and $4.32 \pm 0.58°$ for ILN8B). Once slack was overcome (at high moments), angular deformation for the ILNn constructs was less than that of the 6 mm ILN constructs and greater than that of the 8 mm ILN constructs (Table 3-3). See Appendix 4 for all pairwise comparisons.

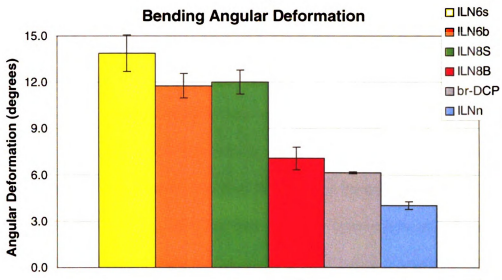

Figure 3-20. Construct angular deformation in bending.

Construct	Compliance (°/N*m)	Slack (°)	Angular Deformation (°)	AD – Slack (°)
ILN6s	0.58 ± .03	9.79 ± 1.21	13.87 ± 1.18	4.08 ± 0.24
ILN6b	0.71 ± .08	6.81 ± 0.4	11.77 ± 0.8	4.96 ± 0.56
ILN8S	0.43 ± .04	9.03 ± 1.06	12 ± 0.79	2.98 ± 0.33
ILN8B	0.4 ± .03	4.32 ± 0.58	7.07 ± 0.72	2.75 ± 0.15
br-DCP	0.92 ± .02	0	6.15 ± 0.07	6.15 ± 0.07
ILNn	0.6 ± .05	0	4.03 ± 0.25	4.03 ± 0.025

Table 3-3. Bending data (mean ± standard deviation).

DISCUSSION

This study compared the mechanical properties of a novel interlocking nail designed for the treatment of diaphyseal fractures in mid-size dogs (body weight of approximately 30 to 35 kg) to those of standard 6-mm and 8-mm ILNs available in the USA. It was hypothesized that the bending and torsional compliances of novel ILN constructs would be significantly less than those of the currently available 6 mm ILN constructs, and that bending and torsional angular deformation of the novel ILN constructs would be less than currently available 6 and 8 mm ILN constructs. It was also hypothesized that angular deformation of the novel ILN and br-DCP constructs would be continuous throughout loading, whereas there would be slack during angular deformation of currently available ILN constructs. The results of the torsion and bending tests in the present study support the above hypotheses. Specifically, the compliance of the ILNn construct was significantly less than all other constructs tested in this study. Furthermore results of the torsion and bending tests on the ILNn constructs indicated a continuous resistance to deformation throughout loading and reversal of loading directions, whereas slack was present during reversal of loading in currently available ILN constructs. On the basis that there was no slack for the novel ILN in torsion or bending, it was determined that the ILNn described here had better torsional and bending stability, compared with that for the currently available ILNs. What is also important to consider, is that the loading curves of the ILNn constructs were similar to the br-DCP construct (no slack, constant resistance to applied load). This suggested that the novel ILN design may improve the biomechanical environment for fracture healing.

Clinical studies have revealed intraoperative or postoperative instability of interlocking nails.[3,17] In these studies, 12% to 14% of the animals have delayed healing or require supplementation of the initial ILN repair to provide adequate stability. Similarly, delayed union rates as high as 18% have been reported in humans treated by use of tibial nails without reaming of the medullary cavity.[22] Although the optimal mechanical environment favorable to bone healing remains controversial, it is generally accepted that excessive interfragmentary motion delays bone healing, in contrast to studies where results for axial micromotion is controlled.[23-25] In particular, the effect of shear motion on fracture healing continues to be debatable. Numerous studies in dogs and sheep have indicated deleterious effects of torsional and shear motions on early bone healing and functional recovery.[2,15,26,27] Another study,[28] on rats has revealed that the callus 2 and 4 weeks after surgery was significantly larger in tibial fractures subjected to local shear strains than those with rigid stabilization of the fracture.

Results of such studies, supported by experimental evidence of construct instability with current ILNs,[7,9] emphasize the need for a more effective ILN design. In an attempt to investigate potential correlations between construct stability and functional recovery, an *in vitro* and *in vivo* study was conducted to evaluate an experimental nail featuring bolts threaded into the nail holes using a tibial gap fracture model in sheep.[29] The study revealed that although experimental and conventional nails had similar stiffnesses in mediolateral bending and axial compression, the experimental nail was significantly stiffer in shear and craniocaudal bending. Additionally, the experimental nail had a slightly higher stiffness in torsion. As a result, the experimental nail group had significantly smaller interfragmentary motion throughout the 9 weeks of the experiment.

This was suspected to explain the resultant superior bone healing (as evaluated by use of histomorphometry, radiography, and *ex vivo* biomechanical testing) and faster, more complete functional recovery of the patient (as evaluated by use of gait analysis).[29]

To increase construct stability by eliminating motion at the interface between the nail and locking device the SCP was designed with a central Morse taper. A Morse taper features a matching trunnion (male component) and bore (female component) and is commonly used to join modular components during total hip arthroplasty.[30] The tapered design also facilitates the insertion of the SCP by providing a self-centering feature, even when there is slight misalignment between the cortical pilot hole and nail hole. This may help reduce the incidence of missed locking devices due to misaligned holes during treatment of fractures with ILNs.

The strength and failure pattern of ILNs depend in large part on the design and size of the nail hole and locking device.[6,31,32] In comminuted fractures, implants are mainly subjected to bending stresses.[18] Therefore, the AMIs used in the study reported here were calculated with respect to theoretical bending conditions. The AMI of an implant is a structural property that characterizes the geometric distribution of a material with respect to the axis of loading. Based on strength of materials bending theory, an implant with a larger AMI will sustain lower stresses during cyclic loading, which in turn will extend its fatigue life.[17] One limitation of early ILNs designed for veterinary use was the weakness of the nail holes, which, because of the sharp local decrease in AMI, acted as stress concentrators that led to nail failure.[17,33,34] On the basis of the AMIs, ILNs are weakest at the nail hole in mediolateral bending. Reducing the diameter of the screw hole from 4.5 mm (early 8 mm ILN design) to 3.5 mm (current 8 mm ILN design) results in a

5.7-fold increase in local AMI, which translates into an 8-fold increase in fatigue life of an 8 mm nail.[33] This design change improves structural properties of a nail to the detriment of a thinner or weaker screw as indicated by approximately a one third decrease in AMI. [34]

Because of the failure patterns of 6-mm nails and screws and increased strength of 8 mm ILNs, the novel ILN reported here was devised so that the AMI of the locking device was equal to or greater than that of the 4.5 mm screw and the AMI of the nail at the holes was similar to that of the ILN8 with 3.5 mm screws. Design of the SCP was such that its smallest AMI (ie, AMI for the peg section) had to be greater than that of a 4.5 mm bone screw; AMI for the peg section was 5.15 mm^4, whereas AMI for the 4.5 mm bone screw was 3.98 mm^4, which represented an increase of approximately 30%. At the same time, the smallest AMI for the SCP could be smaller than that of a 3.5 mm bolt (7.36 mm^4). This design constraint was selected on the basis of the fact that failure of 4.5 mm screws has not been reported for the first generation of 8 mm ILNs. Furthermore, although the corresponding AMI of the novel ILN (62.1 mm^4) was slightly smaller than that of the ILN8 with a 3.5 mm screw (65.6 mm^4), it is 64% greater than that of an ILN8 with a 4.5 mm screw (37.94 mm^4), thus suggesting that the novel ILN should have an estimated fatigue life similar to that of the currently available 8 mm ILNs with 3.5 mm screws. Moreover, the improved stability of the novel ILN (no slack) could potentially result in shorter healing time, thereby rendering the slight theoretical decrease in fatigue life of the novel ILN clinically irrelevant.

The hourglass design of the nail provides several potential benefits. First, this design should contribute to preserving the endosteum and improve restoration of the

medullary blood supply after implantation, [2] that, in turn, may enhance the rate of bone healing.[13,14] This shape should also facilitate implantation of the nail in curvilinear bones by limiting contact between the nail and endocortices. The use of a relatively large nail is often guided by the necessity to have a strong locking mechanism.[33] Consequently, it is recommended that the largest possible nail be used, principally on the basis that the fatigue life of an 8 mm nail is 10 times that of a 6 mm nail.[33] Alternatively, a comparable fracture could be treated successfully by use of a 3.5 mm br-DCP.[35] Because the AMI of the solid section of a 6-mm nail (approx 64 mm^4) is similar to that of a 3.5-mm br-DCP (approximately 59 mm^4), it can be argued that the strength of an ILN8, which has an AMI for the solid section of 201 mm^4, is not warranted. Furthermore, the use of larger medullary implants can substantially impede the cortical blood supply, which in turn could negatively affect bone healing.[2]

Finally, the bullet-shaped distal tip of the nail was designed to facilitate reduction of the fracture, particularly with regard to restoring length of the bone without increasing the risk of penetration of the distal joint associated with the use of trocar points. The oblong tip of the novel ILN could facilitate insertion through the proximal metaphysis and permit deep anchorage in the distal metaphysis, compared with results for the flat truncated tip in currently available ILNs. This may allow for treatment of a greater variety of fractures including those affecting the metaphyses.

Results of the torsion and bending tests indicate that the compliance of the ILNn is less than the 6 mm constructs but greater than the 8 mm constructs. In comparison to the 6 mm ILNs, the ILNn has the same AMI in the central section of the nail (6 mm diameter); therefore the nails should have the same ability to resist deformation.

However, the load applied to the bone is essentially transferred to the nail through bending of the locking mechanism.

In the current study, the torsional and bending forces on the nail result in applied bending and shearing forces to the locking mechanism. Therefore, given an equal diameter of the solid central section of the nails (ILN6s, and ILN6b, and ILNn), differences in compliance are only attributable to mechanical properties of their respective locking mechanisms. This is shown under torsion, where the ILN6s, ILN6b and ILNn constructs decreased in compliance (approximately 1.65, 1.12, and 0.87 °/N*m, respectively) as the AMIs of their corresponding locking mechanisms increased. It should be noted however, that the torsional compliance of an implant is inversely proportional to its polar moment of inertia (approximately 1.28 mm^4, 5.22 mm^4, and 16.48 mm^4, respectively) as opposed to its AMI (0.64 mm^4, 2.61 mm^4, and 8.24 mm^4), which is inversely proportional to the bending compliance of an implant. The larger torsional and bending compliance of the novel ILN construct, compared with that of the 8 mm ILN constructs (ILN8S and ILN8B), was attributed to the difference in the core diameter of the solid section of the nails (6 and 8 mm for the novel ILN and ILN8 constructs, respectively), which resulted in a > 3-fold increase in AMI. Interestingly, the torsional compliance of the ILNn in the current study was very similar to the compliance of a 6 mm ILN locked with an external fixator, as tested in Chapter 2 (both are approximately 0.87 °/N*m).

Primarily because of slack in the 6 and 8 mm ILN systems (ILN6s, ILN6b, ILN8S, and ILN8B) angular deformation of the currently available ILN constructs in bending and torsion was greater than that of the novel ILN construct. Slack, which

corresponds to a lack of resistance to applied load, has been associated with looseness between the locking mechanism and nail.[9] When slack was removed, at high torsional and bending loads, differences in angular deformation decreased drastically. Consider the comparison of the overall angular deformation of the ILN6s construct to that of the ILNn construct in bending. The ILN6s constructs deformed approximately 350% more than the ILNn constructs, including deformation incurred due to slack in the system. After slack was removed, the angular deformation of the ILN6s construct (approx. 4.075°) was no longer significantly different than the ILNn construct (approx. 4.025° [$p = 0.821$]). Construct slack results in uncontrolled, acute motion at the fracture site, which in turn likely generates high local strains. Since shear strains can be detrimental to bone healing,[36-38] slack in torsion or bending or both could explain some of the cases of delayed and non-union seen clinically after repair of fractures with standard ILNs.

CONCLUSION

The study reported here suggested that re-engineering of the locking mechanism in a novel hourglass-shaped ILN has eliminated the instability associated with the use of current ILNs inserted, without reaming of the medullary cavity. Furthermore, the improved torsional and bending stability of the construct matched that of a comparable br-DCP construct, a device routinely used to treat comminuted diaphyseal fractures. In contrast to plate osteosynthesis, an ILN can be applied at remote fracture sites and be used to reduce and stabilize fractures by use of a closed technique. This less invasive approach to fracture repair improves early bone healing.[39] Because of the potential combined mechanical and biological benefits of this novel hourglass shape, the novel ILN could represent an effective and safe alternative to plate osteosynthesis while preserving the advantages of nails that do not require intramedullary reaming.[39] Additional biomechanical studies to evaluate fatigue strength of the novel ILN are warranted. In vivo studies of the novel ILN should also be conducted to fully assess the potential use of the new hourglass-shaped ILN.

REFERENCES

1. Kyle RF, Schaffhausen JM, Bechtold JE. Biomechanical characteristics of interlocking femoral nails in the treatment of complex femoral fractures. *Clin Orthop Relat Res* 1991: 169-173

2. Klein P, Opitz M, Schell H, et al: Comparison of unreamed nailing and external fixation of tibial diastases--mechanical conditions during healing and biological outcome. J Orthop Res 22: 1072-1078, 2004

3. Duhautois B: Use of veterinary interlocking nails for diaphyseal fractures in dogs and cats: 121 cases. Vet Surg 32: 8-20, 2003

4. Knothe U, Knothe Tate ML, Klaue K, et al. Development and testing of a new self-locking intramedullary nail system: testing of handling aspects and mechanical properties. *Injury* 2000; 31: 617-626

5. Laflamme GY, Heimlich D, Stephen D, et al. Proximal tibial fracture stability with intramedullary nail fixation using oblique interlocking screws. *J Orthop Trauma* 2003; 17: 496-502

6. Lin J, Lin SJ, Chen PQ, et al. Stress analysis of the distal locking screws for femoral interlocking nailing. *J Orthop Res* 2001; 19: 57-63

7. Schandelmaier P, Krettek C, Tscherne H. Biomechanical study of nine different tibia locking nails. *J Orthop Trauma* 1996; 10: 37-44

8. Suber JT, Basinger RR, Keller WG. Two unreported modes of interlocking nail failure: breakout and screw bending. *VCOT* 2002; 15: 228-232

9. von Pfeil DJ, Déjardin LM, DeCamp CE, et al: In vitro biomechanical comparison of a plate-rod combination-construct and an interlocking nail-construct for experimentally induced gap fractures in canine tibiae. Am J Vet Res 66: 1536-1543, 2005

10. Basinger RR, Suber JT: Two techniques for supplementing interlocking nail repair of fractures of the humerus, femur, and tibia: results in 12 dogs and cats. Vet Surg 33: 673-680, 2004

11. Mayr E. [Tibial fractures]. *Chirurg* 2002; 73: 642-661

12. Heim D, Schlegel U, Perren SM: Intramedullary pressure in reamed and unreamed nailing of the femur and tibia--an in vitro study in intact, human bones. Injury 24 Suppl 3: S56-63, 1993

13. Krettek C. [Principles of intramedullary fracture stabilization. 1]. *Unfallchirurg* 2001; 104: 639-651

14. Runkel M, Wenda K, Stelzig A, et al: Bone remodeling after reamed and unreamed intramedullary nailing: A histomorphometric study. Unfallchirurg 97:385-390, 1994

15. Duda GN, Mandruzzato F, Heller M, et al. Mechanical boundary conditions of fracture healing: borderline indications in the treatment of unreamed tibial nailing. *J Biomech* 2001; 34: 639-650

16. Hibbeler RC. *Mechanics of Materials*. 3rd ed. Upper Sadle River: Pearson Prentice Hall, 2004

17. Dueland RT, Vanderby R, Jr., McCabe RP. Fatigue study of six and eight mm diameter interlocking nails with screw holes of variable size and number. *Vet Comp Orthop Traumatol* 1997; 10: 194-199

18. Muir P, Johnson KA, Markel MD. Area moment of inertia for comparison of implant cross-sectional geometry and bending stiffness. *VCOT* 1995; 8: 146-152

19. Milgrom C, Giladi M, Simkin A, et al. The area moment of inertia of the tibia: a risk factor for stress fractures. *J Biomech* 1989; 22: 1243-1248

20. MATLAB and Simulink. Matlab Version 7.0.4. The MathWorks, Inc. Natick, MA. 2003

21. Bouvy BM, Markel MD, Chelikani S, et al. Ex vivo biomechanics of Kirschner-Ehmer external skeletal fixation applied to canine tibiae. Vet Surg 22: 194-207, 1993

22. Goldhahn S, Moser R, Bigler R, et al. [Treatment methods and outcomes of tibial shaft fractures in Switzerland. A prospective multicenter study of the Swiss AO]. *Swiss Surg* 2000; 6: 315-322

23. Goodship AE, Kenwright J. The influence of induced micromovement upon the healing of experimental tibial fractures. *J Bone Joint Surg Br* 1985; 67: 650-655

24. Lewallen DG, Chao EY, Kasman RA, et al. Comparison of the effects of compression plates and external fixators on early bone-healing. J Bone Joint Surg Am 66: 1084-1091, 1984

25. Wu JJ, Shyr HS, Chao EY, et al. Comparison of osteotomy heling under external fixation devices with different stiffness characteristics. J Bone Joint Surg Am 66: 1258-1264, 1984

26. Aron DN, Palmer RH, Johnson AL. Biologic strategies and a balanced concept of repair of highly comminuted long bone fractures. Comp Cont Ed Pract Vet 17: 35-38, 1995

27. Augat P, Burger J, Schorlemmer S, et al. Shear movement at the fracture site delays healing in a diaphyseal fracture model. *J Orthop Res* 2003; 21: 1011-1017

28. Claes LE. Biomechanics of fracture repair and fracture fixation. In: Mow VC, Hayes WC, eds. Basic Orthopaedic Biomechanics and Mechano-Biology. Philadelphia: Lippincott Williams and Wilkins; 2005

29. Kaspar K, Schell H. Seebeck P et al. Angle stable locking reduces interfragmnetary movements and promotes healing after unreamed nailing. Study of a displaced osteotomy model in sheep tibiae. J Bone Joint Surg Am 87: 2028-2037, 2005

30. Pennock AT, Schmidt AH, Bourgeault CA. Morse-type tapers: factors that may influence taper strength during total hip arthroplasty. *J Arthroplasty* 2002; 17: 773-778

31. Gaebler C, Stanzl-Tschegg S, Heinze G, et al. Fatigue strength of locking screws and prototypes used in small-diameter tibial nails: a biomechanical study. *J Trauma* 1999; 47: 379-384

32. Gaebler C, Stanzl-Tschegg S, Laube W, et al. The fatigue strength of small diameter tibial nails. *Injury* 2001; 32: 401-405

33. Dueland RT, Johnson KA, Roe SC, et al. Interlocking nail treatment of diaphyseal long-bone fractures in dogs. *J Am Vet Med Assoc* 1999; 214: 59-66

34. Brinker WO, Olmstead ML, Sumner-Smith G, et al. *Manual of Internal Fixation in Small Animals.* Ist ed. Berlin: Springer-Verlag, 1998; 125

35. Piermatti DL, Flo GL. *Brinker, Piermattei, and Flo's Handbook of Small Animal Orthopedics and Fracture Repair.* Third ed. Philadelphia: W.B. Saunders Company, 1997

36. Claes LE, Eckert-Hubner K, Augat P. The effect of mechanical stability on local vascularization and tissue differentiation in callus healing. J Ortho Res 20: 1099-1105, 2002

37. Claes LE, Heigele CA. Magnitudes of local stress and strain along bony surfaces predict the course and type of fracture healing. J Biomech 32: 255-266, 1999

38. Claes LE, Heigele CA, Neidlinger-Wilke C, et al. Effects of mechanical factors on the fracture healing process. Clin Orthop Relat Res Suppl 355: S132-S147, 1998

39. Grundnes O, Reikeras O. The importance of the hematoma for fracture healing in rats. *Acta Orthop Scand* 1993; 64: 340-342

APPENDIX ONE

FIXTURE SOPS

CHAPTER ONE

Plate Bending - Depending on the plate you are bending, you will need to change the arm, the plate holder, and the hardened steel piece (fulcrum). The 3.5mm LC-DCP has a different set than 3.5mm broad DCP. They are marked appropriately.

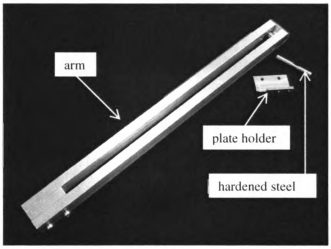

Figure A1-1. MSU BP lever arm.

- Make sure all the adjustment screws are loose and the block should slide easily.
- Place the plate in the plate holder and place the peg and tighten and plate holder screws with the plate. One peg is enough. Do not use two pegs, see figure below.
- Once the appropriate angle and level of the bend are obtained, loosen only the screws on the plate holder to take the plate in/out.

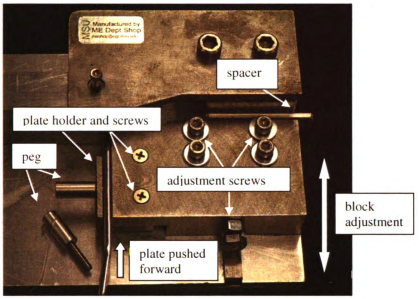

Figure A1-2. MSU BP plate holder and adjustments.

- Slide the block so the plate is at the correct level for bending. Spacer can be used if needed to. Double check to make sure the plate is pushed forward and the bending level is correct. The plate may be bent at this time.
- Once the correct level is identified, tighten all the adjustment screws.

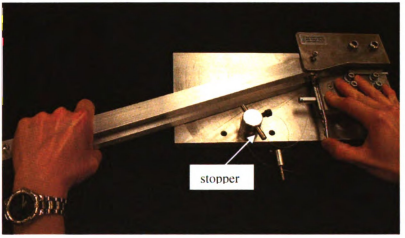

Figure A1-3. MSU BP with the plate pushed forward.

- After the plate is bent, loosen only the screws on the plate holder (not the adjustment screws).

- Inspect the angle of the bend; adjust the stopper as necessary to obtain the desired angle. Once the appropriate angle and level of the bend are obtained, loosen only the screws on the plate holder to take the plate in/out.
- You may start bending the rest of the plates. Remember to make sure the bending level is correct and the plate is pushed forward each time you load the plate.

Strain Gage Selection and Application - Strain gage application was performed according to manufacturer's specifications (Vishay Micro-Measurements Inc.). Clean latex gloves were worn during the surface cleaning process and application of the strain gages so the bonding surface was not contaminated. The first step was to clean and prepare the surface of the implant (Surface Preparation, Vishay Micro-Measurements Inc.) This was done using M-Prep Conditioner A and 320 grit sand paper. The whole surface of the implant was wet sanded with special attention given to the areas where the gages would be applied. Next, the sanding residue was removed from the surface by rinsing it with M-Prep Conditioner A and wiping it clean with cotton gauze. This procedure was repeated with clean gauze until there was no more sanding residue visible on the gauze after wiping the surface. The surface was then rinsed with M-Prep Neutralizer 5A and wiped again with a clean piece of cotton gauze.

Strain gage selection was based on the required size of the gage and the estimated levels of strain, which would be incurred during testing. Strain values were not expected to exceed 4000 με. The selected strain gage (EA-06-031DE-350 Vishay Micro-Measurements) was rated for 3% strain, and had a gage length of 0.79 mm and a grid width of 0.81 mm.

The overall size of the gage, which includes the plastic backing that the gage is attached to, was 6.9 mm and 3.0 mm in length and width, respectively. This presented a problem due to the size of the gage with respect to the area of the plate where it was to be adhered. Therefore, the gage backing had to be carefully trimmed, without interrupting the actual grid, to allow the gage to fit properly. After trimming of the backing, the overall size of the gage was 4 mm by 1mm in length and width, respectively. Cellophane tape was then placed over the gage to allow for accurate positioning of the gage on the plate.

Positioning of the gage on the specimens was also difficult, once again due to the small tolerances between the features of the plates and the strain gage area. Special attention was given to make sure that there were no corners or edges of the gages hanging over the edge of a hole or the edge of the plate. Because strain gages are uniaxial, and measure an average strain over a finite area, it was important to align them on the axes where maximum strain was thought to occur. Therefore, prior to placing the gages on the plates, a line was sketched to mark the longitudinal and transverse axes. The longitudinal axes were located 1 mm from the edge of the plate. The transverse axis was identified as the line along which the bend was centralized. Neither line jeopardized the integrity or cleanliness of the plate surface. The gage was then carefully aligned with both axes and taped to the surface of the plate.

Once desired gage location was achieved, M-Bond 200 Adhesive and M-Bond 200 Catalyst C were used to attach it to the specimen. The tape was slowly peeled back at a large angle, making sure the gage was still attached to the tape, and M-Bond 200 Catalyst C was delicately applied directly to the bottom of the gage. The catalyst was

allowed to dry for 30 seconds. M-Bond 200 Adhesive was then applied sparingly (1-2 drops) to the plate surface. The gage was then immediately pressed onto the surface of the plate applying gradual pressure to the length of the gage to squeeze out excess glue, but care was taken not to press too hard and squeeze out all of the glue. Firm pressure was applied to the gage overnight using clamps. It should be noted that the clamps had soft tips and applied pressure over the entire area of the gage so as not too damage the grid of the gage with any point loads. The tape was removed at a sharp angle ensuring that the gage was adhered to the plate surface and no longer attached to the cellophane tape. The process of gluing the strain relief tabs to the plate was exactly the same, without the extreme attention given to their exact location. This process was carried out on both the medial and lateral sides of the plate, resulting in dual uniaxial strain measurement (medial and lateral) of the specimens. The strain gages were check for a their appropriate resistance readings (350 ± 0.2% Ω) with an ohmmeter prior to moving on to the next step.

The next step in preparation of the plates was to prepare the wires and to solder the relief wire to the strain gage tabs and the strain relief tabs. Single strand, solid copper wire with a polyurethane enamel coating (American Wire Gauge size 34) was used as the strain relief wire.

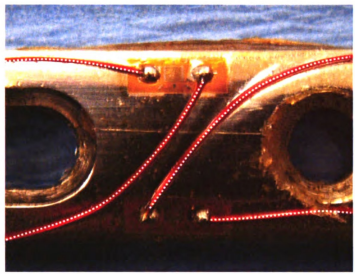

Figure A1-4. Close-up view of solder joint attaching the copper wire (dashed white lines) to the strain gage (strain relief tabs not shown).

Relief wire soldering followed standard soldering procedures at a temperature of 500°. The next step was to solder the 3-conductor cable (M-Line accessories, 326-DSV 6507, Measurements Group) to the strain relief tabs. Once again, standard soldering procedures were followed. The final step in preparation of the plates was to apply a coating material over the strain relief tabs to secure the 3-conductor cable and the relief tab connection (M-Coat B Nitrile Rubber Coating, M-Line Measurements), manufacturer's application specifications were followed. The fully prepared implant is shown below. The 3-wire cable was checked again for appropriate resistance of the gages according to manufacturer's specifications. It should be noted that the 3-conductor cable also had an inherent resistance, which was taken into account on the final measurements of resistance.

Figure A1-5. Fully prepared HP implant (dashed white lines are electrical lines).

CHAPTERS TWO AND THREE

Bone Model Drilling **-** Based on the 30% glass-filled structural nylon (Alro Plastics, Jackson, MI), custom made by Olympia Tool, St. Johns, MI (contact person Todd Deitrich 989-224-4817). Before starting, make sure the bushings are the correct size. Change the bushings based on the SOP provided.

- Fit the larger end of the bone model (30mm) in the fixture. Make sure it is well seated with no wiggle room, yet you should be able to take them out with mild force. Remove any drilling debris from previous drilling.
- **Note**: some bone models are made slightly larger. In this case, you want to sand the larger end down with 220-grade sandpaper to a point where it can just fit in the fixture like in step one.

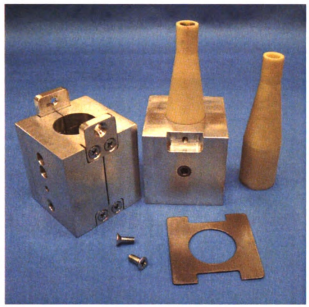

Figure A1-6. Disassembled drill guide.

- Fit the top and bottom pieces together and tighten the screws just slightly. Adjust the pieces until all the edges are smooth and the surface is flat.

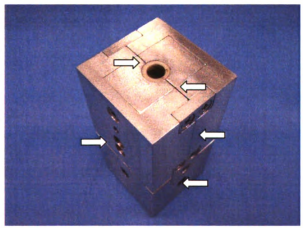

Figure A1-7. Make sure all edges pointed out by the white arrows are flush and flat.

- Once they are lined up, tighten the screws sequentially (finger tight).
- When drilling the interlocking screw holes, make sure your drill goes in and out the bushing easily and perpendicular to the bushing. Make sure you don't hold the fixture too tight, so the drill can go down the path of least resistance inside the bushing without damaging the wall of the bushing or the drill bit.

- Since the interlocking screw holes are perfectly aligned, you may drill one side at a time.

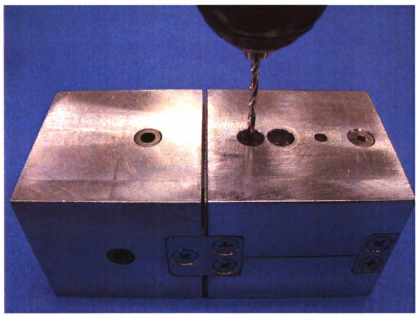

Figure A1-8. View of drill bit insertion into drill guide.

- Use 5.5mm drill bit for the linkage hole. You may drill one side and flip around to drill the other side.
- Loosen all the screws, but remove the two most distal screws and take the fixture apart. Make sure you get rid of all the plastic debris in the fixture and inside the bushing before drilling the next bone model.
- Over-drill the cis cortex with the following:
    - For 2.7mm bolt, over drill with 7/64 (2.76mm in metric system) drill bit
    - For 3.5mm bolt, over drill with 9/64 (3.55mm in metric system) drill bit

- **Note**: Make sure you label the size of the hole you drilled if you are going to put various size holes on the same bone.

Bushing Adjustment - Change bushings based on the chart provided below for different size screw or bolt.

- Remove the top two halves as shown on the picture.

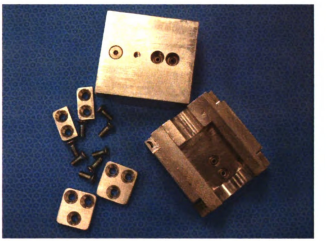

Figure A1-9. Disassembled top portion of drill guide.

- Next, remove the inner housing for the bushing. The inner housing has two set-screws holding the bushing down.
- Loosen the set-screws and change the bushings to the desired size.

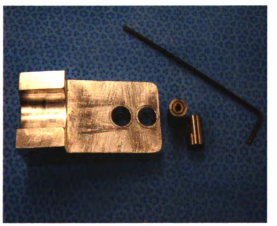

Figure A1-10. View of inner housing containing drill guide bushings.

- Make sure when the bushings are inserted, the notch on the bushing line up with set-screws and the bushings should not protrude from the slanted side (this is where the bone contact would be).

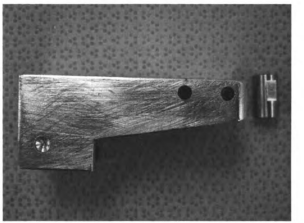

Figure A1-11. View of drill guide inner housing profile.

Desired size	Drill bit size	Bushing size
6mm ILN, 2.7mm screw	2.0mm	2.0mm
6mm ILN, 2.7mm bolt	2.7mm	2.7mm
8mm ILN, 3.5mm screw	2.5mm	2.5mm
8mm ILN, 3.5mm bolt	3.5mm	3.5mm
MSU ILN cis-cortex	4.0mm	4.0mm
MSU ILN trans-cortex	3.0mm	3.0mm

Table A1-1. Bushing selection for desired screw/bolt size.

ILN Placement -

- Insert the bolts from the cis cortex, half way in.
- Place the nail in the bone model.
- Insert the bolts all the way in.
- Make sure that the nail hole is centered.
- Similar placement for the rest of the bolts.
- For screw placement, the only difference is that you need to tap the bone first.
- Tap 2.7mm screw with 2.0mm tap, 3.5mm screw with 2.5mm tap.
- Looseness should be present if the traditional ILN is used. If not, the bolts/screws may be bent or the holes are not lined up.

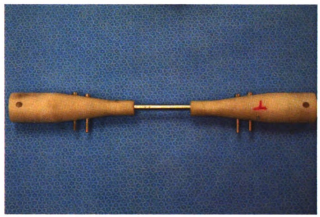

Figure A1-12. View of fully assembled construct.

Size of nail	Bolt/Screw size
6mm	2.7mm
8mm	3.5mm

Table A1-2. Bolt/screw selection for desired nail size.

ILN-ESF Placement -

- Similar to ILN bolt placement, but instead of the bolts, place the 2.7/3.2mm hybrid pins into the pre-drilled holes.
- 1 cm should be removed from the most distal and proximal pins with enclosed pin cutter. This should be done before placement into the bone model. The shorter pins will allow easier placement.

Figure A1-13. Enclosed pin cutter.

- All the hybrid pins should be perfectly aligned from all angles.
- Pre-place all the clamps and rod, but do not tighten them at this point.
- Place the construct in the ILN-ESF alignment fixture (Figure A1-14) with distal aspect facing left.

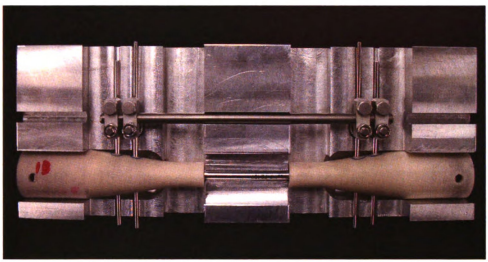

Figure A1-14. ILN-ESF in alignment fixture.

- Make sure that all the bones, clamps, and rods seat properly. There should not be any wiggle room.
- Tighten all the top screws first (the lag screw), then the bolts with torque wrench (4.5 N*m is the ideal torque).

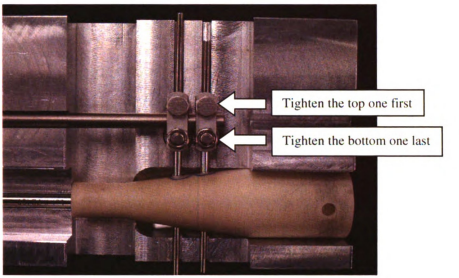

Figure A1-15. Correct screw tightening order.

Foam Tube SOP -

- Take out about 30" of aluminum foil. Roll the aluminum foil around the DePuy "hip drill 45° angle" plastic tube. Make sure one side is flush against the top of the tube.

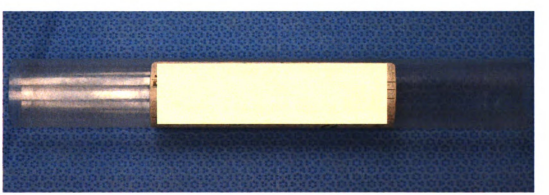

Figure A1-16. Depuy "hip drill 45° angle" plastic tube.

- Tape down the edge with several pieces of scotch tape or masking tape. Gently smash the side of the aluminum roll that is longer than the plastic tube, but make sure that the end of the tube is still round.

Figure A1-17. Depuy plastic tube with aluminum foil shell.

- Flatten the bottom from inside with the iron plunger.

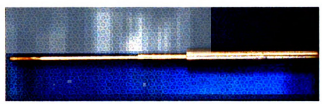

Figure A1-18. Iron plunger.

- Take the plastic tube out.
- Mix 15cc of mixture A with 15cc of mixture B in the urine cup. Mix them very fast with a tongue depressor for about 10-15 seconds. Make sure you add A to B, not B to A.
- Pour the mixture down the tube and set it straight up for about 20 min.
- Remove all the foil. Remove as much foil at the distal end as possible. Don't worry if you have leftover foil on the distal end. Cut approximately 1/3 of the proximal end off since the density will be a bit different.

Foam Lathing SOP

Purpose and Use **-** The foam is meant to simulate cancellous bone in the synthetic bone model. It is inserted into the metaphyseal region of the bone and it's sole purpose it to provide otherwise non-existent vertical stability (parallel to the screws) to keep the ILN centered throughout testing. If the foam is not present, the nail will fall to the bottom of

the inner diaphyseal diameter, the off axis position of the nail will erroneously affect the positive and negative loading data.

The foam lathe bit has been designed to fill approximately 10 mm proximal to the beginning of the taper and 15-20 mm distal to the beginning of the taper (30 mm was the original length, this was then reduced to 25 mm). The distal dimensions were specifically chosen to provide support for the nail only, and to not reach the nail screw interface.

Materials

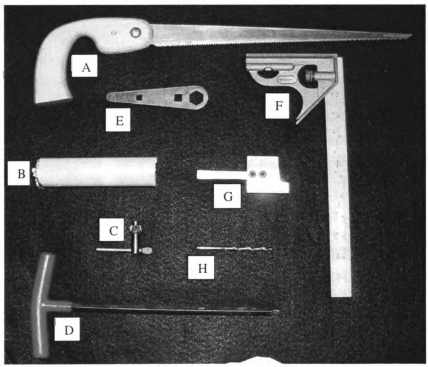

Figure A1-19. Foam lathing materials, including:

A) hand saw
B) foam cylinder
C) drill bit chuck
D) lathe head chuck
E) foam lathe bit chuck
F) t-square
G) foam lathe bit (30 mm version shown)
H) drill bit

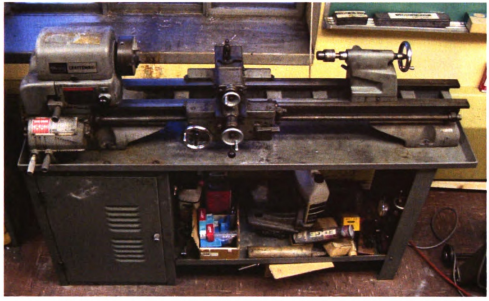

Figure A1-20. Lathe, including:

A) Lathe head

B) Lathe bit crosshead

C) Drill bit crosshead

Procedure - Determine desired amount of nail support, and decide which version of the foam lathe bit is appropriate.

- Version 1 produces a 30 mm (overall) piece of foam, with 20 mm distal to the beginning of the taper (use when more support of the nail is desired).
- Version 2 produces a 25 mm (overall) piece of foam, with 15 mm distal to the beginning of the taper (use when less nail support is desired).

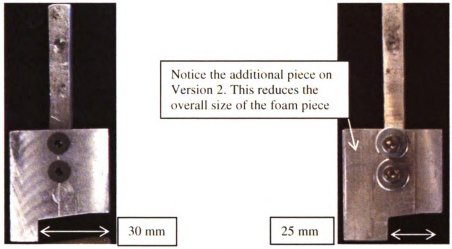

Figure A1-21. Foam lathe bit, Version 1 (left) and Version 2 (right)

Place foam lathe bit into lathe bit holder located in the lathe bit crosshead

- between the foam lathe bit and the base of the bit holder, there should be a large black washer, approximately 9/32" thick and 1 ¾" in diameter.
- use a T-square to make sure that the foam lathe bit is oriented 90 degrees to the rotating surface.
- Tighten the foam lathe bit into the bit holder using the foam lathe bit chuck.

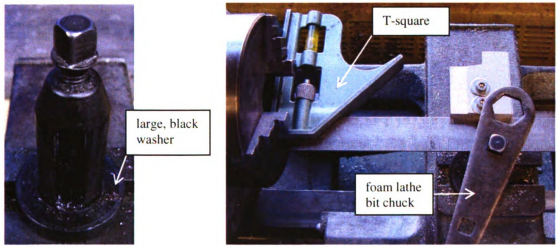

Figure A1-22. Close-up view of lathe bit holder (left) and tightening of lathe bit holder using foam lathe bit chuck. Note that using T-square while tightening will ensure proper alignment.

- Insert drill bit into drill bit crosshead (use a #3 drill bit for 6 mm nails, use a 19/64" for 8 mm nails)
- Tighten the drill bit into the bit crosshead using the drill chuck.

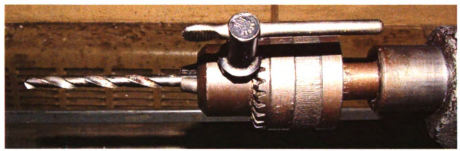

Figure A1-23. Close-up view of drill bit crosshead with drill bit and chuck shown.

Insert the foam tube into the lathe head

- align the foam tube with the rotational axis of the lathe as much as possible, this may take some adjustment and getting used to (some tubes are better than others).
- when tightening lathe grip, be sure that the teeth of the lathe head sink in the foam at least ¼" to 3/8", if not, the tube will come loose when trying to lathe.

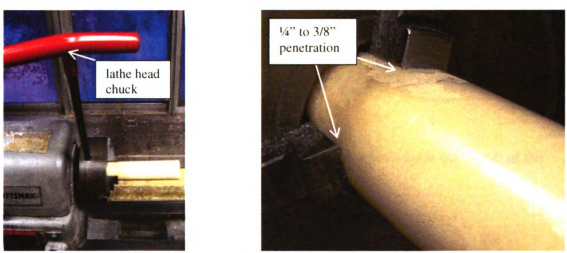

Figure A1-24. Tighten the foam tube into the lathe head using the lathe head chuck.

Begin lathing, several tips to keep in mind though:

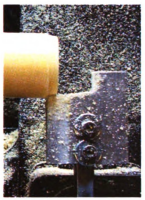

Take the first (shiny) layer of tube off by moving the lathe bit crosshead from right to left, not outside to inside (front to back).

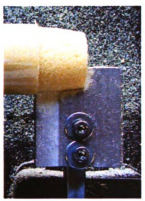

Continue moving the lathe bit crosshead from right to left until the shiny layer of the foam tube for the foam piece is removed.

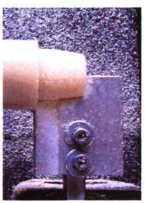

Once the shiny layer is removed, the lathe crosshead can then be moved towards the center of the tube (away from your body).

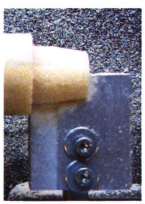

Continue to move the lathe crosshead towards the center of the tube, do this slowly!!!!

Take measurements of the tube as you reduce the diameter. When a desirable diameter is achieved (slightly > 0.25 mm), take note of the position of the crosshead indicator. This will ensure consistent foam pieces.

The drill bit crosshead can be adjusted with this lever, located on the back of the lathe.

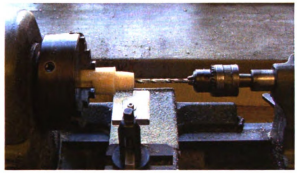

The entire drill bit crosshead is then slid along the lathe base and into the central axis of the foam, do this slowly and carefully!

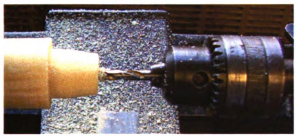

Continue to move crosshead until the entire length of the foam piece (25-30 mm) has been drilled.

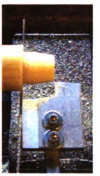

Using the handsaw, oriented with the teeth facing up, place the tip of the saw (under the foam tube) on the crosshead. In a very slow, controlled motion, lift the handle of the saw towards the foam tube.

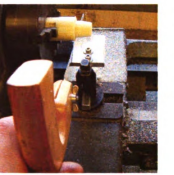

Continue lifting the handle of the handsaw towards the center of the foam tube. Continue lifting until the tube is almost cut. Be careful as the foam piece is cut from the tube.

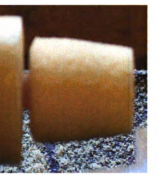

Do not grab the foam piece. It is best to allow the piece to fall.

When the foam piece is cut from the tube, there will be some residue from the tube. Just lightly run the foam piece over some sandpaper until the residue is gone.

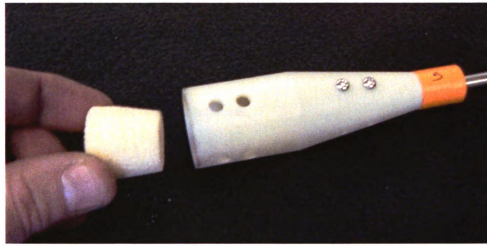

Figure A1-25. Finally, push the foam piece into the bone model

APPENDIX TWO

TESTING SOPs AND PIDs

INSTRON MACHINE GENERAL INFORMATION

Location: Orthopaedic Biomechanics Laboratories

4th floor, East Fee Hall

Technician/Operator: Cliff Beckett

A411 East Fee Hall

353-3122

- Must be present during operation.

Parts and Terms

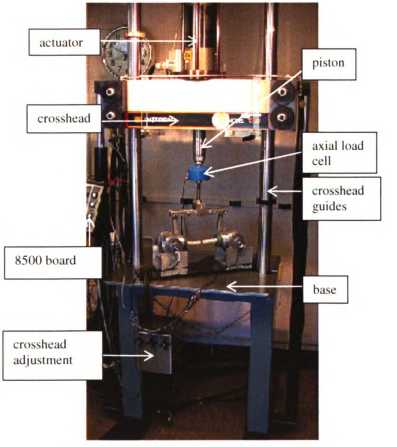

Figure A2-1. General view of Instron machine.

Actuator: consists of the working parts of the machine: the piston, the servo-hydraulic valve, and the LVDT (linear variable displacement transducer).

Piston: only part of the machine that will move during testing.

Axial Load Cell: not actually part of the Instron machine, but attached to the end of the piston. Essential to record load data. Load cells of various shapes and sizes can be fitted to the Instron Machine. *Do not over tighten when attaching load cell to piston, can damage load cell!!!!!* Usually about an inch of threaded length is adequate to securely fix the load cell to the piston.

Crosshead: the moveable base connecting the actuator to the base of the Instron machine vie the guide rails.

Guides: allow for the very top, or crosshead of the Instron machine, to be adjusted vertically. *An orange clamp has been put on the top of the left guide to prevent the head from going to far up and hitting the ceiling, be cautious of this!!!!!*

Crosshead Adjustment: controls crosshead height. There are three handles from left to right they are: raise, lower and clamp. The hydraulics must be on to move the crosshead; the on button is located on the 8500 board attached to the Instron. The clamp handle needs to be loosened first to allow any further adjustment. After the clamp handle is loosened, loosening of either the raise of lower handle will result in motion of the crosshead in that direction. The speed at which the crosshead moves is proportional to how much the raise or lower handles are loosened.

Base: all fixtures will be mounted to the base of the Instron in some way shape or form.

8500 Board: triggers and controls all data acquisition by the computers. The 8500 board will be further discussed in the data acquisition section of the SOP.

Data Acquisition

Computers

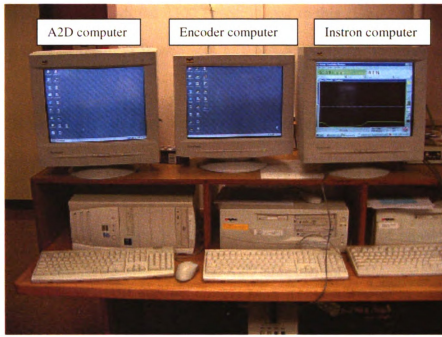

Figure A2-2. A2D, Encoder, and Instron monitors and computers.

8500 Board

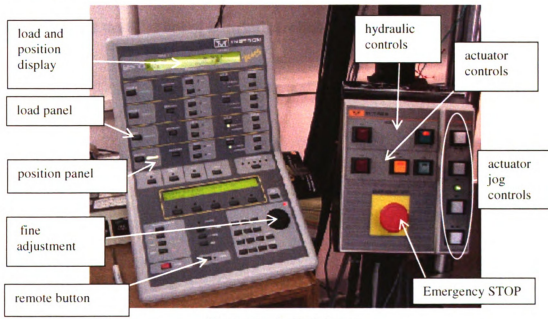

Figure A2-3. 8500 Board.

Instron Computer: used for all tests. All programming is done on this computer, instead of the 8500 board, making them easier to modify and edit. All the data from the Instron machine, which goes through the 8500 board, is sent to this computer and stored as a *.csv file, a copy of this data is also sent to the A2D computer for interpretation into digital data.

Encoder Computer: this computer is only used for tests that involve additional encoders, such as the bending tests, which collect data from two rotary encoders. The program Labview is installed on this computer, it allows us to tell the computer to start recording data when triggered. The trigger is usually set to be the first bit of movement by the piston. A copy of this data is also sent to the A2D computer for further interpretation.

A2D Computer: this computer takes the analog data that it receives from both the Instron computer and the Encoder computer and converts it into digital format. This computer is also equipped with Labview and must be run simultaneously with the Encoder computer.

Detailed use of the 8500 board is included within each test procedure.

TORSION TEST SOP

Test

Sine wave (load control)-------*controlled by135 N*m torque load cell,*

previously *controlled by 2500 lb axial load cell*

0 N*m preload to ± 5 N*m.

10 cycles @ 8 seconds a cycle (0.125 Hz)

PIDS

Load and position PIDs are construct dependent, see Testing PIDs

Data

- Torque is recorded via the torque load cell

- Actuator displacement measured by the LVDT is recorded (converted to angular displacement in the excel macro).

- Angular displacement is recorded via the rotary encoder

Materials

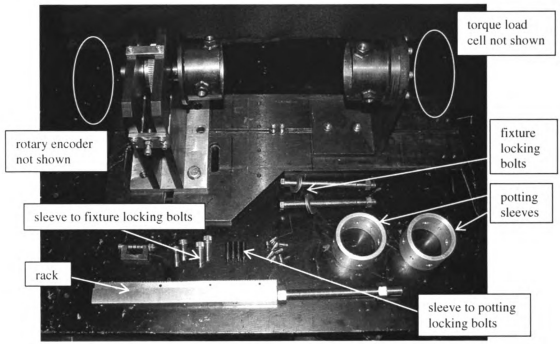

Figure A2-4. Torsion fixture and required materials.

Setup

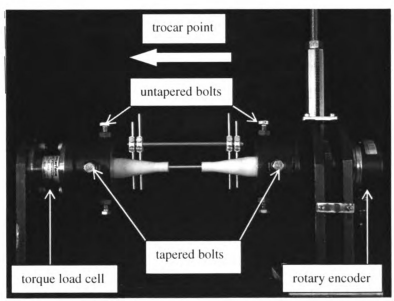

Figure A2-5. View of construct within torsion fixture.

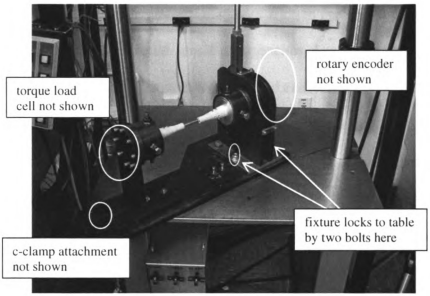

Figure A2-6. View of torsion fixture within Instron machine.

Torsion Test Background Information

The torsion tests are intended to simulate a torque of 5 N*m being applied. The amount of torque being generated is completely proportional to the size of the moment arm where the load is being applied. The current torsion fixture is equipped with a gear of radius 0.0381 m. To achieve the desired torque of 5 N*m, a 131.2 N load must be applied by the piston. This was calculated by:

$$(0.0381 \text{ m})*(131.2 \text{ N}) = (5 \text{ N*m})$$

Prior to using the torque load cell, the axial load cell was programmed to ± 131.2 N.

Procedure

Attaching the torsion fixture to the base of the Instron machine - The primary concern when mounting the fixture is to ensure that there is no friction or contact between the rack and the walls of the fixture itself. To do this, the axial load cell must first be calibrated with the rack of the fixture attached. This is a very important step in recording

accurate data. If this is not done, large amounts of friction can develop between the rack and the torsion fixture. This could result in erroneous data or damage to the Instron machine. So, attach the rack to the axial load cell and calibrate by pressing the "calibrate" button on the load panel of the 8500 board, then select "cal", then "auto", the screen will ask you to ensure that the transducer is at zero, double check, then select "go". The calibrate button will rapidly blink will it is calibrating itself, you will see it go to its maximum values and then it will zero itself. The load cell is now calibrated to take into account the rack of the torsion fixture when the red light stops blinking.

With the rack attached to the calibrated load cell, jog the actuator to its highest position, or high enough to allow the rack to fit between the walls of the torsion fixture. Crosshead adjustment may be necessary, if so, adjustment of the crosshead position is controlled by the 3 black knobs on the silver box under the Instron table on the left side. The "clamp" knob must be loosened (turn counter clockwise) first, then the "lower" knob must be slowly loosened to adjust the crosshead positioning to an appropriate height (notice that the speed of the crosshead position adjustment depends on how much you turn the "clamp" and "lower" knobs, GO SLOW, BE SAFE. DO NOT forget to tighten (turn clockwise) the "clamp" and "lower" knobs before doing anything else, notice though that these knobs do not need to be tightened extremely tight, be snug but don't overdo it.

With the rack hanging from the axial load cell, move the actuator up and down and look for points where the axial load increases rapidly. Ultimately, you should be able to have less than a couple of Newton felt by the load cell throughout the entire stroke of the Instron. Once this is achieved, the base of the torsion fixture is then mounted tot eh

base of the Instron machine. The fixture is mounted to the Instron machine by two bolts and a c-clamp. These two bolts are referred to as the fixture locking bolts.

Preparing the specimen - After mounting the specimen in the potting cups, it can then be mounted into the potting sleeves. Using eight sleeve-to-potting locking bolts, lock the potting into the sleeve. Be sure to orient the potting sleeves as indicated on the sleeve (arrows should point away from the middle of the specimen towards the fixture mounts). Edge of potting and sleeve will be flush if properly placed.

Mounting the specimen - The potting sleeves are then inserted into the torsion fixture. Sleeve to fixture locking bolts secure its position.

- The sleeve-to-fixture bolts are different. There are 8 total, 4 with tapered ends for locking, 4 with blunt ends for removing slack between the potting sleeves and the torsion fixture cups.
- The tapered end bolts must be placed in the holes on the fixture, which are 1 in. from the edge. This will allow proper alignment of the specimen and the fixture.

Tighten all bolts until the potting sleeves are stable within the torsion cups

Calibrating torque load cell - The torque applied to the specimen is measured with a torque load cell. The calibration of the torque load cell must be done with Cliff Beckett present. The PIDs given in the Testing PIDs section are given for the axial load cell and are different from those implemented when using the torque load cell.

Adjusting actuator position - When running torsion tests, the goal is to start at a point when no torque is applied to the specimen. This is done by adjusting the actuator position until the reading of the torque load cell is zero (or very close). So, to zero the torque on the specimens prior to beginning the test, first go into high pressure by pressing the

"high" button on the 8500 board. You will then manually adjust the position control on the 8500 board until a torque reading close to zero is achieved. The Instron machine can now be placed into load control. It is important to realize that once the machine is in load control, position is no longer a factor, the machine now will move in whatever direction it needs to, to achieve a desired load (*in other words, BE CAREFUL, load control is dangerous!*).

Running the program - The torsion test (torqsin.blk) program is located in the C:/Wavemaker/Lansdown directory. After the load is set to zero by adjusting the position set point, double check that you are in "high" pressure, and begin the test.

After the test - After the test is run, be sure to switch the Instron machine back into position control.

BENDING TEST SOP

Test

Sine wave (load control)------- *controlled by 2500 lb axial load cell*

0 N preload to ± 151.7 N. (equivalent to moment of 3.5 N*m, based on specimen length)

10 cycles @ 8 seconds a cycle (0.125 Hz)

PIDs

Load and position PIDs are construct dependent, see Testing PIDs (calibrated for use of 2500 lb axial load cell)

Data

- Load on the axial load cell is recorded.

- Actuator displacement measured by the LVDT is recorded.

- Angular displacement measured by the 2 rotary encoders is recorded

Materials

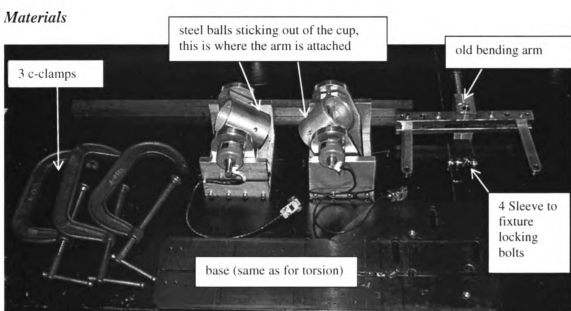

Figure A2-7. Bending fixture and required materials.

Setup

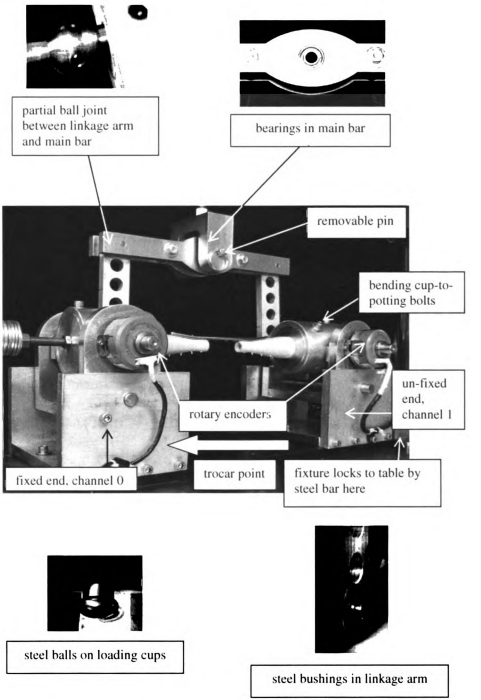

Figure A2-8. View of construct within bending fixture.

Bending Test Background Information

The bending tests are intended to simulate a moment of 3.5 N*m being applied to the specimen. The moment being generated is completely proportional to the size of the design of the individual bending cup fixtures. Because four-point bending is the desired tests, the generation of a 3.5 N*m moment under four-point bending must be considered. The current bending fixture is equipped with two individual bending cups, each of these cups is allowed to rotate in one plane. This axis of rotational is approximately 0.04629 m away from the point of applied load (the steel balls). Based on these dimensions, a load of 75. 6 N must be applied to each bending cup to achieve a desired load of 3.5 N*m. Because the fixture is designed to transfer one axial load through the main bar into two equal loads on each linkage arm, an axial load of 151.2 N is equivalent to creating a 3.5 N*m pure bending moment on the specimen. This is calculated by:

$$(75.6\ \text{N})*(0.04629\ \text{m}) = (3.5\ \text{N*m})$$

Once again, this bending moment is applied to both sides of the bending fixture; therefore the bendsine program is designed to achieve a maximum axial load of 151.2 N.

Procedure

Attaching the bending cups to the base of the bending fixture - The first step is to attach the two bending cups to the base of the fixture. Be sure to attach the fixed cup (ch. 0) on the left and the free cup (ch. 1) on the right. The cups do not need to be locked to the base yet.

Aligning and connecting the bending fixture and the Instron machine - Prior to aligning the cups, a loosely placed specimen should be put into the bending cups, making

sure the surface of the potting is flush with the surface of the bending cups. The main bar is attached to the Instron actuator via a removable pin. Once the main bar of the bending fixture is attached to the Instron, the next step is to lower the crossheads of the Instron machine and to lower the actuator position so that the linkage arm steel bushings line up with the steel balls of the bending cups. In order to achieve this, the two individual bases of the bending cups must be perfectly aligned with one another.

Putting a specimen into the cups, then rotating the cups until all of their surfaces are parallel or perpendicular to one another, does this. Adjustment of the crosshead position is controlled by the 3 black knobs on the silver box under the Instron table on the left side. The "clamp" knob must be loosened (turn counter clockwise) first, then the "lower" knob must be slowly loosened to adjust the crosshead positioning to an appropriate height (notice that the speed of the crosshead position adjustment depends on how much you turn the "clamp" and "lower" knobs, GO SLOW, BE SAFE. DO NOT forget to tighten (turn clockwise) the "clamp" and "lower" knobs before doing anything else, notice though that these knobs do not need to be tightened extremely tight, be snug but don't overdo it.

Once the vertical position of the crosshead is determined, the base of the bending fixture must be adjusted to properly align it with the main bar of the fixture. This is done by rotating the base of the fixture until two things are possible, one is to lower the actuator and see that the two linkage points are aligned with the steel balls (from an overhead view), and there must also be room for the steel bar that attached the base of the bending fixture to the base of the Instron machine. Once desired alignment is achieved,

the base of the bending fixture may be attached to the base of the Instron machine via two c-clamps and a steel bar on the right side, and a c-clamp by itself on the left side.

Calibrating the axial load cell - The final step prior to mounting the specimen into the fixture is to calibrate the load cell taking into account the weight of the main bar and two linkage arms. Load cell should be calibrated with the entire bending arm hanging from it, but not attached to the fixture (very important step in recording accurate data). If this is not done then the load cell will consider the weight of the main bar and linkage arms (not good!). So, attach the main bar, with the two linkage arms, to the actuator and calibrate the load cell. Load cell calibration is done by pressing the "calibrate" button on the load panel of the 8500 board, then select "cal", then "auto", the screen will ask you to ensure that the transducer is at zero, double check, then select "go". The calibrate button will rapidly blink will it is calibrating itself, you will see it go to its maximum values and then it will zero itself. The load cell is calibrated to take into account the main bar and linkage arms when the red light stops blinking. You are now ready to mount the specimen into the fixture.

Mounting the specimen - The potting can be inserted directly into the bending fixture cups. If slack is present before a construct is placed into the bending fixture, than check to make sure it is still present after the specimen is mounted and secured by the cup to potting locking bolts. Each cup should have two screws on the top only, bottom screws are not necessary. If a specimen loses its slack when placed into the bending cups, then the specimen is out of alignment. If this occurs, simply loosen the attachment screws and rotate the specimen/potting until the actual slack is present again. In these cases, the

potting must be reattached to the bending cups via screws that do not have shoulders (any standard screw).

Setting PID levels - Before or after opening the program you have to adjust the PID levels. This is done manually on the Instron 8500 by pressing the calibrate button on the load panel, then loop and then enter the appropriate numbers.

Adjusting actuator position - When running bending tests, the goal is to start at a point when no load is applied to the specimen. This is done by adjusting the actuator position until the reading of the axial load cell is zero (or very close). Remember that the weight of the main bar and linkage arm has already by neglected by calibrating the load cell with them attached. So, to zero the load on the specimens prior to beginning the test, first go into high pressure by pressing the "high" button on the 8500 board. You will then manually adjust the position control on the 8500 board until a load reading close to zero is achieved. The Instron machine can be placed into load control. It is important to realize that once the machine is in load control, position is no longer a factor, the machine now will move in whatever direction it needs to, to achieve a desired load (BE CAREFUL, load control is dangerous!).

Running the program - The bending test (bendsin.blk) program is located in the C:/Wavemaker/Lansdown directory. After the load is set to zero by adjusting the position set point, double check that you are in "high" pressure, and begin the test.

After the test - After the test is run, be sure to switch the Instron machine back into position control.

COMPRESSION TEST SOP

Test

Sine wave (load control)------- *controlled by 2500 lb axial load cell*

–5 N preload to –176 N. (construct is never in tension)

10 cycles @ 1 second a cycle (1 Hz)

data sampling is 500 Hz for 10.5 seconds

PIDs

Load and position PIDs are construct dependent, see Testing PIDs

The load vs. time sine wave should be used to determine if proper load PID levels are being used. Pay attention to the following:

- The most important thing is to analyze the wave to look for areas where it appears that the Instron machine may go unstable; this is usually characterized by a sharp jump in load over a very short period of time. (it looks like a spike in the sine wave, but it may not be very obvious). ***The Instron machine going unstable is the most dangerous thing that can happen during testing, if your PID levels are not carefully managed, severe damage and injury may occur.***
- Check maximum and minimum peak values and make sure that the Instron machine is not overshooting or undershooting the desired load levels of –5 N and –176 N. **(Do not be satisfied with peak values until you are at least ± 2 N of your desired load)**
- You must also analyze the peaks and check for flat spots (where a constant load is held over some length of time)

The relationship between the PIDs and the characteristics of the load vs. time wave are based on the construct being tested and the speed of the test. Contributing factors to these variations are: slack in the system, extreme compliance or stiffness, and overall expected range of motion.

Data

- Load on the actuator load cell is recorded.
- Actuator displacement measured by the Instron LVDT is recorded.

Materials

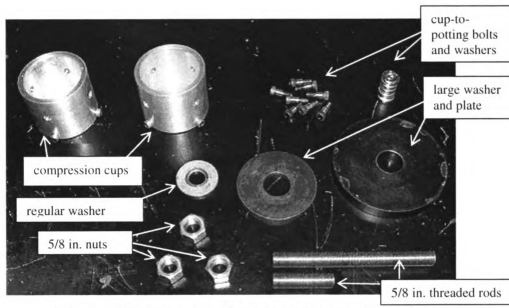

Figure A2-9. Compression fixture and required materials.

Setup

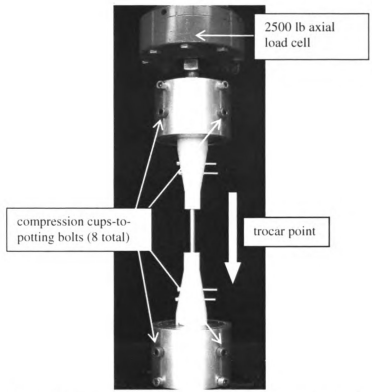

Figure A2-10. View of construct within compression fixture attached to Instron machine.

Procedure

Attaching the compression cups **-** The first step is to securely attach the top cup to the load cell. This attachment should consist of two 5/8"-18 nuts and a 5/8"-18 threaded rod, with about a ½" between the two nuts. After the top cup is attached, the bottom cup may then be attached, but not securely. Attachment of the bottom cup consists of the large plate (4" dia, ½" thick), the large washer (3" dia, 1/8" thick), a regular washer (1" dia, 1/16" thick), a 5/8"-18, nut and a 5/8"-18 threaded rod. Remember; do not secure the bottom cup yet.

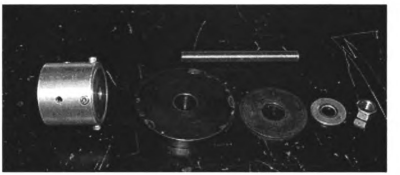

Figure A2-11. Order of materials for bottom cup.

Aligning the cups - The next step is to lower the crossheads of the Instron machine and to lower the actuator position itself so that the two cups are allowed to nearly contact each other (1 mm apart). Adjustment of the crosshead position is controlled by the 3 black knobs on the silver box under the Instron table on the left side. The "clamp" knob must be loosened (turn counter clockwise) first, then the "lower" knob must be slowly loosened to adjust the crosshead positioning to an appropriate height (notice that the speed of the crosshead position adjustment depends on how much you turn the "clamp" and "lower" knobs, GO SLOW, BE SAFE). Be careful not to try to get the two compression cups too close with the crosshead control (knobs), this is just a rough position adjustment. DO NOT forget to tighten (turn clockwise) the "clamp" and "lower" knobs before doing anything else, notice though that these knobs do not need to be tightened extremely tight, be snug but don't overdo it.

The next step is to lower the actuator position for a more precise adjustment. This is done by the "jog" buttons on the Instron 8500 board. You will notice that once the "clamp" knob is loosened, the "actuator" light on the 8500 board turns to off, this a safety precaution. Before you have any control of the actuator, you must put the machine into "low" pressure on the 8500 board. While in low pressure, the actuator can be adjusted by

the "jog" buttons. This should be done slowly to avoid any accidental contact between the two cups. When the two cups are within range (approximately 1 mm apart), move the bottom cup accordingly so that they both line up perfectly axial. ALIGNMENT IS CRUCIAL to the compression tests!

Securing the cups - Once perfect alignment is reached, the bottom cup can then be secured. Be sure to take note of the position of the locking holes in the bottom potting cup, (two holes should be visible; this is the only configuration which allows the specimen to be placed correctly, with the bolts facing to the right). Don't worry about the hole positioning of the top cup, this can be rotated later by turning the actuator shaft manually.

Once you are satisfied with the cup positioning with respect to each other, the crossheads can then be raised to an appropriate height to fit the specimen. Raising the actuator and crosshead is done in the same way as lowering it, except that after the "clamp" knob is loosened, the "raise" knob is used now. DON'T FORGET to tighten both of them when the desired position is reached.

Calibrating the load cell - The final step prior to loading the specimen into the fixture is to calibrate the load cell taking into account the weight of the top compression cup and its attachments. This is a very important step in recording accurate data. If this is not done then the load cell will consider the weight of the top cup and its attachments to be a tensile load, this is not good!

Calibrating the load cell with the top cup is done by pressing the "calibrate" button on the load panel of the 8500 board, then select "cal", then "auto", the screen will ask you to ensure that the transducer is at zero, then select "go". The calibrate button will

rapidly blink will it is calibrating itself, you will see it go to its maximum values and then it will zero itself. The load cell is calibrated to take into account the top potting cup when the red light stops blinking. You are now ready to mount the specimen into the fixture.

Mounting the specimen - It is very important that the compression fixture is properly set up, if the cups aren't aligned on there axis, loading the specimen will be nearly impossible, and erroneous data will result. When the crosshead positioning is done, it is important that you allow enough room between the two cups for the entire length of the potted specimen. The specimen is to be consistently mounted with the trocar point of the nail facing down and the bolts/screws pointing to the right. First slide the bottom potting partially into the compression cup, then slowly lower the actuator position with the "jog" buttons until the mounted specimen is restricted to only move vertically on the same axis as the two compression cups.

Securing the specimen - Once all three (the two cups and the specimen) are aligned axially, the actuator can be lowered further until the locking bolts can be inserted through the compression cups and into the potting. Take careful notice that you are not loading you specimen while placing the bolts, loads can go unnoticed do to the minimal displacement under compressive loads and this can make it difficult to place the locking bolts, they should go in freely, without much force. Depending on the length of the locking bolts, washers may or may not be used. Once all eight of the bolts are secured, the specimen is mounted.

Setting PID levels - Before or after opening the program you have to adjust the PID levels accordingly. This is done manually on the Instron 8500 by pressing the calibrate button on the load panel, then loop and then enter the appropriate numbers.

Preloading the specimen - The last step before running a compression test is to preload the specimen. First go into high pressure by pressing the "high" button on the 8500 board. Then manually adjust the position control on the 8500 board until a load reading close to zero is achieved. Instron machine can now be placed into load control. Remember that once the machine is in load control, position is no longer a factor, the machine now will move in whatever direction it needs to, to achieve a desired load (BE CAREFUL!). Under position control you may now select a desired set point, the screen will prompt you to give a load value, enter -5 N (hit 5 first, then the – sign), then hit enter. You should now see a reading close to -5 N on the 8500 board, this is your compressive preload.

Running the program - The compsine (compsin.blk) program is located in the :/C/Wavemaker/Lansdown directory. Double check that you are in "high" pressure, then run the program according to the Wavemaker program instructions.

After the test - After the test is run, be sure to switch the Instron machine back into position control.

TESTING PIDs

Torsion

Specimen type: **ILN6s** (short & long)
Description: 6 X 185 mm nail, 4-2.7 mm bi-cortical screws, 5 & 12 cm osteotomy
Load PID: -2, 0, 0, 0
Position PID: 13, 1, 0, 1

Specimen type: **ILN6b** (short & long)
Description: 6 X 185 mm nail, 4-2.7 mm bi-cortical bolts, 5 & 12 cm osteotomy
Load PID: -2, 0, 0, 0
Position PID: 13, 1, 0, 1

Specimen type: **ILN8S** (short & long)
Description: 8 X 185 mm nail, 4-3.5 mm bi-cortical screws, 5 & 12 cm osteotomy
Load PID: -2, 0, 0, 0
Position PID: 13, 1, 0, 1

Specimen type: **ILN8B** (short and long)
Description: 8 X 185 mm nail, 4-3.5 mm bi-cortical bolts, 5 & 12 cm osteotomy
Load PID: -2, 0, 0, 0
Position PID: 13, 1, 0, 1

Specimen type: **ILNn** (short and long)
Description: 8-6 X 185 mm novel nail, with 4-SCP locking devices, 5 & 12 cm osteotomy
Load PID: -2, 0, 0, 0
Position PID: 13, 1, 0, 1

Specimen type: **br-DCP** (short and long)
Description: broad DCP with 8-3.5 mm bicortical screws, 5 & 12 cm osteotomy
Load PID: -2, 0, 0, 0
Position PID: 13, 1, 0, 1

Specimen type: **ILN-ESF**
Description: 6 X 185 mm nail, with 4 hybrid 2.7 mm ILN bolt/3.2 mm ESF pins and 1 small SK™ titanium connecting bar (6.3 mm [diameter] by 150 mm [length])
Load PID: -2, 0, 0, 0
Position PID: 13, 1, 0, 1

Mediolateral and Craniocaudal Bending

Specimen type: **ILN6s** (short & long)
Description: 6 X 185 mm nail, 4-2.7 mm bi-cortical screws, 5 & 12 cm osteotomy
Load PID: 10, 0, 2, 0
Position PID: 13, 1, 0, 1

Specimen type: **ILN6b** (short & long)
Description: 6 X 185 mm nail, 4-2.7 mm bi-cortical bolts, 5 & 12 cm osteotomy
Load PID: 10, 0, 2, 0
Position PID: 13, 1, 0, 1

Specimen type: **ILN8S** (short & long)
Description: 8 X 185 mm nail, 4-3.5 mm bi-cortical screws,5 & 12 cm osteotomy
Load PID: 10, 0, 2, 0
Position PID: 13, 1, 0, 1

Specimen type: **ILN8B** (short & long)
Description: 8 X 185 mm nail, 4-3.5 mm bi-cortical bolts, 5 & 12 cm osteotomy
Load PID: 10, 0, 2, 0
Position PID: 13, 1, 0, 1

Specimen type: **ILNn** (short & long)
Description: 8-6 X 185 mm novel nail, with 4-SCP locking devices, 5 & 12 cm osteotomy
Load PID: 6, 0, 2, 10
Position PID: 13, 1, 0, 1

Specimen type: **br-DCP** (short & long)
Description: broad DCP with 8-3.5 mm bicortical screws, 5 & 12 cm osteotomy
Load PID: 6, 0, 2, 10
Position PID: 13, 1, 0, 1

Specimen type: **ILN-ESF**
Description: 6 X 185 mm nail, with 4 hybrid 2.7 mm ILN bolt/3.2 mm ESF pins and 1 small SK™ titanium connecting bar (6.3 mm [diameter] by 150 mm [length])
Load PID: 6, 1, 2, 10
Position PID: 13, 1, 0, 1

Compression

Specimen type: **ILN6s** (short & long)
Description: 6 X 185 mm nail, 4-2.7 mm bi-cortical screws, 5 & 12 cm osteotomy
Load PID: 0, 1, 2, 3
Position PID: 13, 1, 0, 1

Specimen type: **ILN6b** (short & long)
Description: 6 X 185 mm nail, 4-2.7 mm bi-cortical bolts, 5 & 12 cm osteotomy
Load PID: 0, 1, 2, 3
Position PID: 13, 1, 0, 1

Specimen type: **ILN8S** (short & long)
Description: 8 X 185 mm nail, 4-3.5 mm bi-cortical screws,5 & 12 cm osteotomy
Load PID: 0, 1, 2, 3
Position PID: 13, 1, 0, 1

Specimen type: **ILN8B** (short & long)
Description: 8 X 185 mm nail, 4-3.5 mm bi-cortical bolts, 5 & 12 cm osteotomy
Load PID: 0, 1, 2, 3
Position PID: 13, 1, 0, 1

Specimen type: **ILNn** (short & long)
Description: 8-6 X 185 mm novel nail, with 4-SCP locking devices, 5 & 12 cm osteotomy
Load PID: 0, 1, 2, 1
Position PID: 13, 1, 0, 1

Specimen type: **br-DCP** (short & long)
Description: broad DCP with 8-3.5 mm bicortical screws, 5 & 12 cm osteotomy
Load PID: 0, 1, 2, 1
Position PID: 13, 1, 0, 1

Specimen type: **ILN-ESF**
Description: 6 X 185 mm nail, with 4 hybrid 2.7 mm ILN bolt/3.2 mm ESF pins and 1 small SK™ titanium connecting bar (6.3 mm [diameter] by 150 mm [length])
Load PID: 0, 1, 2, 1
Position PID: 13, 1, 0, 1

APPENDIX THREE

THEORETICAL ANALYSIS

CHAPTER ONE

Strain Readout

$$\varepsilon_s = (R_g)/[F_g*(R_g + R_s)] \qquad \text{[A3-1]}$$

Equation A3-1. Shunt calibration strain readout, where:

ε_s : strain readout with shunt cal.

R_g : strain gage resistance (350 Ohms)

F_g : gage factor (2.12 ± 1.0%)

R_s : shunt cal. resistance (30060 Ohms)

Longitudinal Strain Derivation/Calculation

$$\varepsilon_x = - y/\rho \qquad \text{[A3-2]}$$

Equation A3-2. Longitudinal strain as a function of radius of curvature and distance from neutral axis, where:

ε_x : longitudinal strain

y : distance from the neutral axis to the point of interest

ρ : radius of curvature

Since both plates are bent to the same degree, their curvatures are equal, reducing Eq. [B] to:

$$(\varepsilon_{HP}/y_{HP}) = (\varepsilon_{LC\text{-}DCP}/y_{LC\text{-}DCP})$$

Hooke's Law

$$\sigma = E*\varepsilon \qquad \text{[A3-3]}$$

Equation A3-3. Hooke's Law, where:

σ : elastic stress

E : modulus of elasticity

ε : elastic strain

Flexural Formula

$$S = -(M*y)/I \qquad \text{[A3-4]}$$

Equation A3-4. Flexural formula, where:

σ : bending stress

M : moment at the point of interest

y : distance form the neutral axis to the point of interest

I : area moment of inertia of the cross section at the point of interest

Area Moment of Inertia (AMI)

The AMI is a geometrical property (Equation E) [17], which is related to the amount of material in a given region, therefore, the AMI is higher in the solid portion of the plate than it is in the region where a hole is present.

$$I_x = \int y^2 dA \qquad I_y = \int x^2 dA \qquad \text{[A3-5]}$$

Equation A3-5. Area moment of inertia (AMI), where:

I_x, I_y: AMI with respect to x and y-axis, respectively

y, x: equation of the line forming the boundary of the cross section

A: area of the cross section

AMI and Strain

$$\varepsilon = \sigma/E = (M*y*E)/I \qquad \text{[A3-6]}$$

Equation A3-6. Showing the inverse relationship between AMI and strain.

CHAPTER THREE

Matlab Programming for AMI Calculation

*note: % sign denotes a non-command line and is typically a brief description of the function performed by following command

Screw, Bolt, and SCP AMI Calculation (ScrewBoltSCP_AMIcalc.m)

```
clear
clc
global x
%User input Diameter of screw or peg at nail hole level
CD=input('Enter cis core diameter:');
%User input Diameter of screw or peg at nail hole level
TD=input('Enter trans core diameter:');
if CD==TD
    AMI=((pi)*(CD/2)^4)/4
end
if CD>TD
    ThreadedSection_AMI=((pi)*(CD/2)^4)/4
    MidTaperedSection_AMI=((pi)*(((CD+TD)/2)/2)^4)/4
    SolidSectionAMI=((pi)*(TD/2)^4)/4
end
if CD<TD
    'ERROR!!!!!    Cis diameter must be greater than Trans diameter'
end
```

Plate AMI Calculation (Plate_AMIcalc.m)

```
clear
clc
global x
%User input width of plate at screw hole level
PW=input('Enter width of plate at screw hole level:');
%User input thickness of plate at screw hole level
PT=input('Enter thickness of plate at screw hole level:');
%User input screw hole diameter at nail hole level
HD=input('Enter diameter of screw hole:');
'At nail hole level'
MedioLateral_AMI=((1/12)*(PW)*(PT^3))-((1/12)*(HD)*(PT^3))
CranioCaudal_AMI=((1/12)*(PT)*(PW^3))-((1/12)*(PT)*(HD^3))
'At solid section'
MedioLateral_AMI=((1/12)*(PW)*(PT^3))
CranioCaudal_AMI=((1/12)*(PT)*(PW^3))
if PT>PW
    'ERROR!!!!!    Plate width must be greater than plate thickness'
end
if HD>PW
    'ERROR!!!!!    Plate width must be greater than screw hole
diameter'
end
```

ILN AMI Calculation (FinalAMIcalc.m)

```
clear
clc
global x
%User input Diameter of ILN at nail hole level
D=input('Enter ILN diameter at nail hole level:');
%User input Diameter of ILN at solid level
DS=input('Enter Solid ILN Diameter:');
%User input Cis Cortex Hole Diameter
CC=input('Enter Cis Hole diameter:');
%User input Trans Cortex Hole Diamter
TC=input('Enter Trans Hole diameter:');
%Calculate the length of the rectangle and triangle
if CC>TC
StraightLength=[(D^2)/4-(CC^2)/4]^(1/2)+[(D^2)/4-(TC^2)/4]^(1/2);
%Calculate the width of the triangle
TriangleWidth=(CC/2-TC/2);
%Calculate the width of the rectangle
RectangleWidth=(TC/2);
%Calculate the height of the top Semi-Circle
ycis=(((D^2)/4)-((CC^2)/4))^(1/2);
%Calculate the height of the bottom Semi-Circle
ytrans=(((D^2)/4)-((TC^2)/4))^(1/2);
%Calculate the Area of the Top Semi-Circle
TopTheta=2*[asin((CC/2)/(D/2))];
AreaTopSlice=(TopTheta/2)*(D^2)/4;
AreaTopTriangle=((D/2)*(cos(TopTheta/2)))*(CC/2);
AreaTopCircle=AreaTopSlice-AreaTopTriangle;
%Calculate the Area of the Bottom Semi-Circle
BotTheta=2*[asin((TC/2)/(D/2))];
AreaBotSlice=(BotTheta/2)*(D^2)/4;
AreaBotTriangle=((D/2)*(cos(BotTheta/2)))*(TC/2);
AreaBotCircle=AreaBotSlice-AreaBotTriangle;
%Calculate the Area of the Half Circle
AreaHalfCircle=pi*(D^2)/8;
%Calculate the Area of the Triangle
AreaTriangle=(StraightLength)*(TriangleWidth)/2;
%Calculate the Area of the Rectangle
AreaRectangle=(StraightLength)*(RectangleWidth);
%Calculate the Total Area of half of the Cross Section
AreaTotal=AreaHalfCircle-
(AreaTopCircle/2+AreaBotCircle/2+AreaTriangle+AreaRectangle);
%Calculate the centroid of the top Semi-Circle (origin is taken as
bottom
%of cross section, not center)
CentroidTopCircle=(D/2)+((((D^2)*CC)/8)-(((ycis^2)*CC)/2)-
((CC^3)/24))/AreaTopCircle;
%Calculate the centroid of the bottom Semi-Circle (origin is bottom of
%cross section, not center)
CentroidBotCircle=(D/2)+(-
(((D^2)*TC)/8)+(((ytrans^2)*TC)/2)+((TC^3)/24))/AreaBotCircle;
%Calculate the centroid of the half circle
CentroidHalfCircle=D/2;
%Calculate the centroid of the triangle
CentroidTriangle=(D/2-ytrans)+(StraightLength)*(2/3);
```

```
%Calculate the centroid of the rectangle
CentroidRectangle=(D/2-ytrans)+(StraightLength/2);
%Calculate the centroid of the entire cross section
SumIndividual=(AreaHalfCircle*CentroidHalfCircle)-
((AreaTopCircle/2)*(CentroidTopCircle)+(AreaBotCircle/2)*(CentroidBotCi
rcle)+(AreaRectangle*CentroidRectangle)+(AreaTriangle*CentroidTriangle)
);
CentroidTotal=(SumIndividual/AreaTotal);
%Calculate "d" used in parallel axis theorem (distance from centroid to
NA)
d=D/2-(SumIndividual/AreaTotal);
%Calculate the slope of the line in Mediolateral Bending
m_medio=(-ycis-ytrans)/(-TC/2+CC/2);
%Calculate the y-intercept of the line in Mediolateral Bending
b_medio=ycis+(m_medio*CC/2);
%Equation of the line in Mediolateral Bending
y=(m_medio)*x+(b_medio);
% Define lower limit of x integral
xmin=-D/2;
% Define upper limit of x integral
xmax=-CC/2;
% Calculate ami
ami1=1/6*xmax*(xmin^2-xmax^2)^(3/2)+1/4*xmin^2*xmax*(xmin^2-
xmax^2)^(1/2)+1/4*xmin^4*atan(xmax/(xmin^2-xmax^2)^(1/2))-
1/8*i*xmin^4*log(-i*xmin/(-2*xmin)^(1/2))+1/8*i*xmin^4*log(i*xmin/(-
2*xmin)^(1/2));
% Define lower limit of x integral
xmin2=-CC/2;
% Define upper limit of x integral
xmax2=-TC/2;
% Calculate ami2
ami2=1/12*m_medio^3*xmax2^4+1/3*m_medio^2*xmax2^3*b_medio+1/2*m_medio*x
max2^2*b_medio^2+1/3*xmax2*b_medio^3+1/96*xmax2*(D^2-
4*xmax2^2)^(3/2)+1/64*D^2*xmax2*(D^2-
4*xmax2^2)^(1/2)+1/128*D^4*atan(2*xmax2/(D^2-4*xmax2^2)^(1/2))-
1/12*m_medio^3*xmin2^4-1/3*m_medio^2*b_medio*xmin2^3-
1/2*m_medio*b_medio^2*xmin2^2-1/3*b_medio^3*xmin2-1/96*xmin2*(D^2-
4*xmin2^2)^(3/2)-1/64*D^2*xmin2*(D^2-4*xmin2^2)^(1/2)-
1/128*D^4*atan(2*xmin2/(D^2-4*xmin2^2)^(1/2));
% Calculate final integral
final=ami1+ami2;
%Compute Mediolateral AMI with parallel axis theorem taken into
consideration
MedioLateral_AMI=2*(final)-(2*AreaTotal)*(d^2)

%Calculate the slope of the line in CranioCaudal Bending
m_cranio=(TC/2-CC/2)/(ycis+ytrans);

%Calculate the y-intercept of the line in CranioCaudal Bending
b_cranio=CC/2-(m_cranio*-ytrans);
%Equation of the line in Mediolateral Bending

y=(m_cranio)*x-(b_cranio);
ymin=(m_medio)*x+(b_medio);
ymax=((D/2)^2-x^2)^0.5;
```

```
CranioCaudal_AMI=2*(1/96*ytrans*(D^2-
4*ytrans^2)^(3/2)+1/64*D^2*ytrans*(D^2-
4*ytrans^2)^(1/2)+1/128*D^4*atan(2*ytrans/(D^2-4*ytrans^2)^(1/2))-
1/12*m_cranio^3*ytrans^4-1/3*m_cranio^2*ytrans^3*b_cranio-
1/2*m_cranio*ytrans^2*b_cranio^2-1/3*ytrans*b_cranio^3+1/96*ycis*(D^2-
4*ycis^2)^(3/2)+1/64*D^2*ycis*(D^2-
4*ycis^2)^(1/2)+1/128*D^4*atan(2*ycis/(D^2-
4*ycis^2)^(1/2))+1/12*m_cranio^3*ycis^4-
1/3*m_cranio^2*ycis^3*b_cranio+1/2*m_cranio*ycis^2*b_cranio^2-
1/3*ycis*b_cranio^3)

Solid_AMI=(pi*(DS/2)^4)/4
% Symbolic Manipulation of Integrals
%
%Define symbolic variables
% syms y x ymin ymax xmin xmax b m .....
%
% Assign ymin and ymax
% ymin=-((D/2)^2-x^2)^0.5
%
% Inisde integration (with respect to y)
% z=int(y^2,y,ymin,ymax)
%
% Assign xmin and xmax
%
% Outside integral (with resepct to x)
% Z=int(z,x,xmin,xmax)

% Substitue true variable names
% syms b_medio
%ZZ=subs(ZZ,b,b_medio)
end
if CC==TC
Mediolateral_AMI=2*(-1/96*CC*(D^2-CC^2)^(3/2)-1/64*D^2*CC*(D^2-
CC^2)^(1/2)-1/64*D^4*atan(CC/(D^2-CC^2)^(1/2))-
1/128*i*D^4*log(i*D^(1/2))+1/128*i*D^4*log(-i*D^(1/2)))
Craniocaudal_AMI=2*(1/96*(D^2-CC^2)^(1/2)*(CC^2)^(3/2)+1/64*D^2*(D^2-
CC^2)^(1/2)*(CC^2)^(1/2)-1/3*(D^2-CC^2)^(1/2)+1/64*D^4*atan((D^2-
CC^2)^(1/2)/(CC^2)^(1/2)));
Z=2*(1/64*(D^2)^(3/2)/pi^(1/2)/(-1/D^2)^(1/2)*(2/3*pi^(1/2)*(D^2-
CC^2)^2/D^4-2*pi^(1/2)*(D^2-CC^2)/D^2-1/2*(-2*log(2)-3/2-log(D^2-CC^2)-
log(-1/D^2))*pi^(1/2)-1/12*pi^(1/2)*(D^2-CC^2)^2/D^4*(9/(D^2-
CC^2)^2*D^4-24/(D^2-CC^2)*D^2+8)-1/12*pi^(1/2)*(D^2-
CC^2)^2/D^4*(20/(D^2-CC^2)*D^2-8)*(1-1/(D^2-
CC^2)*D^2)^(1/2)+pi^(1/2)*log(1/2+1/2*(1-1/(D^2-CC^2)*D^2)^(1/2)))-
1/24*CC^3*(D^2-CC^2)^(1/2));
ZZ =2*(1/64*(D^2)^(3/2)/pi^(1/2)/(-1/D^2)^(1/2)*(2/3*pi^(1/2)*(D^2-
CC^2)^2/D^4-2*pi^(1/2)*(D^2-CC^2)/D^2-1/2*(-2*log(2)-3/2-log(D^2-CC^2)-
log(-1/D^2))*pi^(1/2)-1/12*pi^(1/2)*(D^2-CC^2)^2/D^4*(9/(D^2-
CC^2)^2*D^4-24/(D^2-CC^2)*D^2+8)-1/12*pi^(1/2)*(D^2-
CC^2)^2/D^4*(20/(D^2-CC^2)*D^2-8)*(1-1/(D^2-
CC^2)*D^2)^(1/2)+pi^(1/2)*log(1/2+1/2*(1-1/(D^2-CC^2)*D^2)^(1/2)))-
1/24*CC^3*(D^2-CC^2)^(1/2));
a2 =-1/96*(1/4*D^2-1/4*CC^2)^(1/2)*(CC^2)^(3/2)-1/64*D^2*(1/4*D^2-
1/4*CC^2)^(1/2)*(CC^2)^(1/2)-1/128*D^4*atan(2*(1/4*D^2-
1/4*CC^2)^(1/2)/(CC^2)^(1/2))+1/24*CC^3*(1/4*D^2-1/4*CC^2)^(1/2);
```

```
a3 =1/96*(1/4*D^2-1/4*CC^2)^(1/2)*(CC^2)^(3/2)+1/64*D^2*(1/4*D^2-
1/4*CC^2)^(1/2)*(CC^2)^(1/2)+1/128*D^4*atan(2*(1/4*D^2-
1/4*CC^2)^(1/2)/(CC^2)^(1/2))-1/24*CC^3*(1/4*D^2-1/4*CC^2)^(1/2);
Craniocaudal_AMI=2*(a3-a2)
Solid_AMI=(pi*(DS/2)^4)/4
End
```

APPENDIX FOUR

ADDITIONAL DATA

CHAPTER ONE

The following is the compliance data (N/mm) for the HP and LC-DCP constructs which was briefly discussed but not included within the Chapter 1 data:

Specimen	100 N	200 N	300 N
Hybrid 1	0.0036	0.0050	0.0069
Hybrid 2	0.0015	0.0013	0.0013
Hybrid 3	0.0037	0.0046	0.0061
Hybrid 4			
Hybrid 5	0.0025	0.0028	0.0034
Hybrid 6	0.0028	0.0031	0.0036
Hybrid 7			
Hybrid 8	0.0064	0.0086	0.0118
Hybrid 9	0.0011	0.0012	0.0012
AVERAGE	**0.0031**	**0.0038**	**0.0049**
STDEV	**0.0018**	**0.0026**	**0.0037**
LC-DCP 1	0.0067	0.0080	0.0101
LC-DCP 2	0.0014	0.0019	0.0020
LC-DCP 3	0.0059	0.0070	0.0091
LC-DCP 4			
LC-DCP 5	0.0039	0.0056	0.0074
LC-DCP 6	0.0024	0.0034	0.0047
LC-DCP 7			
LC-DCP 8	0.0094	0.0125	0.0146
LC-DCP 9	0.0013	0.0013	0.0013
AVERAGE	**0.0044**	**0.0057**	**0.0070**
STDEV	**0.0030**	**0.0039**	**0.0047**

Table A4-1. Compliance data for HP and LC-DCP constructs.

The following are the exact p-values for the above compliance data:

HP vs LC-DCP
- within 100 N: 0.047
- within 200 N: 0.012
- within 300 N: 0.007

Load within HP
- 300 vs 100: 0.009
- 300 vs 200: 0.051
- 200 vs 100: 0.189

Load within LC-DCP
- 300 vs 100: <0.001
- 300 vs 200: 0.020
- 200 vs 100: 0.031

The following are the exact p-values for the angular deformation data discussed in Chapter 1:

HP vs LC-DCP
- within 100 N: 0.310
- within 200 N: 0.023
- within 300 N: 0.002

Load within HP
- 300 vs 100: <0.001
- 300 vs 200: 0.010
- 200 vs 100: 0.047

Load within LC-DCP
- 300 vs 100: <0.001
- 300 vs 200: 0.003
- 200 vs 100: 0.016

The following are the exact p-values for the plate strain data discussed in Chapter 1:

HP vs LC-DCP
- within 100 N: 0.226
- within 200 N: 0.013
- within 300 N: 0.001

Load within HP
- 300 vs 100: <0.001
- 300 vs 200: 0.004
- 200 vs 100: 0.013

Load within LC-DCP
- 300 vs 100: <0.001
- 300 vs 200: <0.001
- 200 vs 100: <0.001

Finite Element Analysis

Materials and Methods

To rationalize the hypotheses beyond mathematical calculations, a finite element analysis was done to simulate the conditions experienced by the plates during pre-bending. Based on the cross-sections of the plates where the bend occurred (solid section), a model was created (Figure A) for each cross section in Autodesk Inventor Professional (AutoCAD V.10).

Figure A4-1. Cross-sectional view of the solid section of the HP (left) and LC-DCP (right).

Powered by ANSYS® Design Space, a finite element mesh was created, boundary conditions were implemented, and equivalent (von Mises) stresses, and resultant deformations were solved for. Both plates were modeled as Stainless Steel, with tetrahedral elements. The cross sections were extended to a length of 20 mm and boundary conditions represented 3-point bending with opposite ends constrained to restrict movement and a point load of 100 N was applied to the dorsal surface of the plate.

Results

Cross sections of the solid section (Figure A4-1) of both plates were created in Autodesk Inventor Professional and extended to an arbitrary length of 20 mm to give a 3-dimensional representation of the region where the bend occurred. Applying a 100 N point load to the dorsal surface of the beam and constraining the ends of the beam simulated 3-point bending. Results of the simulation are shown in Figure A4-2 and A4-3.

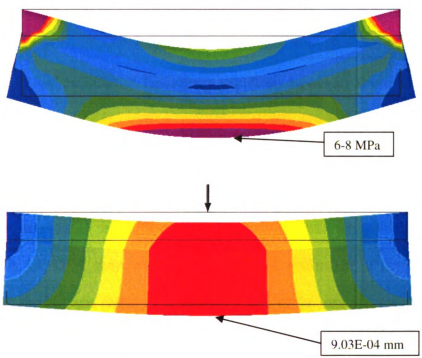

Figure A4-2. FEA of the HP. Equivalent (von Mises) stresses are shown on the top (5:1 actual scale), deformation is shown on the bottom (2:1 actual scale)

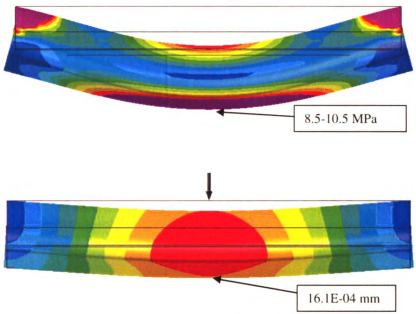

Figure A4-3. FEA of the LC-DCP. Equivalent (von Mises) stresses are shown on the top (5:1 actual scale), deformation is shown on the bottom (2:1 actual scale)

Under the given load of 100 N, the LC-DCP underwent larger deformations, and larger magnitudes of stress in the area of interest, which is the dorsal surface of the plate. The von Mises stresses on the surface of the HP were approximately 6.701 MPa, on the surface of the LC-DCP they were 10.106 MPa, a difference of 34%. Maximum deformation in the HP was found to be 9.03E-04 mm in the area of interest, whereas in the LC-DCP it was 16.1E-04 mm, a difference of approximately 44%.

CHAPTER TWO

The following data includes results of the following tests:

Torsion

6 mm ILN with 2.7 mm bolts

6 mm ILN with ESF

6 mm ILN with ESF minus connecting bar

with p-values for pairwise comparisons

ML Bending

6 mm ILN with ESF minus connecting bar

CC Bending

6 mm ILN with ESF minus connecting bar

Compression

6 mm ILN with ESF minus connecting bar

Torsion Tests

	Sample	Intl. Comp. (0-1.5 N*m)			Term. Comp. (2.5-5 N*m)			Slack	Def.
		+	-	avg	+	-	avg		
6 mm ILN w/ 2.7 mm bolts	GILT1	NA	NA	NA	1.17	1.16	1.16	5.43	17.1
	GILT2	NA	NA	NA	1.16	1.15	1.15	6.38	17.95
	GILT3	NA	NA	NA	1.17	1.15	1.16	6.08	17.76
	GILT4	NA	NA	NA	1.16	1.15	1.15	6.58	18.14
	Mean	NA	NA	NA	1.17	1.15	1.16	6.12	17.74
	SD	NA	NA	NA	0.01	0.01	0.01	0.5	0.45
6 mm ILN w/ ESF	GXF1T1 b	2.2	2.28	2.24	0.94	0.95	0.94	NA	13.44
	GXF1T2	1.18	1.94	1.56	0.83	0.84	0.83	NA	11.53
	GXF1T3	1.57	2	1.79	0.83	0.84	0.83	NA	11.69
	GXF1T5	1.67	2.2	1.94	0.88	0.87	0.88	NA	12.12
	Mean	NA	NA	1.88	0.87	0.87	0.87	NA	12.2
	SD	NA	NA	0.29	0.05	0.05	0.05	NA	0.87
6 mm ILN w/ ESF (minus connecting bar)	GXF0T1 b	NA	NA	NA	1.15	1.16	1.16	6.99	18.58
	GXF0T2	NA	NA	NA	1.08	1.06	1.07	5.45	16.19
	GXF0T3	NA	NA	NA	1.09	1.08	1.08	5.67	16.53
	GXF0T5	NA	NA	NA	1.14	1.13	1.13	5.78	17.09
	Mean	NA	NA	NA	1.11	1.11	1.11	5.97	17.1
	SD	NA	NA	NA	0.04	0.04	0.04	0.69	1.06

Table A4-2. Torsion test data

Torsion p-values

Terminal Compliance			*Slack*			*Def.*	
ILN vs EXFIX no bar	0.0254	unpaired t-test	ILN vs EXFIX no bar	0.3742	unpaired t-test	ILN vs EXFIX no bar	0.1538	unpaired t-test
ILN vs EXFIX w/ bar	0.0000	unpaired t-test				ILN vs EXFIX w/ bar	0.0000	unpaired t-test
EXFIX w/bar vs EXFIX no bar	0.0001	paired t-test				EXFIX w/bar vs EXFIX no bar	0.0000	paired t-test

Table A4-3. Torsion data p-values

ML Bending Tests

	Sample	Terminal Compliance (2.5-5 N*m) positive	negative	average	Slack	Overall Def.
6 mm ILN w/ ESF (minus connecting bar)	GX0ml1a	0.775	0.720	0.747	5.784	10.998
	GX0ml2a	0.814	0.852	0.833	4.969	10.764
	GX0ml4a	0.713	0.626	0.670	5.981	10.656
	GX0ml5a	0.657	0.762	0.709	5.595	10.530
	Mean	0.740	0.740	0.740	5.582	10.737
	SD	0.069	0.094	0.070	0.438	0.199

CC Bending Tests

	Sample	Terminal Compliance (2.5-5 N*m) positive	negative	average	Slack	Overall Def.
6 mm ILN w/ ESF (minus connecting bar)	GX0cc1a	1.025	1.205	1.115	1.897	9.702
	GX0cc2a	1.100	1.280	1.190	1.529	9.864
	GX0cc4a	1.024	1.186	1.105	2.062	9.828
	GX0cc5a	1.114	1.231	1.173	1.521	9.702
	Mean	1.066	1.226	1.146	1.752	9.774
	SD	0.048	0.041	0.042	0.271	0.084

Compression Tests

	Sample	Compliance (mm/N*E-04)	Displacement (mm*E-02)
6 mm ILN w/ ESF (minus connecting bar)	GXF0C2	6.300	11.400
	GXF0C3	5.500	9.500
	GXF0C4	8.100	14.600
	GXF0C5	6.300	11.400
	Mean	6.550	11.725
	SD	1.100	2.116

Table A4-4. Mediolateral bending, Craniocaudal bending, and Compression test data

CHAPTER THREE

The following data are included, pairwise comparisons follow each set of data

Torsion

ILN6s (50 mm fracture gap)

ILN6b (50 mm fracture gap)

ILN8S (50 mm fracture gap)

ILN8B (50 mm fracture gap)

3.5 mm br-DCP (50 mm and 100 mm fracture gap)

ILNn (50 mm fracture gap)

Mediolateral Bending

ILN6s (50mm and 100mm fracture gap)

ILN6b (50mm and 100mm fracture gap)

ILN8S (50mm and 100mm fracture gap)

ILN8B (50mm and 100mm fracture gap)

3.5 mm br-DCP (50mm and 100mm fracture gap)

ILNn (50mm and 100mm fracture gap)

Craniocaudal Bending

ILN6s (50mm and 100mm fracture gap)

ILN6b (50mm and 100mm fracture gap)

ILN8S (50mm and 100mm fracture gap)

ILN8B (50mm and 100mm fracture gap)

3.5 mm br-DCP (50mm and 100mm fracture gap)

ILNn (50mm and 100mm fracture gap)

Torsion Tests		Moment: 5 Nm		TC Range: ±2 to ±5			
ILN6s	(+) TC (x10-2)	(-) TC (x10-2)	Avg TC(x10-2)	IC (x10-2)	Max def	Slack (y)	Comments
6st1	1.758	1.701	1.729	NA	39.96	22.52	
6st2	1.676	1.638	1.657	NA	37.1	20.34	
6st3	1.635	1.596	1.616	NA	34.32	18.09	
6st4	1.626	1.597	1.612	NA	34.39	18.20	
MEAN	1.674	1.633	1.653		36.44	19.79	
SD	0.060	0.049	0.055		2.68	2.10	
ILN6b	(+) TC (x10-2)	(-) TC (x10-2)	Avg TC(x10-2)	IC (x10-2)	Max def	Slack (y)	Comments
GILT2	1.158	1.145	1.152	NA	17.95	6.38	From Scott Goet's data
GILT4	1.156	1.147	1.152	NA	18.14	6.58	From Scott Goet's data
6bt3	1.094	1.089	1.092	NA	18.15	7.18	
6bt4	1.092	1.086	1.089	NA	18.2	7.26	
MEAN	1.125	1.117	1.121		18.11	6.85	
SD	0.037	0.034	0.035		0.11	0.43	
ILN8s	(+) TC (x10-2)	(-) TC (x10-2)	Avg TC(x10-2)	IC (x10-2)	Max def	Slack (y)	Comments
8St1	0.717	0.713	0.715	NA	23.90	16.71	
8St2	0.719	0.737	0.728	NA	24.47	17.16	
ILn8s3	0.854	0.742	0.798	NA	23.57	15.58	Early Jen data Computer file name 35s5at
ILn8s4	0.841	0.742	0.792	NA	23.77	15.81	Early Jen data Computer file name 35s6at
MEAN	0.783	0.734	0.758		23.93	16.31	
SD	0.075	0.014	0.043		0.39	0.74	

ILN8b	(+) TC (x10-2)	(-) TC (x10-2)	Avg TC(x10-2)	IC (x10-2)	Max def	Slack (y)	Comments
ILn8b1	0.858	0.699	0.779	NA	13.20	5.45	Early Jen data file name 35b2ct
ILn8b2	0.816	0.764	0.790	NA	13.58	5.77	Early Jen data file name 35b4ct
8Bt3	0.586	0.594	0.590	NA	11.44	5.52	
8Bt4	0.567	0.578	0.573	NA	11.41	5.66	
MEAN	0.707	0.659	0.683		12.41	5.60	
SD	0.152	0.088	0.118		1.14	0.14	
ILNn	(+) TC (x10-2)	(-) TC (x10-2)	Avg TC(x10-2)	IC (x10-2)	Max def	Slack (y)	Comments
ILnt1	0.883	0.883	0.883	NA	8.60	None	
ILnt2	0.851	0.837	0.844	NA	8.14	None	
ILnt3	0.898	0.844	0.871	NA	8.13	None	
ILnt4	0.890	0.856	0.873	NA	8.30	None	
MEAN	0.881	0.855	0.868		8.29		
SD	0.021	0.020	0.017		0.22		
3.5brDCP	(+) TC (x10-2)	(-) TC (x10-2)	Avg TC(x10-2)	IC (x10-2)	Max def	Slack (y)	Comments
Pt1	1.227	1.180	1.204	NA	11.32	None	
Pt2	1.358	1.284	1.321	NA	12.18	None	
Pt3	1.363	1.337	1.350	NA	12.47	None	
Pt4	1.246	1.231	1.239	NA	11.74	None	
MEAN	1.299	1.258	1.278		11.93		
SD	0.072	0.068	0.069		0.50		
Ptsh1	1.793	1.763	1.778	NA	16.74		loss of alignment
Ptsh2	1.854	1.888	1.871	NA	17.36	None	loss of alignment
Ptsh3	1.739	1.715	1.727	NA	16.36	None	
Ptsh4	1.861	1.846	1.854	NA	17.25	None	
MEAN	1.812	1.803	1.807		16.93	#DIV/0!	
SD	0.057	0.078	0.067		0.46	#DIV/0!	

Table A4-5. Torsion test data

Torsion - Terminal Compliance p-values

	ILN6s	ILN6b	ILN8S	ILN8B	br-DCP	ILNn
ILN6s	NA	$p < 0.001$	$p < 0.001$	$p < 0.001$	$p < 0.001$	$p < 0.001$
ILN6b	$p < 0.001$	NA	$p < 0.001$	$p < 0.001$	$p = 0.003$	$p < 0.001$
ILN8S	$p < 0.001$	$p < 0.001$	NA	$p = 0.115$	$p < 0.001$	$p = 0.027$
ILN8B	$p < 0.001$	$p < 0.001$	$p = 0.115$	NA	$p < 0.001$	$p = 0.002$
br-DCP	$p < 0.001$	$p = 0.003$	$p < 0.001$	$p < 0.001$	NA	$p < 0.001$
ILNn	$p < 0.001$	$p < 0.001$	$p = 0.027$	$p = 0.002$	$p < 0.001$	NA

Torsion - Angular Deformation p-values

	ILN6s	ILN6b	ILN8S	ILN8B	br-DCP	ILNn
ILN6s	NA	$p < 0.001$	$p < 0.001$	$p < 0.001$	$p < 0.001$	$p < 0.001$
ILN6b	$p < 0.001$	NA	$p < 0.001$	$p < 0.001$	$p < 0.001$	$p < 0.001$
ILN8S	$p < 0.001$	$p < 0.001$	NA	$p < 0.001$	$p < 0.001$	$p < 0.001$
ILN8B	$p < 0.001$	$p < 0.001$	$p < 0.001$	NA	$p = 0.585$	$p < 0.001$
br-DCP	$p < 0.001$	$p < 0.001$	$p < 0.001$	$p = 0.585$	NA	$p < 0.001$
ILNn	$p < 0.001$	$p < 0.001$	$p < 0.001$	$p < 0.001$	$p < 0.001$	NA

Torsion - Slack p-values

	ILN6s	ILN6b	ILN8S	ILN8B	br-DCP	ILNn
ILN6s	NA	$p < 0.001$	$p < 0.001$	$p < 0.001$	$p < 0.001$	$p < 0.001$
ILN6b	$p < 0.001$	NA	$p < 0.001$	$p = 0.073$	$p < 0.001$	$p < 0.001$
ILN8S	$p < 0.001$	$p < 0.001$	NA	$p < 0.001$	$p < 0.001$	$p < 0.001$
ILN8B	$p < 0.001$	$p = 0.073$	$p = 0.115$	NA	$p < 0.001$	$p < 0.001$
br-DCP	$p < 0.001$	$p < 0.001$	$p < 0.001$	$p < 0.001$	NA	$p = 1$
ILNn	$p < 0.001$	$p < 0.001$	$p < 0.001$	$p < 0.001$	$p = 1$	NA

Torsion - Angular Deformation minus Slack p-values

	ILN6s	ILN6b	ILN8S	ILN8B	br-DCP	ILNn
ILN6s	NA	$p < 0.001$	$p < 0.001$	$p < 0.001$	$p < 0.001$	$p < 0.001$
ILN6b	$p < 0.001$	NA	$p < 0.001$	$p < 0.001$	$p = 0.138$	$p < 0.001$
ILN8S	$p < 0.001$	$p < 0.001$	NA	$p = 0.077$	$p < 0.001$	$p = 0.132$
ILN8B	$p < 0.001$	$p < 0.001$	$p = 0.077$	NA	$p < 0.001$	$p = 0.008$
br-DCP	$p < 0.001$	$p = 0.138$	$p < 0.001$	$p < 0.001$	NA	$p < 0.001$
ILNn	$p < 0.001$	$p < 0.001$	$p = 0.132$	$p = 0.008$	$p < 0.001$	NA

Tables A4-6 thru A4-9. Torsion data p-values.

Bending Tests	Moment: 3.5 Nm TC Range: +/-1.5-3.5	50mm gap - 10mm bone diameter	120mm gap 14.5mm bone diameter				
ILN6sML	(+) TC (x10-2)	(-) TC (x10-2)	Avg TC(x10-2)	IC (x10-2)	Ang def	Slack	Comments
6SMLb1	0.483	0.636	0.5595	NA	12.62	8.69	ML first, CC second, interference
6SMLb2	0.533	0.684	0.6085	NA	13.09	8.82	CC first, ML second, interference
6SMLb3	0.556	0.67	0.613	NA	14.9	10.61	ML first, CC second, interference
6SMLb4	0.479	0.624	0.5515	NA	14.86	11.05	CC first, ML second, interference
MEAN	0.51	0.65	0.58		13.87	9.79	
SD	0.04	0.03	0.03		1.18	1.21	
6SMLb1sh	0.843	1.16	1.0015	NA	21.6	14.53	CC first, ML second, no interference
6SMLb2sh	0.842	1.05	0.946	NA	21.29	14.67	ML first, CC second, huge slack, no interference
6SMLb3sh	0.725	1.253	0.989	NA	25.92	18.93	CC first, ML second, no interference
6SMLb4sh	0.753	1.15	0.9515	NA	22.68	16.03	no interference
MEAN	0.79	1.15	0.97		22.87	16.04	
SD	0.06	0.08	0.03		2.12	2.04	
ILN6sCC	(+) TC (x10-2)	(-) TC (x10-2)	Avg TC(x10-2)	IC (x10-2)	Max def	Slack	Comments
6SCCb1	0.64	0.88	0.76	NA	12.58	3.07	ML first, CC second, interference
6SCCb2	0.51	0.604	0.557	NA	12.33	3.21	CC first, ML second, interference
6SCCb3	0.499	0.608	0.5535	NA	12.29	3.25	ML first, CC second, interference
6SCCb4	0.559	0.669	0.614	NA	12.55	3.19	CC first, ML second, interference
MEAN	0.55	0.69	0.62		12.44	3.18	

SD	0.06	0.13	0.10		0.15	0.08	
6SCCb1sh	1.603	2.045	1.824	NA	16.94	4.2	CC first, ML second, no interference
6SCCb2sh	2.066	2.789	2.4275	NA	18.66	2.7	ML first, CC second, no interference
6SCCb3sh	1.945	2.51	2.2275	NA	18.61	3	CC first, ML second, no interference
6SCCb4sh	1.787	2.117	1.952	NA	17.15	3.51	no interference
MEAN	1.85	2.37	2.11		17.84	3.35	
SD	0.20	0.35	0.27		0.92	0.66	
ILN6bML	(+) TC (x10-2)	(-) TC (x10-2)	Avg TC(x10-2)	IC (x10-2)	Max def	Slack	Comments
GILBml2a	0.603	0.775	0.689		11.3	6.44	Use Scott's data
6BMLb2b	0.558	0.689	0.6235	NA	11.27	6.96	CC first, ML second
6BMLb3	0.754	0.871	0.8125	NA	12.96	7.3	ML first, CC second
GILBml3a	0.69	0.75	0.72		11.54	6.53	Use Scott's data
MEAN	0.65	0.77	0.71		11.77	6.81	
SD	0.09	0.08	0.08		0.80	0.40	
6BMLb1sh	0.766	0.899	0.8325	NA	12.49	6.65	CC first, ML second, No interference
6BMLb2sh	0.786	1.013	0.8995	NA	12.37	6.06	ML first, CC second, No interference
6BMLb3sh	0.739	0.935	0.837	NA	14.67	8.81	CC first, ML second, No interference
6BMLb4sh	0.768	0.887	0.8275	NA	12.38	6.57	ML first, CC second, No interference
MEAN	0.76	0.93	0.85		12.98	7.02	
SD	0.02	0.06	0.03		1.13	1.22	
ILN6bCC	(+) TC (x10-2)	(-) TC (x10-2)	Avg TC(x10-2)	IC (x10-2)	Max def	Slack	Comments
GILBcc2a	1.14	1.24	1.19		10.52	2.24	Use Scott's data
6BCCb2b	1.1	1.276	1.188	NA	10.51	2.17	CC first, ML second
6BCCb3	1.168	1.273	1.2205	NA	10.85	2.38	ML first, CC second
GILBcc3a	1.13	1.286	1.208		10.57	2.14	Use Scott's data

MEAN	1.13	1.27	1.20		10.61	2.23	
SD	0.03	0.02	0.02		0.16	0.11	
6BCCb1sh	1.182	1.301	1.2415	NA	11.14	2.44	CC first, ML second, No interference
6BCCb2sh	1.114	1.294	1.204	NA	10.64	2.17	ML first, CC second, No interference
6BCCb3sh	1.175	1.327	1.251	NA	11.05	2.26	CC first, ML second, No interference
6BCCb4sh	1.161	1.335	1.248	NA	10.12	1.38	ML first, CC second, No interference
MEAN	1.16	1.31	1.24		10.74	2.06	
SD	0.03	0.02	0.02		0.47	0.47	
ILN8sML	(+) TC (x10-2)	(-) TC (x10-2)	Avg TC(x10-2)	IC (x10-2)	Max def	Slack	Comments
8SMLb1	0.347	0.426	0.3865	NA	12.24	9.61	ML first, CC second
8SMLb2b	0.446	0.514	0.48	NA	10.84	7.48	CC first, ML second
8SMLb3	0.344	0.447	0.3955	NA	12.58	9.81	CC first, ML second
8SMLb4	0.453	0.442	0.4475	NA	12.35	9.21	ML first, CC second
MEAN	0.40	0.46	0.43		12.00	9.03	
SD	0.06	0.04	0.04		0.79	1.06	
8SMLb1sh	0.433	0.575	0.504	NA	17.73	14.18	ML first, CC second, no interference
8SMLb2bsh	0.427	0.553	0.49	NA	18.41	14.96	file name 8SMLb2sh, CC first, ML second
8SMLb3sh	0.478	0.553	0.5155	NA	18.31	14.68	ML first, CC second
8SMLb4sh	0.453	0.561	0.507	NA	17.89	14.33	CC first, ML second
MEAN	0.45	0.56	0.50		18.09	14.54	
SD	0.02	0.01	0.01		0.33	0.35	
ILN8sCC	(+) TC (x10-2)	(-) TC (x10-2)	Avg TC(x10-2)	IC (x10-2)	Max def	Slack	Comments
8SCCb1	0.314	0.345	0.3295	NA	7.4	5.09	
8SCCb2	0.309	0.337	0.323	NA	7.11	4.84	
8SCCb3	0.314	0.345	0.3295	NA	7.34	5.04	
8SCCb4	0.366	0.4	0.383	NA	7.2	4.52	

MEAN	0.33	0.36	0.34		7.26	4.87	
SD	0.03	0.03	0.03		0.13	0.26	
8SCCb1sh	0.953	1.07	1.0115	NA	12.96	5.83	ML first, CC second, no interference
8SCCb2sh	0.939	1.129	1.034	NA	12.64	5.38	CC first, ML second
8SCCb3sh	0.799	0.99	0.8945	NA	12.15	5.86	ML first, CC second
8SCCb4sh	0.816	0.93	0.873	NA	11.90	5.73	CC first, ML second
MEAN	0.88	1.03	0.95		12.41	5.70	
SD	0.08	0.09	0.08		0.48	0.22	
ILN8bML	(+) TC (x10-2)	(-) TC (x10-2)	Avg TC(x10-2)	IC (x10-2)	Max def	Slack	Comments
8BMLb1	0.41	0.466	0.438	NA	8.06	5.12	ML first, CC second, intereferenc e?
8BMLb2b	0.331	0.41	0.3705	NA	6.34	3.73	ML first, CC second, intereferenc e?
8BMLb3b	0.321	0.469	0.395	NA	6.95	4.18	ML first, CC second
8BMLb4b	0.348	0.414	0.381	NA	6.91	4.25	ML first, CC second
MEAN	0.35	0.44	0.40		7.07	4.32	
SD	0.04	0.03	0.03		0.72	0.58	
8BMLb1sh	0.458	0.535	0.4965	NA	9.31	5.8	ML first, CC second
8BMLb2bsh	0.479	0.617	0.548	NA	9.54	5.73	file name 8BMLb2sh, CC first, ML second
8BMLb3bsh	0.487	0.57	0.5285	NA	9.25	5.57	file name 8BMLb3sh, ML first, CC second
8BMLb4bsh	0.54	0.566	0.553	NA	9	5.16	file name 8BMLb4sh, CC first, ML second
MEAN	0.49	0.57	0.53		9.28	5.57	
SD	0.03	0.03	0.03		0.22	0.29	
ILN8bCC	(+) TC (x10-2)	(-) TC (x10-2)	Avg TC(x10-2)	IC (x10-2)	Max def	Slack	Comments
8BCCb1	0.305	0.575	0.44	NA	5.99	2.91	ML first, CC second

8BCCb2	0.575	0.416	0.4955	NA	6.5	3.04	CC first, ML second
8BCCb3b	0.452	0.573	0.5125	NA	6.73	3.2	ML first, CC second
8BCCb4	0.638	0.44	0.539	NA	6.21	2.47	CC first, ML second
MEAN	0.49	0.50	0.50		6.36	2.91	
SD	0.15	0.08	0.04		0.32	0.31	
8BCCb1sh	0.72	0.798	0.759	NA	7.45	2.12	ML first, CC second
8BCCb2sh	0.663	0.692	0.6775	NA	7.18	2.41	CC first, ML second
8BCCb3bsh	0.671	0.76	0.7155	NA	7.52	2.52	file name 8BCCb3sh, ML first, CC second
8BCCb4sh	0.617	0.722	0.6695	NA	6.91	2.22	CC first, ML second
MEAN	0.67	0.74	0.71		7.27	2.32	
SD	0.04	0.05	0.04		0.28	0.18	

Br-DCP ML	(+) TC (x10-2)	(-) TC (x10-2)	Avg TC(x10-2)	IC (x10-2)	Max def	Slack	Comments
PMLb1	0.919	0.954	0.9365	NA	6.23	None	Beaut
PMLb2	0.887	0.908	0.8975	NA	6.06	None	Beaut
PMLb3	0.901	0.955	0.928	NA	6.14	None	Beaut
PMLb4	0.883	0.929	0.906	NA	6.16	None	Beaut
MEAN	0.90	0.94	0.92		6.15		
SD	0.02	0.02	0.02		0.07		
PMLb1sh	1.351	1.462	1.4065	NA	9.56	None	
PMLb2sh	1.375	1.472	1.4235	NA	9.59	None	
PMLb3sh	1.356	1.456	1.406	NA	9.63	None	
PMLb4csh	1.349	1.456	1.4025	NA	9.54	None	
MEAN	1.36	1.46	1.41		9.58		
SD	0.01	0.01	0.01		0.04		
Br-DCP CC	(+) TC (x10-2)	(-) TC (x10-2)	Avg TC(x10-2)	IC (x10-2)	Max def	Slack	Comments
PCCb1	0.225	0.229	0.227	NA	1.49	None	Beaut
PCCb2	0.223	0.231	0.227	NA	1.53	None	Beaut

PCCb3	0.217	0.222	0.2195	NA	1.48	None	Beaut
PCCb4	0.222	0.225	0.2235	NA	1.51	None	Beaut
MEAN	0.22	0.23	0.22		1.50		
SD	0.00	0.00	0.00		0.02		
PCCb1sh	0.351	0.363	0.357	NA	2.11	None	
PCCb2sh	0.345	0.361	0.353	NA	2.12	None	
PCCb3sh	0.345	0.345	0.345	NA	2.11	None	
PCCb4csh	0.454	0.464	0.459	NA	2.68	None	
MEAN	0.37	0.38	0.38		2.26		
SD	0.05	0.05	0.05		0.28		

ILNn ML	(+) TC (x10-2)	(-) TC (x10-2)	Avg TC(x10-2)	IC (x10-2)	Max def	Slack	Comments
ILnMLb1	0.583	0.553	0.568	NA	3.87	None	original file name 40n1cb, new file name has letter "**b**"
ILnMLb2	0.697	0.657	0.677	NA	4.36	None	original file name 40n3ab, new file name has letter "**b**"
ILnMLb3	0.602	0.62	0.611	NA	4.07	None	original file name 40mediab, new file name has letter "**b**"
ILnMLb4	0.575	0.544	0.5595	NA	3.8	None	original file name 40n6cb, new file name has letter "**b**"
MEAN	0.61	0.59	0.60		4.03		
SD	0.06	0.05	0.05		0.25		
ILnMLb1sh	0.559	0.586	0.5725	NA	3.91	None	Instron file name does not have "**h**"

ILnMLb2sh	0.563	0.589	0.576	NA	3.91	None	Instron file name does not have "h"
ILnMLb3sh	0.563	0.597	0.58	NA	3.98	None	Instron file name does not have "h"
ILnMLb4sh	0.55	0.582	0.566	NA	3.89	None	file name does not have the "h"
MEAN	0.56	0.59	0.57		3.92		
SD	0.01	0.01	0.01		0.04		
ILNn CC	(+) TC (x10-2)	(-) TC (x10-2)	Avg TC(x10-2)	IC (x10-2)	Max def	Slack	Comments
ILnCCb1	0.821	0.865	0.843	NA	5.38	None	
ILnCCb2	0.756	0.81	0.783	NA	5.06	None	
ILnCCb3	0.805	0.852	0.8285	NA	5.24	None	
ILnCCb4	0.804	0.857	0.8305	NA	5.256	None	
MEAN	0.80	0.85	0.82		5.23		
SD	0.03	0.02	0.03		0.13		
ILnCCb1sh	0.813	0.879	0.846	NA	5.4	None	file name does not have the "h"
ILnCCb2sh	0.76	0.805	0.7825	NA	5	None	file name does not have the "h"
ILnCCb3sh	0.796	0.849	0.8225	NA	5.2	None	file name does not have the "h"
ILnCCb4sh	0.8	0.86	0.83	NA	5.27	None	file name does not have the "h"
MEAN	0.79	0.85	0.82		5.22		
SD	0.02	0.03	0.03		0.17		

Table A4-10. Mediolateral and craniocaudal bending data (long and short specimens).

Mediolateral Bending – Compliance p-values (50 mm gap only)

	ILN6s	ILN6b	ILN8S	ILN8B	br-DCP	ILNn
ILN6s	NA	p = 0.003	p < 0.001	p < 0.001	p < 0.001	p = 0.541
ILN6b	p = 0.003	NA	p < 0.001	p < 0.001	p < 0.001	p = 0.005
ILN8S	p < 0.001	p < 0.001	NA	p = 0.36	p < 0.001	p < 0.001
ILN8B	p < 0.001	p < 0.001	p = 0.36	NA	p < 0.001	p < 0.001
br-DCP	p < 0.001	p < 0.001	p < 0.001	p < 0.001	NA	p < 0.001
ILNn	p = 0.541	p = 0.005	p < 0.001	p < 0.001	p < 0.001	NA

Mediolateral Bending – Angular Deformation p-values (50 mm gap only)

	ILN6s	ILN6b	ILN8S	ILN8B	br-DCP	ILNn
ILN6s	NA	p = 0.002	p = 0.002	p < 0.001	p < 0.001	p < 0.001
ILN6b	p = 0.002	NA	p = 0.657	p < 0.001	p < 0.001	p < 0.001
ILN8S	p = 0.002	p = 0.657	NA	p < 0.001	p < 0.001	p < 0.001
ILN8B	p < 0.001	p < 0.001	p < 0.001	NA	p = 0.095	p < 0.001
br-DCP	p < 0.001	p < 0.001	p < 0.001	p = 0.095	NA	p < 0.001
ILNn	p < 0.001	p < 0.001	p < 0.001	p < 0.001	p < 0.001	NA

Mediolateral Bending – Slack p-values (50 mm gap only)

	ILN6s	ILN6b	ILN8S	ILN8B	br-DCP	ILNn
ILN6s	NA	p < 0.001	p = 0.149	p < 0.001	p < 0.001	p = 1
ILN6b	p < 0.001	NA	p < 0.001	p < 0.001	p < 0.001	p < 0.001
ILN8S	p = 0.149	p < 0.001	NA	p < 0.001	p < 0.001	p < 0.001
ILN8B	p < 0.001	p < 0.001	p < 0.001	NA	p < 0.001	p < 0.001
br-DCP	p < 0.001	p < 0.001	p < 0.001	p < 0.001	NA	p < 0.001
ILNn	p < 0.001	p < 0.001	p < 0.001	p < 0.001	p = 1	NA

Mediolateral Bending – Angular Deformation minus Slack (50 mm gap only)

	ILN6s	ILN6b	ILN8S	ILN8B	br-DCP	ILNn
ILN6s	NA	p < 0.001	p < 0.001	p < 0.001	p < 0.001	p = 0.821
ILN6b	p < 0.001	NA	p < 0.001	p < 0.001	p < 0.001	p = 0.001
ILN8S	p < 0.001	p < 0.001	NA	p = 0.305	p < 0.001	p < 0.001
ILN8B	p < 0.001	p < 0.001	p = 0.305	NA	p < 0.001	p < 0.001
br-DCP	p < 0.001	p < 0.001	p < 0.001	p < 0.001	NA	p < 0.001
ILNn	p = 0.821	p = 0.001	p < 0.001	p < 0.001	p < 0.001	NA

Table A4-11 thru A4-14. Mediolateral bending data p-values

Craniocaudal Bending – Compliance p-values (50 mm gap only)

	ILN6s	ILN6b	ILN8S	ILN8B	br-DCP	ILNn
ILN6s	NA	$p < 0.001$	$p < 0.001$	$p = 0.001$	$p < 0.001$	$p < 0.001$
ILN6b	$p < 0.001$	NA	$p < 0.001$	$p < 0.001$	$p < 0.001$	$p < 0.001$
ILN8S	$p < 0.001$	$p < 0.001$	NA	$p < 0.001$	$p = 0.002$	$p < 0.001$
ILN8B	$p = 0.001$	$p < 0.001$	$p < 0.001$	NA	$p < 0.001$	$p < 0.001$
br-DCP	$p < 0.001$	$p < 0.001$	$p = 0.002$	$p < 0.001$	NA	$p < 0.001$
ILNn	$p < 0.001$	$p < 0.001$	$p < 0.001$	$p < 0.001$	$p < 0.001$	NA

Craniocaudal Bending – Angular Deformation p-values (50 mm gap only)

	ILN6s	ILN6b	ILN8S	ILN8B	br-DCP	ILNn
ILN6s	NA	$p < 0.001$	$p < 0.001$	$p < 0.001$	$p < 0.001$	$p < 0.001$
ILN6b	$p < 0.001$	NA	$p < 0.001$	$p < 0.001$	$p < 0.001$	$p < 0.001$
ILN8S	$p < 0.001$	$p < 0.001$	NA	$p < 0.001$	$p < 0.001$	$p < 0.001$
ILN8B	$p < 0.001$	$p < 0.001$	$p < 0.001$	NA	$p < 0.001$	$p < 0.001$
br-DCP	$p < 0.001$	$p < 0.001$	$p < 0.001$	$p < 0.001$	NA	$p < 0.001$
ILNn	$p < 0.001$	$p < 0.001$	$p < 0.001$	$p < 0.001$	$p < 0.001$	NA

Craniocaudal Bending – Slack p-values (50 mm gap only)

	ILN6s	ILN6b	ILN8S	ILN8B	br-DCP	ILNn
ILN6s	NA	$p < 0.001$	$p < 0.001$	$p = 0.039$	$p < 0.001$	$p = 0.001$
ILN6b	$p < 0.001$	NA	$p < 0.001$	$p < 0.001$	$p < 0.001$	$p < 0.001$
ILN8S	$p < 0.001$	$p < 0.001$	NA	$p < 0.001$	$p < 0.001$	$p < 0.001$
ILN8B	$p = 0.039$	$p < 0.001$	$p < 0.001$	NA	$p < 0.001$	$p < 0.001$
br-DCP	$p < 0.001$	$p < 0.001$	$p < 0.001$	$p < 0.001$	NA	$p = 1$
ILNn	$p < 0.001$	$p < 0.001$	$p < 0.001$	$p < 0.001$	$p = 1$	NA

Craniocaudal Bending – Ang. Deformation minus Slack p-values (50 mm gap only)

	ILN6s	ILN6b	ILN8S	ILN8B	br-DCP	ILNn
ILN6s	NA	$p < 0.001$	$p < 0.001$	$p < 0.001$	$p < 0.001$	$p < 0.001$
ILN6b	$p < 0.001$	NA	$p < 0.001$	$p < 0.001$	$p < 0.001$	$p < 0.001$
ILN8S	$p < 0.001$	$p < 0.001$	NA	$p < 0.001$	$p < 0.001$	$p < 0.001$
ILN8B	$p < 0.001$	$p < 0.001$	$p < 0.001$	NA	$p < 0.001$	$p < 0.001$
br-DCP	$p < 0.001$	$p < 0.001$	$p < 0.001$	$p < 0.001$	NA	$p < 0.001$
ILNn	$p < 0.001$	$p < 0.001$	$p < 0.001$	$p < 0.001$	$p < 0.001$	NA

Table A4-15 thru A4-18. Craniocaudal bending data p-values